ACCELERATOR AND INSTRUMENTATION R&D AND CONSTRUCTION

STATUS OF K800 CYCLOTRON

T.Antaya, R.Au, S.M.Austin, H.Blosser, R.Blue, S.Bricker, D.Cole, M.Fowler, M.Gordon, L.Harwood, H.Hilbert, D.Johnson, E.Kashy, H.Laumer, D.Lawton, M.Mallory, F.Marti, P.Miller, B.Milton, R.Morin, J.Nolen, J.Ottarson, B.Sherrill, G.Stork, J.Vincent, X.Wu, and A.Zeller

The K800 is the largest of the superconducting cyclotrons presently under construction in the world and in terms of magnetic rigidity, the 2nd largest cyclotron ever constructed, the bending power of its magnet being exceeded only by that of the 1 GeV synchrocyclotron at Gatchina. The bending power of the K800 magnet corresponds to an actual "K" value in excess of 1200 MeV; isochronous operation is limited by a "focusing K" of 400 MeV (or 200 MeV/nucleon when Q/A = 1/2).

The K800 design can, in most respects, be characterized as an improved K500 system. Problems which have turned up in the course of operating the K500 as a research facility have hopefully all been adequately addressed and corrected in the K800 design. The K800 is however at the same time a much more difficult technical challenge than the K500 due to the larger number of turns, the higher dee voltage, the tighter spiral, and the intrinsic proximity of the operating point to the 3/2's radial stopband. These factors particularly impact the design of the extraction system The status of some of the K800 subsystems is discussed below:

The K800 Magnet

Operating Experience. Beginning with the initial magnet run in May 1984, the superconducting coils for the K800 have been run at liquid helium temperature for a total of approximately 12 months and have operated for over 1000 hours for mapping of the magnetic fields and testing of various systems under the influence of the field. The coils have performed solidly with no indications of shorts or winding movements.

Heat Leak. A measurement of the total heat load generated in the coil cryostat can be obtained by monitoring the helium level after closing off the liquid helium supply ("taking a boil-off curve"). To do this reliably, the cryostat pressure and lead gas flow must be maintained at a constant level; knowledge of the liquid helium reservoir geometry will then yield absolute heat load values. Normal boiloff curves indicate a heat load of 20 watts for the filled coil. As the liquid level falls, the boil-off rate also falls, indicating that much of the heat load is in the upper part of the coil and at the median plane. A drop from 10 watts to 8 watts occurs as the liquid level goes below the median plane of the coil, and, just before the coil runs dry, the boiloff rate is equivalent to a heat load of 7 watts. The heat load carried away by liquid nitrogen cooled shields and intercepts is typically around 175 watts under operating conditions. The observed boiloff rates are not a problem for the laboratory's 800 watt (at 4.5 K) refrigeration system, but are never-the-less 2 to 3 times higher than expected.

A reevaluation of the actual cryostat internal conditions (vs. design conditions) has led to a tentative understanding of this heat load. During the initial running periods, the helium vessel was wrapped with 20 layers of multilayer insulation and the liquid nitrogen cooled radiation shield was in turn wrapped with 30 layers of multilayer insulation. Using a design value for heat transmission that takes into account that some of the multilayer insulation was fairly tightly packed, and noting that the 4 K surface area is approximately 30 m^2, a value of 7 watts is calculated for the

heat transmitted from the shield to the coil. Openings in the 80 K shield and unshielded penetrations through the median plane of the cryostat account for another 8 watts of heat load on the coil. These losses are then apparently the dominant factor in the larger-than-expected total heat load. In the coming months, as the coil is reassembled following installation of beam extraction elements, effort will be directed toward improving the overall effectiveness of the insulation and thermal shield systems with the goal of significantly reducing the total thermal load on the coil.

K800 Trim Coil Fabrication and Installation. The K800's one hundred twenty-six trim coils use fused dacron insulated, 0.250" square, OFHC, hollow copper conductor. Each coil was hand wound on one of twenty-one different fixtures corresponding to the radial location of the coil on the pole tip. Prior to being mounted on the pole tips, additional coil-to-ground insulation of two layers of fiberglass cloth was wrapped around each coil. The coils were then mounted on the pole tips and each of the six 3400 lb. pole tip, pole base, and trim coil assemblies were potted with an unfilled, flexibilized epoxy formula chosen for good mechanical and vacuum properties. The potting used a vacuum impregnation procedure with the epoxy cured by resistive heating in the trim coils themselves. Trim coil leads were dressed with additional insulating sleeving and routed through glass laminate clamps to combined vacuum, electrical, and water feedthroughs on the magnet surface.

Radio Frequency System

The status of the K800 RF system is described in detail in a following article in this Annual Report.

Extraction System

Layout of System Elements. The principal difference between the final K800 extraction system and previous versions is that the second electric deflector (E2) is reduced to one-third of its former length, which allows a mechanically important section of the cryostat wall to be left intact in the space occupied by the last third of the previous E2, thereby alleviating a problem of inadequate wall strength in that area. To make up the lost deflecting power, a passive magnetic dipole (B1) replaces the middle third of E2. The central field of this dipole element is 4 kilogauss, i.e. nearly six times the strength (at 200 MeV/nuc) of the electrostatic element it replaces. The layout of these and other extraction system elements is shown in Fig. 1.

The focusing bars M2-M8 have gradients ranging from 7.5 to 12 kilogauss/inch, with central field strengths of two to three kilogauss. Maximum E1 and E2 field strengths are 124 kilovolts/centimeter (this compares with 140 kV/cm required for maximum design energy in the K500). The magnetic elements B1, M1 and M2, which are close to the internal orbits, each have two compensators to eliminate first and second harmonic field perturbations. B1, unfortunately, cannot have perfect three-sector compensation because an exact 120° duplicate would interfere with the electric deflector E1. Its compensators (C1 and C2) are therefore single element bars placed at a larger radius, and a "wing" is added to B1 to give its fringe field the same shape as the field of the compensators over the last inch of internal orbit space.

The external field of B1 generates a significant displacement of the last internal orbit by decreasing the average field of the main magnet. M1 and its compensators largely offset this effect by generating a positive peak at the extraction radius. A second function of

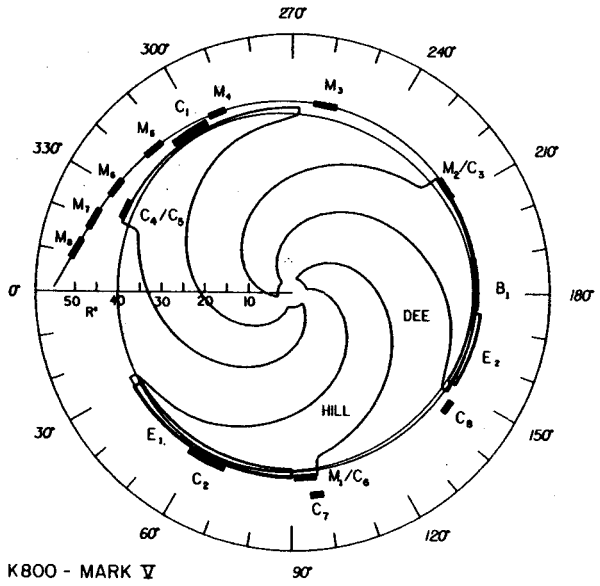

Fig. 1--Polar coordinate drawings showing the location of K800 extraction system elements. Symbols are: E-electrostatic deflector; M-magnetic focusing cluster; B-magnetic dipole; C-imperfection compensating element.

M1 is to prevent radial defocusing of the extracted beam by the M2 compensator at the end of E1. This is done by making another, smaller peak on the outer side of the large one. Figure 2 is a plot of the M1 field and the external field of C6, a compensator identical to M2, and shows the cancellation of the gradients.

At lower main-magnet excitations, the focusing power of the extraction system is adjusted by removing elements. Figure 3, for example, shows the radial and axial envelopes for the 200 MeV/nucleon beam and indicates that satisfactory focusing is obtained for this field with M3 not in use.

Vacuum System

The beam chamber of the K-800 superconducting cyclotron is maintained at high vacuum by two types of pumping systems, cryogenic and turbomolecular. The cryopumps which are mounted inside of each dee are the primary pumping system, but three external turbo-molecular pumps serve for the initial

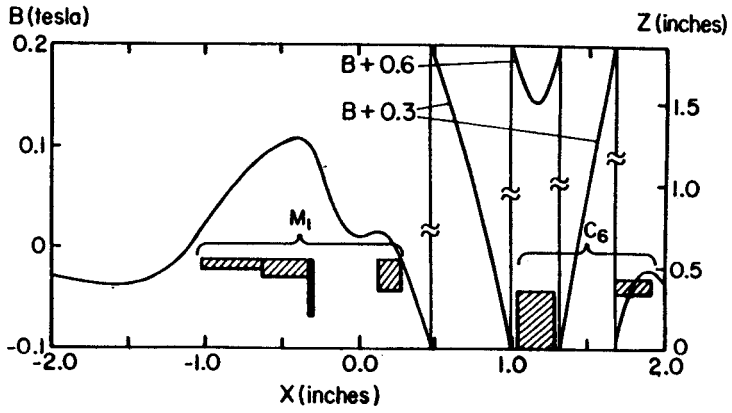

Fig. 2--Right ordinate--cross section through the pair of elements M1/C6 (which are identical to M2/C3 and C4/C5); left ordinate--the magnetic field produced by these elements.

pumpdown and pump away gasses evolved when the cryopanels warm up. The effectiveness of pumps external to the cyclotron is limited by the conductance of the penetrations through the magnet yoke; thus each of the 550 liter/second turbo pumps yields a net pumping speed for air of only 110 liters/second in the beam space, or a total of 330 liters/second from the three external pumps combined.

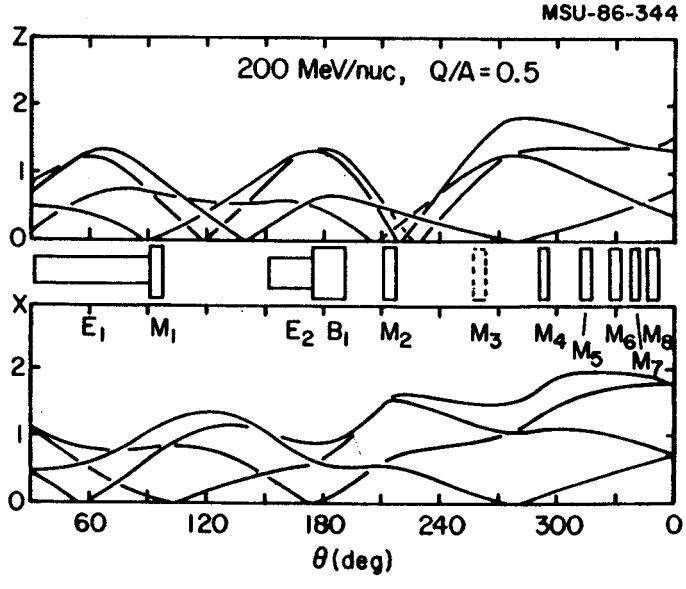

Fig. 3 --Extraction orbit behavior for Q/A=0.5 rays in the 200 MeV/nuc field.

The cryopanels are located in the lower half of each of the three dees. Each helium-cooled panel presents 900 square centimeters of pumping surface which, taking account of the transmission to the panels, leads to a net pumping speed for nitrogen of about 2500 liters/second. Each cryopanel includes a layer of charcoal granules epoxied to the surface to enhance the pumping for neon, helium, and hydrogen which would otherwise have a low sticking probability. The cryopanel is enclosed in a shroud, cooled by liquid nitrogen, to shield the panel from high temperature sources of radiant energy. A small reservoir for each of the cryogens, helium and nitrogen, is housed in the dee stem just outside the dee, and heavy copper thermal buses conduct heat from the cryopanel and its shroud to these reservoirs.

A continuous supply of liquid helium and liquid nitrogen is delivered to the cryopanels via vacuum-jacketed cryolines in the interior of each lower dee stem. Following the K500 design, these lines emerge at the shorted end of the dee stem which is at ground potential and are connected to the general cryo-distribution system. The cryopanels and shrouds are instrumented with sensors for temperature monitoring during operation. The estimated total pumping speed for the three cryopanels and the turbo-molecular pumps of about 8000 liters/second is expected to result in a vacuum of about 10^{-7} Torr in the beam region.

Control System

The K800 controls will be a sub-system of the overall NSCL Phase II control system. This system can be characterized as a modified copy of the Fermilab Linac control system. The basic structure is a distributed, intelligent data base, system, with the multi-node structure connected by ARCNET, a token passing ring network. The ARCNET link permits passing commands or readings and data base alteration as needed. An ARCNET to ETHERNET gateway will be used to interface the control system to the central laboratory VAX system.

Local control nodes are M68010 single board microprocessor systems. All local control nodes operate with the same core program; the general program is tailored to the requirements of a specific complement of devices by using a table driven data base stored in nonvolatile RAM and specific device driver software. Each local control node can be directly accessed via a dedicated local console consisting of an alpha-numeric keyboard, 5" CRT screen, multipurpose knob and several switches.

General system control is from multiple main console nodes, which include a centralized master station for program development, initial load, and archival storage. Each main console is managed by a multi-tasking operating system servicing several CRT screens, a keyboard, a mouse, a collection of adjustment knobs, and a bank of meters. All main consoles are basically identical and are user configurable within the generic capabilities of the console. The primary control CRT is touch sensitive; other screens are used for dedicated display of interlocks, graphical displays, control menus, parameter lists and data logs. An operator at any console can select any desired set of major subsystems for control (provided the subsystems are not already under the exclusive control of some other console), can save and recall complete sets of value settings for all parameters, can save and recall user configured console control arrangements, and can change parameter settings via knobs, touch screen, keyboard or mouse buttons.

Interlocks will be managed by separate programmable logic controllers. Control system computers will have "read only" access to interlock status in the programmable controllers, and will have a mechanism to request that interlocks be reset. (The read-only access protects interlocks from unintentional

changes by control system computers.)

Cryogenic System

The 800 watt helium refrigerator-liquefier from Cryogenic Consultants Inc. has been operated since Sept. 1982. The system utilizes liquid nitrogen precooling and incorporates 3 reciprocating expanders, the third acting as a wet expander which can be bypassed by a J.T. valve. The design allows for expansion of capacity by adding a turbine expander and also includes intermediate temperature tap points appropriate for controlled coil cooldown. An additional feature, a cold gas compressor, is being added to maintain a lower helium boiling pressure in the cyclotron coils when the refrigerator is running at maximum capacity. Three oil flooded screw compressors can supply up to 80 grams/s of room temperature helium at a pressure of 18 atmospheres. Liquid nitrogen, brought in by tanker truck and stored in two 3600 gallon tanks, is used as well for operating liquid nitrogen cooled shields and intercepts in coil cryostats and transfer lines. A comprehensive cryogen distribution system is being build in stages. The design makes extensive use of Invar 36, a material with a very low thermal expansion coefficient. The Invar 36 has been used in unshielded, multi-layer insulated transfer lines up to 65 feet in length (these lines were used in the K800 magnet testing and mapping phase to supply cryogens to the magnet).

The final crogenic distribution system uses counterflow coaxial subcooling lines for controlled liquid transfer and employs liquid nitrogen cooled shields to minimize the 4.5 K heat load. One of 4 main distribution boxes is in operation and a second is about to be completed by a local shop. The system in its final configuration will be capable of supplying cryogens to the main coils and cryopumps of the two cyclotrons as well as to an ECR source and to approximately 70 beamline magnets.

Future Directions

Superconducting ECR

Planning for the K800 cyclotron has identified stand alone operation with an ECR ion source as a likely dominant mode of operation, if ion sources can be realized having the capability of producing charge states of Q=40-50 for very heavy ions. At the present time, the only ECR design philosophy that has resulted in significant new gains in intensity versus Q, over the usual gains from well optimized operation are the high frequency sources at Grenoble. Unfortunately, very high frequency microwave transmitters are quite expensive, and direct purchase of such a transmitter is not presently to be expected at NSCL. We are therefore starting construction of a source for the K800 which will be able to operate over a wide range of frequencies from the 6.4 GHz of our present transmitters up to as high as 30 GHz, so that the source can be reconfigured when, or if, we are later able to obtain transmitter(s) of higher frequency. The field strengths required in the higher end of this design range dictate use of superconducting coils. Design of such a superconducting magnet is presently underway at NSCL and is discussed in more detail elsewhere in this Annual Report.

K500/K800 Coupling vs. Stand Alone

Continuing rapid progress in the development of ECR sources opens to question the wisdom of proceeding with implementation of the originally planned coupling of the K500 and K800 cyclotrons. The purpose of coupling is to provide the K800 with ions of higher charge than can be obtained directly from an ion source (the charge state is increased by passing the K500 beam through a stripping foil at the K800 injection point). This process is expensive by virtue of the cost of the rather complicated

beam transport system which must connect the two cyclotrons, and overall reliability for a two accelerator system is obviously reduced compared to a one accelerator system. The appeal of coupling the two cyclotrons then disappears as the charge states which can be produced in the ion source approach those which result from stripping of the K500 beam.

The central uncertainty in deciding whether or not to couple is an assessment of the improvement to be expected in ECR sources in the next few years. In the past few years, ECR's have made quite impressive advances -- trends also indicate likely further gains by going to higher rf frequencies and by going to larger sources. Figure 4 indicates the impact of possible further ECR improvements on the K800 operating regime. One curve in this figure is based on those ions for which electrical currents from existing ECRs are at the 1 μa level, a second curve raises these assumed charge states by a factor of 5/4's, and a third curve raises the assumed charge states by a factor of 5/3's. For comparison, two other curves are also included, one the original goals of the coupled cyclotron project, the other, the energy which results from coupling the K500 and K800, with the K500 injected from an existing ECR. (The limits for this last curve are due to the injection process and would not be changed by using a higher charge state in the K500.) The judgement as to whether to couple then comes down to an evaluation of which of the ECR curves to assume for the near future and of the incremental value of the expanded research regime which would be derived from coupling versus the cost of coupling (in both money and reliability). Given these issues, and the need for additional information on further ECR improvements, a decision has been taken at NSCL to defer coupling until additional data becomes available, while maintaining all designs in a coupling-compatible state, so that coupling can be implemented later without undue difficulty, if, or when, future developments give a clear cost effectiveness justification for such an action.

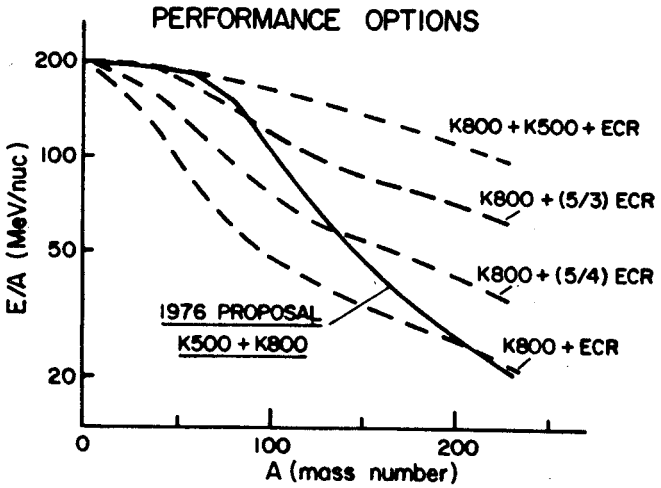

Fig. 4--Energy/nuc versus mass number for several combinations of cyclotrons and ion source (see text).

References

1. F. Bourg, et. al. Sixth International Workshop on the ECR Ion Source, Berkeley, CA (1985).
2. T. Antaya and Z.Q. Xie, 7th International Workshop on the ECR Ion Source, Julich, W.Germany (1986).
3. R. Geller and B. Jacquot, 7th International Workshop on the ECR ion Source, Julich, W.Germany (1986).

K800 RF STATUS

T.R. Jones, J. Brandon, J. Ottarson, D. Scott and J. Vincent

The past year saw a major part of the final assembly of the RF system completed. The work performed varied from designing, building, and testing intricate signal modules, to working the problems out of a 1.2 MVA power supply.

Prior to 1986, there was a history of problems with the Aydin power supply caused by malfunction of the 13.2KV to 15.4KV step-up transformer. Two dummy loads and the "C" amplifier were set up in March 1986, for a combined 1.2MW load, and the Aydin was brought up to full power. After six full-power crowbars, (an event which shorts the output, lifts the inputs, and in microseconds directs the stored energy in the system to ground), and approximately three hours of running time, the system failed.

Again, the failure was traced to the step-up transformer. NWL Transformer, the company which manufactured the unit, honored their warranty and took the transformer back for repair. They discovered that the transformer failed because of improperly installed jacking screws on the bottom coil frame of the unit. These screws, subjected to the 40-60,000lb instantaneous force of a full-power crowbar, broke from their mountings, causing the coil to be skewed out of position and shorted. The redesign and repair of the transformer took the company approximately six weeks. They then returned it for installation.

Before resuming tests on the Aydin, we modified the system in two ways. First, we installed an SCR/electronic relay circuit in the relay string to enable the vacuum contactors to open within two cycles after a crowbar cycle had been initiated. Second, we installed a Snubber network, to prevent voltage overshoot, prior to the step-up transformer. We felt that these two additions and the redesign of the mechanical section of the transformer by NWL would increase the life expectancy of the unit. We then conducted a run of approximately 16 hours at full power with numerous crowbars. The Aydin performed well during these tests.

However, at the time of this writing, the Aydin step-up transformer is again out of commission, and its course of repair had not yet been decided.

During 1986, the tuned semi-rigid coaxial cables were also cut out and put in place. This job required each semi-rigid cable which interconnects the RF balcony with the three amplifiers to be custom measured and cut so the signals on these cables remain in the proper phase relation.

Along with the semi-rigid cables, many control and signal monitoring lines had to be run to the cyclotron. These cables include servo control lines, signal monitoring cables, and Modicon interlock cables.

Another area of great progress was the construction and installation of the RF electronics, which by the fall of the year, was nearing completion.

One of the changes in the electronics of the K800 from the K500 was the change of the interface section in the dee voltage regulator and phase trimmer modules. This new subunit allows us to place phase and amplitude information on a data bus more dependably for monitoring by the control system.

We also took a step toward improving system reliability and accuracy by installing transient absorbers and EMI/RFI line filters on the power lines which feed the RF system.

The Modicon brand control system, already in use at the Laboratory, was selected to be the programmable controller for the RF system. A stand alone Modicon 884 controller will monitor

water flow, water temperature, and door interlocks to insure equipment integrity and personnel safety.

Prior to the project, the Modicon program was written in a haphazard "spaghetti" code which made troubleshooting very difficult. After researching ways of standardizing the programming, we developed a system which uses input/output relations to allow us to use a "top-down" programming technique.

Another advance to the Modicon/RF control system this year was the addition of a "Panel Mate" programmable controller unit. This system allows an operator to inspect the program of the Modicon and monitor a number of controls and faults on a TV screen. It allows us to control all three RF systems together or independently using programmable soft-touch buttons on the Panel Mate. This system worked so well that we also used it to control the ECR system.

The method of analysis of the various cavities was also perfected. Reson[1] was completed prior to 1986, but was first used extensively in 1986 for the analysis of the various dee shape modifications and it has proven itself well.

The mechanical design and construction of the K800 RF system moved along very well in 1986. A large amount of work was put into the stems, dees, and transmitter.

For the stems, we installed a new silver graphite finger assembly on the sliding short. We discovered on the K500 that the best working sliding short has silver graphite fingers on the outer conductor. However, there was some concern about whether these fingers could withstand the current densities on the inner conductors of the stems on the K800. There were tested and proved to work, so the new sliding shorts will have silver graphite fingers for the contact points.

The shape of the dees was finalized during 1986 and manufacture has now begun.

The transmitter construction was also completed in 1986. This includes the transmission lines, amplifier boxes, and associated components. After initial testing, it was discovered that the amplifier design must be modified to accommodate stability requirements of the final amplifier, but the bulk of the work has been completed.

The coupling capacitor is new for the K800. It involves a variable parallel plate capacitor enclosed in a bellows assembly. This allows a good range of coupling to the dees. The design was completed and manufacture has begun.

In general, 1986 proved to be a year of prime accomplishment for the RF group and shops involved with the construction of the RF system. These shops were the Assembly, Mechanical, and Design Groups, Machine, Welding, Electrical, and Electronics Shops and the Purchasing Department, to name a few. Major goals were set forth and met. Although much work remains for the RF group, we are well on our way to completing the radio frequency portion of the K800 cyclotron.

References

1. J. Vincent, 1986 NSCL Annual Report, "General TEM Non Systematic RF Resonator Design and Analysis Techniques," (May 1987).

GENERAL RF DESIGN AND ANALYSIS TECHNIQUES FOR TWO-CONDUCTOR, NON-SYMMETRIC, AND NON-UNIFORM RESONATORS

John Vincent

In order to design and analyze the RF resonators for the K800 and Harper Cyclotrons, we needed a process for analyzing non-symmetric resonators. The processes which are usually used for this analysis take the form of one large main program which solves the three-dimensional problem by requiring one dimension to be circularly symmetric. They do not allow switching the symmetric axis within the same analysis. For example, one could not model a coaxial tee. Some three-dimensional programs do exist, but geometric constraints are placed on what can be modeled. When true three-dimensional codes are used to model truly three-dimensional cases such as ours, the large inputs and run times make them unattractive for this application. In addition, these programs have no provisions for incorporating lumped elements which are often required to model couplers, tube capacities, etc.

The RF resonators required by the RF amplifiers, beam bunchers and cyclotrons in this laboratory require a different approach. Two years ago the author began developing the process now known as "RESON".[1] This process is directly applicable to symmetric and non-symmetric two-conductor resonant structures in which the direction of wave propagation (Poynting vector) at any point in the resonator may be determined by inspection.

Until "RESON", however, the conventionally accepted method of analysis was used at the Lab. With this method, when the non-symmetric portions of a resonator are small (when compared to the resonant wavelength and the symmetric portions), one can successfully use two-dimensional codes that require symmetry for the third dimension. The non-symmetric section(s) are modeled by some symmetric quasi-equivalent section.

The dimensions of the equivalent section are established by an iterative, trial and error process: A scale model of the structure is designed and constructed so that electrical measurements can be made over the desired frequency band. Meanwhile, a computer model (either a specially written program which does a simplified transmission line analysis or an input file for some two- or three-dimensional program as previously described) is designed. Next, electrical measurements are made on the scale model over the desired frequency band. Finally, the computer model is modified to match the measured response of the scale model over the fundamental frequency band by a trial and error process.

It should be clear that models derived in this manner are only valid over the finite band in which the match was forced. Therefore, higher order resonances (out of the matched band) calculated by the computer model are suspect. The validity of conduction losses and potential variations predicted by the model are strictly a function of how skillfully these mechanisms are matched to those that would exist in the final devices.

Usually, the equivalent section was used to model the actual accelerating electrodes (dees). This meant that as the electrode size became large with respect to the resonant wavelength, and its shape became more diverse, the accelerating potential along the electrode became less well defined by the model. Not only was the assumption of a uniform potential along the accelerating electrode no longer valid, but the processes used to calculate these quantities were becoming less reliable. Since the value of the accelerating potential is most critical near the beam extraction location, improper design of the electrode structure would cause extraction

difficulties, unnecessarily high potentials, and excessive losses. This would result in unnecessary sparking and excessive energy costs. Transmitter design and analysis derived from the previous techniques resulted in insufficient or flawed information about harmonic distortion.

Clearly, more accurate information was needed about higher order modes, conduction losses, and potential distributions.

The process developed to cope with the need outlined above is two-fold. First, appropriate two-dimensional cross sections are taken perpendicular to the direction of wave propagation, through the asymmetric portion(s) of the structure to be modeled. These cross sections are accurately translated into equivalent, but symmetric, triaxial or triplaner cross sections.

Second, these equivalent triplaner or triaxial cross sections are joined together with linearly tapering transmission lines. This results in a symmetric equivalent circuit for the asymmetric portions of the structure. This circuit is then combined with the model(s) of the symmetric or lumped portion(s) of the original structure (which were obtained by more conventional methods) to form the complete, symmetric model of the overall structure.

The translation of each of the original asymmetric cross sections to the equivalent triplaner or triaxial cross section is accomplished by the following process. A computer program is used to solve the static two-dimensional problem at each of the cross sections for the potential distributions, electric field vectors, electric stored energy, and "The Equivalent Perimeter".

"The Equivalent Perimeter" transforms power and current densities which vary about the perimeter of a complex, asymmetric (or non-uniform) conductor cross section into constant power and current densities about the perimeter of a new equivalent symmetric (or uniform) cross section. This is done in a way that leaves the total current and the resulting total power dissipated unchanged. The actual current densities over the original non-uniform conductor fall out of the calculation as a secondary, but useful result also.

Two equivalent perimeters are calculated: one for each conductor of the asymmetric cross section to be translated. The first is for the innermost ('lowest') conductor, and the second is for the outermost ('highest') conductor.

The equivalent perimeter for each conductor in the cross section being analyzed is calculated by taking the following line integral about the original conductor perimeter:

$$\rho = \frac{[\int |E_n(s)| ds]^2}{\int |E_n(S)|^2 ds}$$

where:

ρ = The equivalent perimeter

$E_n(s)$ = The electric field at the conductor boundary

ds = An infinitesimal element perpendicular to the wave direction, tangent to and at the conductor boundary

In general, it is impossible to translate both wave behavior and dissipation to only two uniform conductors. This is the reason for triplaner or triaxial cross sections. The innermost or 'lowest' conductor size is chosen to match the conduction losses on the innermost or 'lowest' conductor of the original geometry via the equivalent perimeter criteria. The next surrounding or 'higher' conductor size is chosen to match the characteristic impedance of the original geometry, with respect to the innermost or 'lowest' conductor. Note that this conductor is only used to match wave behavior between it and the innermost or 'lowest' conductor; it is ignored in power dissipation calculations. For the last conductor in the new cross section,

which has no dimensional relationship to the first two translated conductors, dimensions are chosen so its total losses match the conduction losses of the remaining conductor from the original geometry.

This translation is performed for every cross section needed to accurately model the asymmetric sections of the resonator. It results in a series of symmetric three-conductor cross sections. These sections are then joined together with linearly tapering three-conductor lines. The resulting symmetric three-conductor structure "accurately" models the original equivalent network of two-conductor asymmetric transmission lines. The linear taper between cross sections is achieved by creating a stairstep of uniform non-tapering lines in series. The number of steps (smoothness of taper) is user-selectable. Lumped elements are inserted where they truly exist, or where they can be used to model discontinuities. Virtually any arrangement of coaxial, coplaner, triaxial, or triplaner lines as well as resistors, capacitors, and inductors is allowed.

All transmission line outer conductors are automatically tied to datum (ground); hence, the inner conductor of one line tied to the outer conductor of another and vice-versa is not allowed.

Once the model, or equivalent circuit, has been derived as outlined above, the RESON program mentioned earlier is used to analyze it. The actual model used by the program for transmission lines consists of a linearly tapering line loaded by a capacity at one end. The program will calculate and automatically insert capacities at places of coaxial discontinuities unless told not to. Conduction losses on annuluses, not resulting from tapering lines, are also automatically found and computed. The program will also compute, insert and match a capacitive coupler to anywhere in the structure, or a magnetic coupler to any shorted transmission line.

RESON generates reports which describe the complete time harmonic electrical behavior of the network. Several types of analysis which are user-selectable are available as outputs from RESON. Examples include:

1. Harmonic analysis at any node.
2. Scan of a broad frequency range plotting the response.
3. A complete analysis of any resonant frequency found to include:

   a. Peak voltages at all nodes
   b. RMS currents entering all nodes
   c. Characteristic impedances
   d. The dimensions of all entered transmission lines
   e. The magnetic electric and total energy circulating in each element and in the total system
   f. The power dissipated of each element including resistors, capacitors, inductors, annuluses
   g. The total power dissipated
   h. The quality factor of all elements
   i. The overall quality factor
   j. The value of all discontinuity capacitances
   k. The value of coupling elements
   l. The equivalent shunt circuit at user selected nodes
   m. The exact resonant frequency
   n. The user-selected peak normalizing voltage
   o. The possible error in the calculations.

As can be seen, just about everything of even the most remote consequence is calculated and supplied to the user in report-ready form.

The entire process (with the exception of generating the required mechanical drawings) resides on a VAX 11/750. The two-dimensional static analysis program is a NSCL modified

version of POISSON.[2] Subroutines were added to POISSON to calculate the equivalent perimeter, electric stored energy, electric fields along conductor boundaries, current density, and loss density, and to generate reports of these quantities. These routines, although very usable, are not bug-free. The circuit analysis is an AC analysis performed by SPICE version 2G-6[3] from Berkeley. SPICE is called and controlled by about 5000 lines of Fortran code. RESON reads the user format free input file, generates the SPICE input file, performs the iteration which converges on resonant frequencies, calculates all the quantities described above and more, and finally generates all the reports requested.

The entire process is now being modified and downloaded to an IBM-compatible personal computer AT. The first generation will use IS-SPICE version 2G-6,[4] and Lahey F77L Fortran.[5] The controlling, calculating and reporting portion known as RESON will be downloaded first. We then will write a new AC circuit analysis code to replace IS-SPICE with a more suitable, faster code for this specific application.

Next, a new two-dimensional static analysis package will be written for the PC, which will accept its input in CAD fashion with a mouse. This program is planned to also plot field lines and allow the user to access specific field information at a point by clicking the mouse on the desired location interactively. While POISSON is mainly oriented to magnetic field analysis, this code should be completely oriented toward electric field analysis, allowing multiple dielectrics, infinite boundaries, etc. To accommodate these goals, finite element numerical analysis techniques will be used. To further decrease the run times, we shall investigate the feasibility of writing the program in the programming language C, supplemented by small assembly language subroutines if necessary.

The process has been used to fix the K800 RF transmitters and to design and/or analyze the following devices:

Design:

K800 cyclotron RF resonators
K800 cyclotron coupling
K800 DEE modification to aid extraction
Harper cyclotron RF resonators
Harper cyclotron RF couplers
K500 beam buncher
K500 RF transmitters

The response of all of these devices were calculated to accuracies of better than a few percent. No device designed exclusively with the RESON process has required any modification to work as specified. All these devices have had responses as calculated by the process, including the location and characteristics of the higher order resonances. The success with this process suggests that its continued development can only improve our ability to quickly and efficiently produce RF systems for any application in a very cost effective manner.

This process is an extremely useful and accurate tool, but only when used correctly. Detailed mathematics and derivations of all concepts used in the process are spelled out in the appendices of the RESON users' guide.

References

1. J. Vincent and J. Priller, RESON Users' Guide, unpublished.
2. R.F. Holsinger, POISSON User's Guide, unpublished.
3. A. Vladimirescu, et. al., SPICE Version 2G User's Guide, (University of California, Berkeley, 1981).
4. "IS-SPICE Manual", Personal Computer Circuit Design Tools, (Intusoft, San Pedro, Calif., 1985).
5. F77L Reference Manual, (Lahey Computer Systems, Inc., Incline Village, Nev., 1986).

CURRENT REGULATION FOR THE K-800 CYCLOTRON SUPERCONDUCTING MAGNET

A. McGilvra, J. Priller, J. Vincent

The K-800 magnet is made up of two mutually coupled, superconducting coils. Controlling the currents in coils such as these presents a multi-variable, non-linear control problem: multi-variable, because there are two currents to control and each affects the other; non-linear, because as the currents change, the inductances change.

The solution to this control problem is a discrete-time, adaptive control algorithm implemented on a micro-computer. The micro-computer continuously reads the current in each coil, calculates the voltages needed on each coil to make them reach their target currents simultaneously, and sends these voltages (via large transistor banks) to the coils.

The control algorithm (also known as ALM) is based on the following transformer equations that model two mutually coupled coils:

$$Va = La(dIa/dt) + M(dIb/dt) \quad \text{Eq. 1}$$
$$Vb = Lb(dIb/dt) + M(dIa/dt) \quad \text{Eq. 2}$$

Where:
- Va = Voltage applied to the alpha coil
- Vb = Voltage applied to the beta coil
- La = Inductance of the alpha coil
- Lb = Inductance of the beta coil
- M = Mutual inductance between the alpha coil and the beta coil
- Ia = Current in the alpha coil
- Ib = Current in the beta coil

Reasoning from Equations 1 and 2, we can arrive at the following equations for ALM:

$$Va = La(Iea/delt) + M(Ieb/delt) \quad \text{Eq. 3}$$
$$Vb = Lb(Ieb/delt) + M(Iea/delt) \quad \text{Eq. 4}$$

Where:
- Iea = Alpha error current (target current minus Ia)
- Ieb = Beta error current
- delt = Projected time for both currents to reach their targets

These equations allow ALM to calculate the voltages needed for both coil currents to reach their targets simultaneously. ALM calculates these voltages once per iteration. Nominally the iteration time is about 1.67 seconds. Equations 3 and 4 also allow ALM to regulate the rate of change of the currents. ALM attempts to achieve a 'zero' rate of change when the currents reach their targets.

ALM must also calculate delt, the projected time it takes for both currents to reach their targets. This is no easy task; one choice of delt may cause Va to exceed its limit, while another choice may cause Vb to exceed its limit. However, a state machine can define a "legal" range for delt to avoid having either Va or Vb exceed their limits. Once this range is defined, ALM chooses a delt within this range that gives optimum performance (minimum time-to-targets without overshoot).

In reality, the K-800 magnet varies from the ideal transformer model given above in several ways. The most bothersome of these differences are the resistances in series with every lead of the magnet. These resistances are the room temperature leads that connect the power supply to the magnet within the cryostat. Originally ALM was an incremental algorithm to overcome this lead resistance problem. The thinking behind this was that if ALM incremented the coil voltages with each iteration, based on a desired increment in the rate of change of the currents, ALM would eliminate the cumulative error caused by the voltage drop across the lead resistances. While this thinking is valid, it is not practical. The round-off errors from the

extra computations needed in an incremental algorithm far exceed the errors introduced by the lead resistances. For this reason, we greatly simplified ALM and simultaneously improved it by changing it to an absolute (non-incremental) algorithm.

Equations 3 and 4 imply that ALM must know the inductances to calculate the voltages. Since the inductances change as the coil currents change, ALM must periodically obtain updated inductances during a ramp to maintain control. There are three ways to do this:

1) read the inductance values from a table that contains each inductance as a function of the operating point (Ia,Ib),
2) calculate the inductances periodically from the measured currents and their rate of change, or
3) infer whether the assumed inductances are higher or lower than the actual inductances and increase or decrease the assumed inductances accordingly.

The first method presents the problem of the initial definition of the table. Assuming we could accurately calculate inductances to fill the table, this method would work. However, the round-off errors involved make it very difficult to calculate inductances accurately.

The second method would work if we could find a calculation method that overcomes the round-off error problem. So far, we haven't been able to overcome the round-off error problem so the first two methods are questionable.

The third method holds the most promise. It compares the two coil voltages to the two voltages calculated, as we replace La, Lb and M in Equations 1 and 2 with the assumed La, Lb, and M. Based on this comparison ALM can decide whether the assumed inductances are too high or too low and increase (or decrease) them accordingly. This method has been through preliminary testing and appears to work. One disadvantage of the inferrence method is that it can take several iterations of the control algorithm to arrive at the correct inductance values. This problem can be minimized by making intelligent initial guesses as close as possible to the actual values.

During testing it was found that a 1- to 3-second iteration time (sample time) was required to achieve acceptable performance. The 1.67 second time was chosen because it allows us to synchronize the algorithm with the cycle time of the instrument that measures the currents (Hewlett-Packard 3456A Digital Volt Meter).

To test ALM we first used a software model of the magnet that included lead resistances and changing inductances. Using this model we were able to achieve stability within one milliamp.

We then built an analog circuit (the "magnet" circuit) that simulated the magnet and we tested ALM again. This analog circuit did not include lead resistances and its effective inductances did not change. We used analog-to-digital and digital-to-analog converters with a resolution of 11 bits (approximately one amp out of +/- 1000 amps). With this lower resolution the algorithm could not control the "magnet" circuit. This is when we decided to change ALM to an absolute (non-incremental) algorithm. After this change, ALM controlled the "magnet" circuit very well, better than it controlled the software model which had 21 bits of resolution.

The present status of the magnet regulation project is as follows:

Software is being transferred from a development micro-computer to an implementation micro-computer.

A method of obtaining inductances is still under development (this will not prevent implementation).

The hardware needed to implement the new software is nearly complete and ready for testing.

STATUS OF INTEGRATED SOFTWARE PROJECT FOR CYCLOTRON DESIGN

L.H.Harwood

The focusing elements of the extraction system for the the K800 cyclotron are comprised of inert iron bars. The strong coupling of the positions of these bars to the positions of the internal beam lead to a well-defined, but lengthy and tedious, iterative procedure for finding the settings for the extraction system's elements. Further it was found that accurate calculations of the particle trajectories permitted no approximations in the calculations of the fields of the iron bars; these calculations increase the computing time for a given path-length by more than a factor of ten thereby compounding the computing time problem further. A decision was made to acquire a FPS-164 attached processor (which has a computing power of 5-15 times that of a VAX-780) and produce a new generation of cyclotron design software which would utilize the new hardware and extend the capabilities of the MSU software. An additional feature of the new package was that it was to be capable not only of designing "academic" machines but, additionally, it was planned that the package should eventually address the needs of the operations group for calculating machine set-up parameters; this required that the code be able to freely intermix calculated and measured fields at any stage of the calculations. Increased utility for the package was to be attained by implementing a screen-interactive communication format. A variety of small mathematical enhancements have been included.

The cyclotron software project was soon followed by a second large software project, that being the code to acquire, process, analyze, and utilize the body of data coming from the magnetic field mapping. It was necessary to not only analyze the data and the field but also the mapping apparatus and the magnet itself. This code and the cyclotron software were merged into a single effort for compatibility, ie. when a piece of code was available for one part of the effort it was available immediately for all others thus eliminating redundant debugging.

The code has been functionally completed. All major and most minor goals of the project have been realized. Paramount among these is the ability to adjust the currents so that the desired phase history is achieved for the beam. While calculated fields are sufficient for designing a cyclotron, actual operating parameters can only be found using measured fields. The package, dubbed affectionately "MONSTER" since it is monstrously big, accomplishes this task then builds a 360° field, ie. one with all harmonics included; the last is another of the enhancements over previous software as it uses fields with many of the harmonics removed due to computer speed and memory limitations. The user can then use that field for a wide variety of operations. These include: equilibrium orbits (in the 360° field or in a 120° field built dynamically from the 360° field), accelerated orbits (forward or backward), accelerated equilibrium orbits, and extraction. Accelerated orbits can be run forward of backward; the code includes the effects of the non-uniform radial voltage distribution on the dees at high frequency.

Output from the package is a mixture of plots and alpha-numerics; hard-copy of each are generally available. Accelerated orbit output is dominantly graphical. Plots of r vs p_r, z vs p_z, vertical envelope sizes vs turn number, x vs p_x are all available. Non-linear behavior can be examined with the automatic radial ellipse feature which accelerates a group of particles which form an ellipse in radial phase

space. The usual output is available for each of the particles and, additionally, the shape of the "ellipse" at various turns can be examined on the same plot.

Field analysis required a sizeable amount of the effort. Not only must the measured fields be analyzed but also the calculated field of the magnet and the iron bars comprising the extraction system. For example, fourier analysis of any of the field components frequently gives useful insight into the beam behavior. It is quite important that the first term in a fourier analysis of the field (the so-called first harmonic) be small near the $n_r=1$ resonance in order for the beam to be extracted correctly. The package was able to analyze the field constituents separately and thereby determine the sources of some of the first harmonic. Coil and coil tank centering are crucial steps in this process; one part of the code analyzes the first harmonic and, assuming the intrinsic first harmonic in the magnet's field is small, finds the distance the coil and coil tank must be moved to eliminate their contributions to the first harmonic. The cyclotron magnet was designed to have three identical 120°-wide sections. The accuracy of the machining and assembly of the magnet pieces can thus be tested by the part of the code that examines the field's deviation from three-fold symmetry; a displaced pole shows readily in such a plot. Naturally the field, its radial derivative, and its angular derivative can be plotted vs radius or angle or any of the three can be plotted in a contour plot in the r-theta plane.

Presently "MONSTER" is being used to do the final checks on the K800 cyclotron extraction system. Soon the final magnet assembly will occur and, utilizing this software, it will be possible to quickly analyze the next set of field mapping data and prepare for first beam. It should be noted that while this code was written with the K800 in mind, it is not specific to it and can fairly easily be modified to handle another machine; no modifications are necessary for any three-sector machines, eg. the K500 and the Harper-Grace Hospital K100 cyclotrons.

IMPROVEMENTS IN THE NUMERICAL MODEL OF THE NSCL K800 SUPERCONDUCTING CYCLOTRON MAGNET*

L.H. Harwood

The numerical model of the magnetic fields of the NSCL cyclotron magnets has shown systematic differences in the predicted and observed fields. The limitations in the models used for the azimuthally averaged field and the azimuthal field modulations have been investigated and are presented here.

Azimuthal average of field

The basis for the new B_{avg} calculations is the NSCL version of the code POISSON.[1,2,3] The axial symmetry option is used. Regions which do not have axial symmetry are modeled with an effective permeability curve which reflects the mixed occupation by air and iron. 22000 points, with 12000 in the iron, are used with the "universe" boundary at R = 300.0 in and z = 300.0 in. Table 1 lists the errors in the calculated B_{avg} for several magnet excitations. Even though the agreement is better with the new calculations, there is room for improvement. It is this improvement that is addressed here.

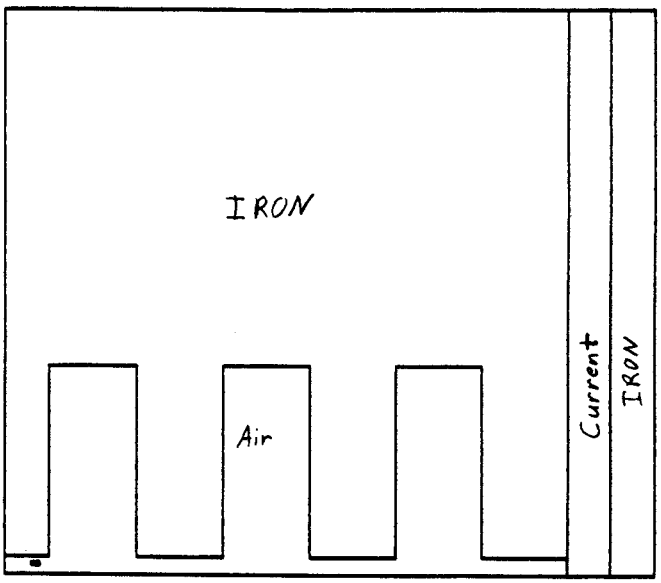

Fig. 1. "End" view used for tests of accuracy of stacking factor. For "side" view, the pole-valley region was replaced with a "stacked" material.

Table 1

Error in B_{avg} at R = 0.5 m

B(r=0)	$B_{meas} - B_{calc}$ (kG)		
	old	new	after offset
2.75	-.08	.47	.02
3.0	.19	.51	.06
3.2	.12	.40	-.05
3.4	.09	.64	.19
3.8	-.01	.52	.07
3.9	-.11	.32	-.13
4.1	-.25	.23	-.22
4.4	-.28	.33	-.12
4.6	-.47	.24	-.21
4.7	-.70	.11	-.34

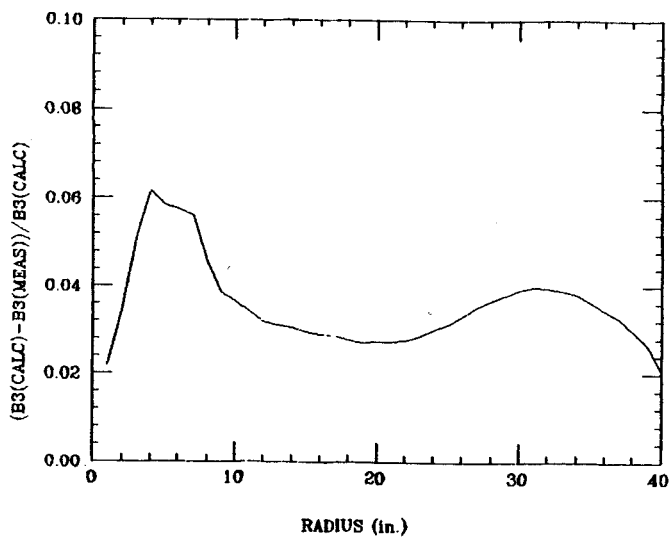

Fig. 2. Percentage error in the leading harmonic term in a Fourier analysis of the field.

As the stacking factor option in POISSON is a critical part of the calculations, the accuracy of this option was tested. Earlier tests[2] were for a different geometry and lower fields; however, the method used for the test was similar to that in ref. 1. In the tests, a model magnet was calculated with POISSON in two-dimensions as viewed from two orthogonal perspectives. In the first view, termed "end", the magnet has repetitive structure, as shown in fig. 1. The "poles" of the model are analogous

to the poles of the cyclotron. In order to reduce edge effects, the fields of only the central pole, valley, and first pole are used. The "side" view replaces the "poles" and intervening spaces with a region of uniform material that has a stacking factor representative of the pole geometry, i.e. if the poles and spaces are equal in size then the factor is 0.5. The same current is used for both views. For a factor of 0.4, comparable to the 0.38 which is valid for the cyclotron's pole region, the error in B_{avg} is 0.45 kG. This value varies little with field level above 30 kG; it does, however, depend fairly linearly on the stacking factor with the error going to zero. as the factor approaches 1. If this "offset" in B_{avg} is added to all fields, then the 110 to 640 G range of errors changes to -350 to 190 G; this is not a big improvement in the maximum error but the average error is much closer to 0, i.e. 0.4 kG is reduced to -0.1 kG which is a four-fold improvement.

Azimuthal modulations in the field

Flutter calculations utilize a model in which the non-axisymmetric portions of the magnet are given a uniform, vertical magnetization[4] distributed over the exact geometry of the magnet's parts. The field is then calculated as a surface integral of the effective currents on the pieces. This process obviously neglects the radial and azimuthal magnetization components. The rounded edges of the poles tips (which facilitate wrapping the trim coils around the pole tips) are modeled by square notches in the pole edges which remove the same volume of iron from the calculation as is removed on the real pole tip. These calculations yield $B_{flutter}$ values in error by as much as 0.3 kG or, typically, 3% of the amplitude of the third harmonic term in a Fourier series representation of the field as shown in fig. 2; it is this term which dominates the flutter of our 120 degree symmetric field.

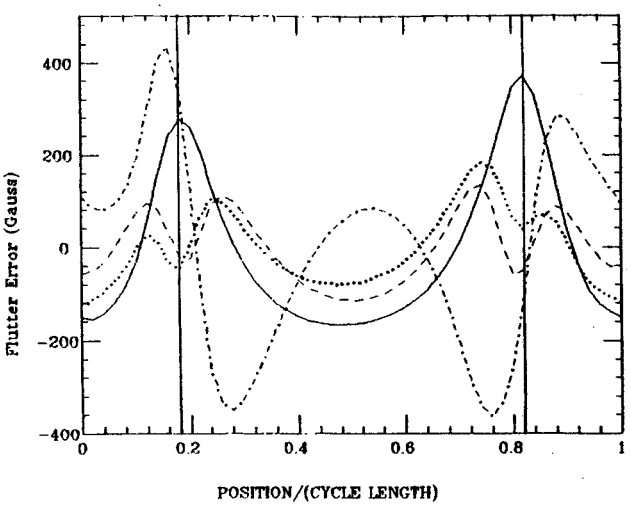

Fig. 3. Comparisons of flutter field after scaling to make the leading harmonic terms equal. Pole edges are marked with vertical lines. Solid curve is the difference between the real data and the original flutter calculation. Dots: same as solid curve except the calculated pole has no notch (see text). Dashed curve: two dimensional test. Dot-dash: Data minus two-dimensional POISSON (without any scaling).

If the amplitude of this harmonic term receives an ad hoc correction, the remaining errors occur at the pole edges, as shown in fig. 3.

The flutter error decreases with increasing field level. Table 2 lists the flutter error at three fields. Over this field range, the error changes from 3.5% to 2.4%. One would expect the effects of azimuthal components of the poles' magnetization to have a similar behavior. To test this hypothesis POISSON was again used to model the geometry. Fig. 4 shows the problem in POISSON form. This geometry was used as it closely matches the pole-valley geometry of the K800 magnet near r=0.5 m; the amount of iron removed with the bevel on the pole edge has the same area as that removed by the rounded pole edge described earlier. It is one cell out of an infinite lattice of identical cells. The vector potential is set constant along each vertical boundary, a Neumann boundary condition is required for the top and bottom surfaces, and a Dirichlet condition at the left and right boundaries. The field level is varied by

changing the potentials along the sides. The average field was subtracted from the result. The POISSON results were compared to a calculation of the same iron geometry (but without the edge bevel) in a uniform, vertical

Table 2

	Flutter Error (%)	
B_{avg} (T)	2-d	3-d
3.0	3.6	3.5
3.4		3.4
4.0	2.4	
4.7		2.3
5.0	1.6	

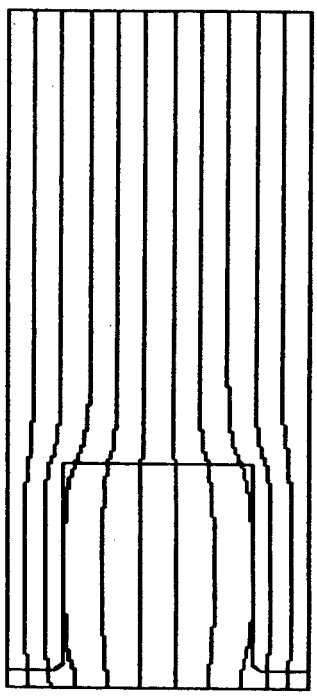

Fig. 4. Geometry used for POISSON study of flutter.

magnetization model; to form the lattice, the pole is repeated for 300 cycles of the lattice and the fields of the central cycle was used. Table 2 shows the results. As the POISSON results simulate the "real" field and the uniform magnetization calculation represents the original model for the cyclotron's poles, we see that our hypothesis as to the source of the flutter error appears to be correct: including the azimuthal components in the magnetization of the pole, the test model results give a field level dependence to the flutter error which is close to that of the error in calculating the field of the cyclotron. A new technique for calculating the flutter could therefore include a=step which the flutter calculated with the quasi- three dimensional uniform magnetization model is reduced by the fraction predicted by the comparison of the two dimensional POISSON and uniform magnetization calculations.

After performing the scaling just described, the remaining flutter error is at the pole edges. It was noted that the agreement between the 2-d calculations was distinctly better than that between the 3-d calculation and the data as shown in fig. 3. This was surprising in that while the 3-d calculation attempts to include the effect of the pole edge chamfer, the 2-d calculations have a bevel in the POISSON calculation but none in the uniform magnetization calculation. The 3-d uniform magnetization calculations were modified to remove the square notch and the resulting field compared to the data (again, after scaling the overall calculated flutter as described earlier). Fig. 3 compares the results to the earlier ones. The square edge worked equally well at all radii. The square edge does, however, increase the discrepancies in the overall flutter. The errors do not surpass 3.5% (after applying the correction deduced from the 2-d calculations) and occur at the inner end of the poles where the flutter is markedly reduced from the 0.2 m< r < 1.0 m region. The net result is an improvement in the flutter calculation at all radii. With these results, one might expect that the 2-d POISSON

calculations would be sufficient for an accurate representation of the flutter; fig. 3 shows this to not be the case. The 3-d aspects of the problem remain strong.

The accuracy of the flutter field calculation depends critically on the saturation field value used for the magnetization. While the value of the saturation field of the iron in our magnet is not precisely known, some sources give a value of 21.2 kG for low carbon steel while others give 20.8 kG. The calculations presented here used 21.4 kG as the saturation value of the magnetization. Reducing this value would accomplish the scaling suggested by the 2-d POISSON results. It is, nevertheless, intriguing that the inclusion of the azimuthal components of the poles' magnetizations accounts for the shortcomings of the original model without having to resort to changes in the 21.4 kG value. In particular, the peak-valley field difference of the POISSON calculation matches the real magnet quite well as seen in fig. 5. Using the default permeability table in POISSON which has a saturation value of 21.2 kG changed the 2-d flutter results by less than 0.5%, i.e. less than half the change in M. The effects of the detail of the permeability curve are still under investigation. Further discussion of this work can be found in ref. 5.

References

1. R. Holzinger, private comm.
2. L.H.Harwood and D.A.Johnson, Proc. of 10th Int. Cycl. Conf., (1984) 99.
3. L.H. Harwood and B.F. Milton, Proc. of 11th Int. Cycl. Conf, Tokyo 1986, in press.
4. M.M.Gordon and D.A.Johnson, Part. Accel. 10, (1980) 217.
5. L.H. Harwood, Particl. Accel. Conf., Wash. D.C. 1987, to be published.

MAGNETIC FIELD MEASUREMENTS OF THE NSCL K800 CYCLOTRON MAGNET

L.H. Harwood, B. Sherrill, J.A. Nolen Jr., and A.F. Zeller

The median plane magnetic field of the NSCL K800 magnet has been measured over its entire operating range and out to r=55 in. The results indicate that the magnet assembly and measurements were both quite good as deviations from symmetry are typically less than 5 G. Likewise, the first harmonic in the field is less than 10 G at all magnet excitations. The accuracy of calculating the change in the field by the addition of iron shims was also tested. Some of the results of these measurements are summarized here.

The measurement hardware has been described in detail previously[1]. The procedure is to measure the field at the center of the magnet with a NMR probe and then measure the difference in field at other points in the magnet relative to the center. The relative measurement is done with a search coil. The field was measured at over 300,000 points in the accelerated beam region of the magnet in about 1.5 hours. A test of the accuracy of our technique is how consistent the field is at various points that should have the same field. The magnet in the beam region (r=0.0-1.0 m) is designed with three-fold symmetry, ie. a structure is repeated at 120° intervals; our measurements should reflect this symmetry. Likewise, we should obtain the same field at 0.0° and 360.0°. Fig. 1 shows plots of the deviation from three-fold symmetry at two radii. The values are less than 0.7 mT with the peaks occuring at pole edges where the field gradient is 0.16 T/cm; the 0.7 mT thus corresponds to about 4×10^{-2} mm of position error in the pole or mapper. Close inspection reveals that the differences in the values at 0° and 360° are less than 0.05 mT. These checks are some of those used to determine the accuracy of the measurements and are obviously very encouraging in the face of high

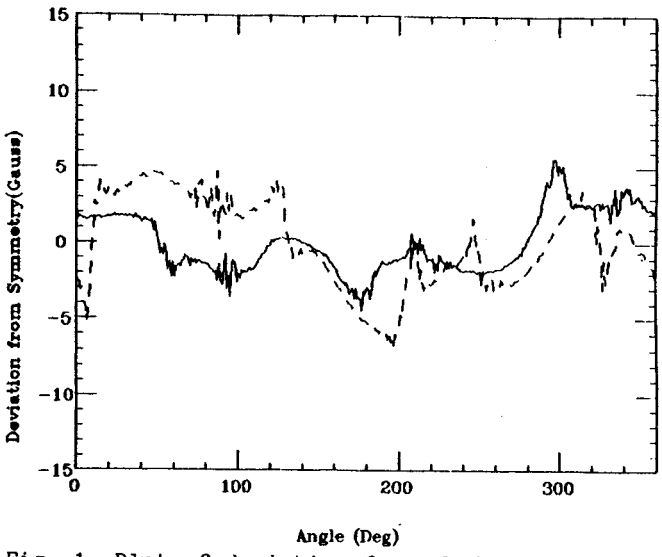

Fig. 1. Plot of deviation from 3-fold symmetry at r=10 in. (solid) and r=30 in. (dashed). This is for map full field.

fields and high gradients. Further analyses can be found in the references.

The first goal of the analysis of the fields was to check the manufacturing and assembly of the magnet's parts. The critical part of the assembly of this magnet was in making it three-fold symmetric. Many opportunities existed for breaking the symmetry ranging from fabrication errors to using bolts of the wrong material. Assembly accuracy can be tested in several ways. One can examine the first harmonic or second harmonic in the field, or, alternately, the absolute deviation from three-fold symmetry. Figure 1 gives a plot of the latter; fig. 2 shows the former two. We see that the first harmonic in the field is less the 10 G, which is within the range of the trim coils to correct. We also see a small peak in the second harmonic near the center. This could be an indication that the center plug and pole tip inner extensions may not be aligned with the rest of the machine or that the center of the coordinate system used for the harmonic analysis was offset from the "real" center. The

deviations from three-fold symmetry indicate that the poles are symmetrically machined and installed to an accuracy of approximately 0.05 mm. The large derivative in the first harmonic outside 89 cm is indicative of several possibilities. First, we could be seeing some effect from an off-center bobbin; second, one or two poles could be shifted radially relative to some chosen "reference" pole; third, the bobbin may not have an azimuthally constant vertical gap.

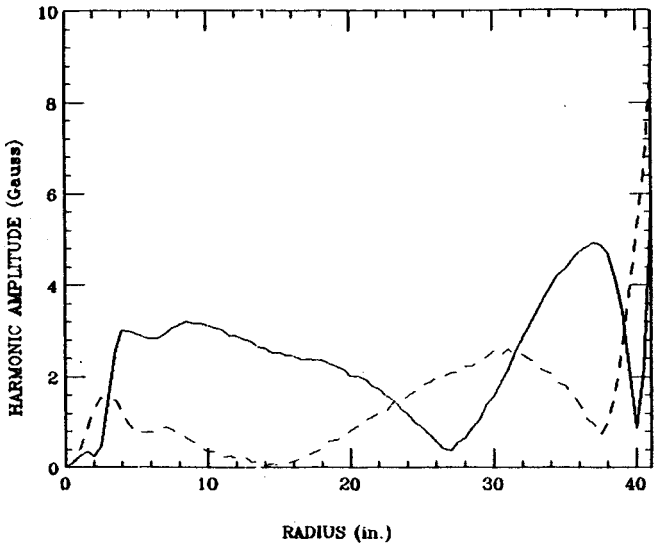

Fig. 2. Plot of the amplitudes of the first harmonic (solid) and second harmonic (dashed) in the field.

The ability to correct the imperfections in the field was tested by comparing two fields: one unshimmed and the other with shims based on the calculations of what was needed to remove the large gradient in the first harmonic. The calculations showed that 0.76 mm thick shims placed on two of the pole edges would greatly reduce this derivative. These shims were installed with the result shown in fig. 3 where the original first harmonic is compared to the first harmonic after shimming The first harmonic obtained in the calculations is not shown because it was so closely the same as the final measurements that they would be nearly indistinguishable in the plot. The agreement between measured and calculated shimmed fields was heartening.

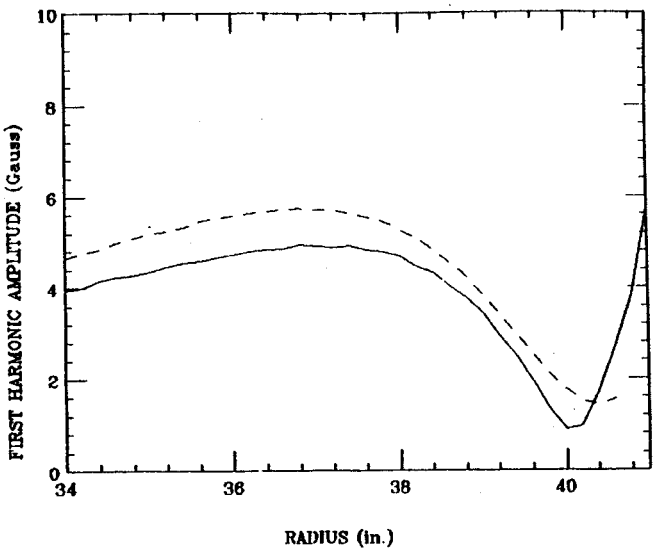

Fig. 3. Plot of the amplitude of the first harmonic in the field before shimming to remove the large derivative (solid) and after insertion of the calculated shim (dashed).

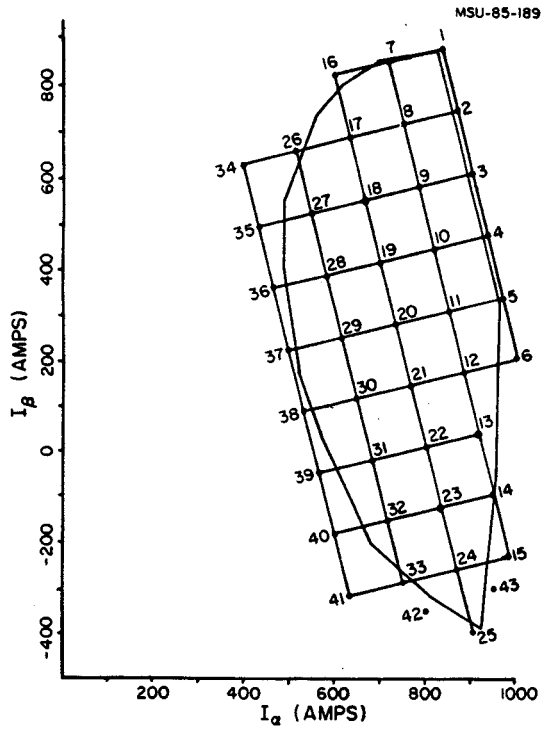

Fig. 4. Grid of points used as basis for mapping. Operating region of the magnet for real beams is shown with the full line.

The main field of the magnet was mapped in 0.1 in. radial steps and 0.5° angular steps at 25 different excitations distributed in a rectangular array over the magnet's operating region. At 4 of these points, the field of each of the 21 trim coils was measured. Additionally, at 19 of the excitations the

magnet's field outside the acceleration region was sampled at 15 angles spread over 130°.

The body of data acquired on magnet field of the K800 magnet is far too great to present in detail in this report so a brief summary will be presented instead:

a) Azimuthally average fields - The average fields measured vary smoothly with coil excitation and follow the basic trend of the calculated fields[3].

b) Field errors - The important first harmonic in the field is less than 10 G in the accelerated beam region at all excitations. It varies smoothly with radius and has no well localized source until r= 1 m is reached, where it undergoes a rapid change. The source of this rapid change has yet to be found; however, small shims were able to greatly reduce the change. The remaining excitation dependence of the first harmonic could be due to one or more of several sources; these include pole motion, incomplete compensation of the yoke median plane penetrations, and coil motion. An analysis which examined the differences between various excitations and one reference excitation found the largest difference to be concentrated at large "beta" coil excitation; the ramifications of this on the analysis is still under study.

c) Shimming - After a first mapping cycle, shimming is often found necessary to achieve the desired orbital characteristics. The success achieved in pre-calculating the shims necessary to reduce the gradient in the first harmonics near r = 1 m indicates that we will be able to do that operation quite reliably should it be necessary.

In conclusion, we have developed a system which can produce highly reliable, highly accurate maps of a high field magnet with large gradients. This system has been used to measure the field characteristics of the NSCL K800 cyclotron magnet. The results show that the magnet was machined and assembled quite well with very good adherence to tolerances. Further, all observables in the field vary smoothly with radius, angle and coil excitation. Our ability to accurately place the coil based on analysis of the fields agrees with force analyses. Finally, shimming, if necessary, can be done reliably based on calculated shims.

References

1. L.H. Harwood and J.A. Nolen Jr., Proc 10th Int. Cyc. Conf., (1984) 101.
2. L. Harwood, et al., IEEE Trans. of Nuc. Sci. 32 (1985) 3734.
3. L.H. Harwood and B.F. Milton , Proc. 11th Int. Cyc. Conf., (1986) Tokyo, in press.

DESIGN OF HARMONIC COMPENSATION HOLES IN THE MEDIAN PLANE SECTION OF THE K800 MAGNET YOKE

L.H. Harwood

Many holes are needed in the median plane section of the return yoke of the K800 magnet; these holes accommodate the myriad of extraction elements, beam extraction channel, beam injection channel, and coil centering links necessary for this cyclotron to work. The holes are not symmetrically placed, however, and if left uncompensated would produce a large first harmonic in the field which could be disastrous for the beam.

A procedure for this compensation was outlined in the 1983-84 annual report; one compensates the field by compensating the harmonics in the iron distribution for the "ring" of iron at a given r and z independently from all other rings. This ensures that the field compensation works equally well at all radii. At each r and z, two holes are added to the array so as to eliminate the first and second harmonics in the iron at that r and z; two holes are the minimum necessary to accomplish this. The net result is to achieve the compensation with a minimum in removed iron. It was commented in the earlier report that the final design of the extraction system and the holes it necessitates would require a final design of the compensation holes. The final extraction system has now been designed and its compensation holes calculated. Some examples of the array of holes are shown in the figs.

Holes shaped exactly like the calculations proved difficult to machine. The field of the section of the yoke in question was calculated in the limit of uniform, vertical magnetization. A value of 1.5 G was found for the first harmonic at the radius of the $n_r = 1$ resonance; this residual was compensated during the compensation of the coil tank outer wall, ie. the first harmonic of the final set of holes in the tank wall have a first harmonic which cancels that coming from the yoke.

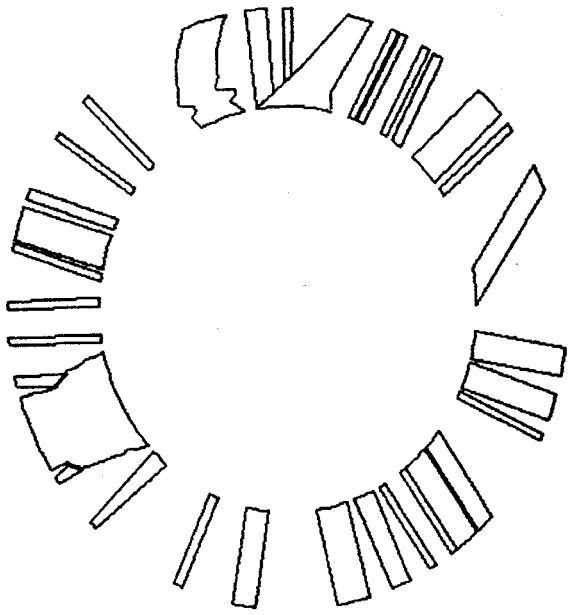

Fig. 1. Penetrations in K800 cyclotron yoke median plane from 0.0" to 1.125" from the median plane; compensation holes are included. N.B.: the penetrations are the enclosed regions, not the open regions.

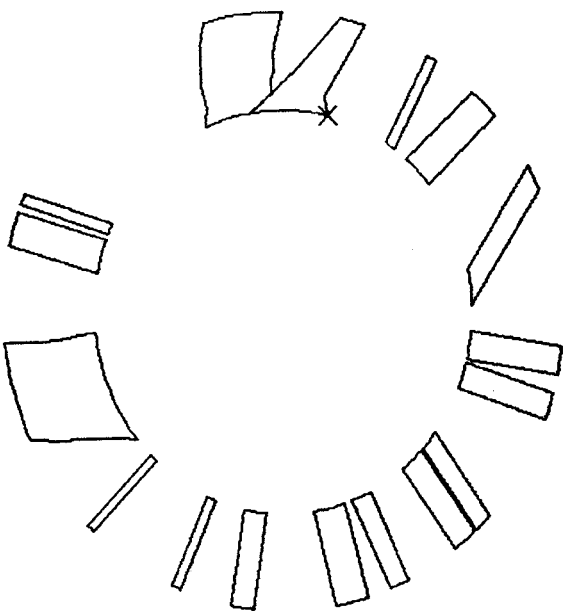

Fig. 2. Same as Fig. 1 but for 1.125" to 1.75" from the median plane.

THE K800 EXIT BEAMLINE DESIGN

A.F. Zeller, J.A. Nolen, R.T. Swanson, and R.D. Hay[a]

In order to transport the heavy ion beam from the NSCL's K800 superconducting cyclotron from the extraction system exit, through the return yoke, to the external beamline, a system of quadrupoles and dipoles is necessary. Because of the small cross sectional area of the exit channel, 18 x 18 cm^2, and the requirements for adjustable elements which do not cause fringe fields to extend into the cyclotron's interior, permanent magnets[1-4] (PM) were chosen.

In the transition phase, the beam will be transported to the 92" chamber. The layout of the system is shown in Fig. 1, with the lumped PMs in the exit channel, and the other elements necessary to provide the required 26° of total bend and the proper focusing to the target of the 92" chamber. (There is also space for the 4π detector and other apparatus in their area, but these devices are not shown in this figure.) In addition to the elements shown, the external cyclotron fringing field will provide approximately 2° of bend for all beams, and the field in the yoke provides an average bend angle of 6°. Because of the non-linear saturation of the return yoke, the bend by the field in the yoke would range between 4° and 8° for momenta of 1.0 to 1.6 GeV/c. This will be corrected to 6° for all beams by use of an adjustable PM dipole, 8" long consisting of counter-rotating ring segments, capable of providing 2° of bend at 1.6 GeV/c. A second similar PM dipole outside the yoke provides an additional 2° deflection. Adjustable PM quadrupoles, arranged as a doublet consisting of four 6" segments together with a superconducting quad doublet further out, reimage the beam at the exit image box. The PM system is shown in Fig. 2. The optical design provides for both point-to-point and waist-to-waist imaging in both planes. The final system differs slightly from that shown in Fig. 2, with all elements the same outside diameter.

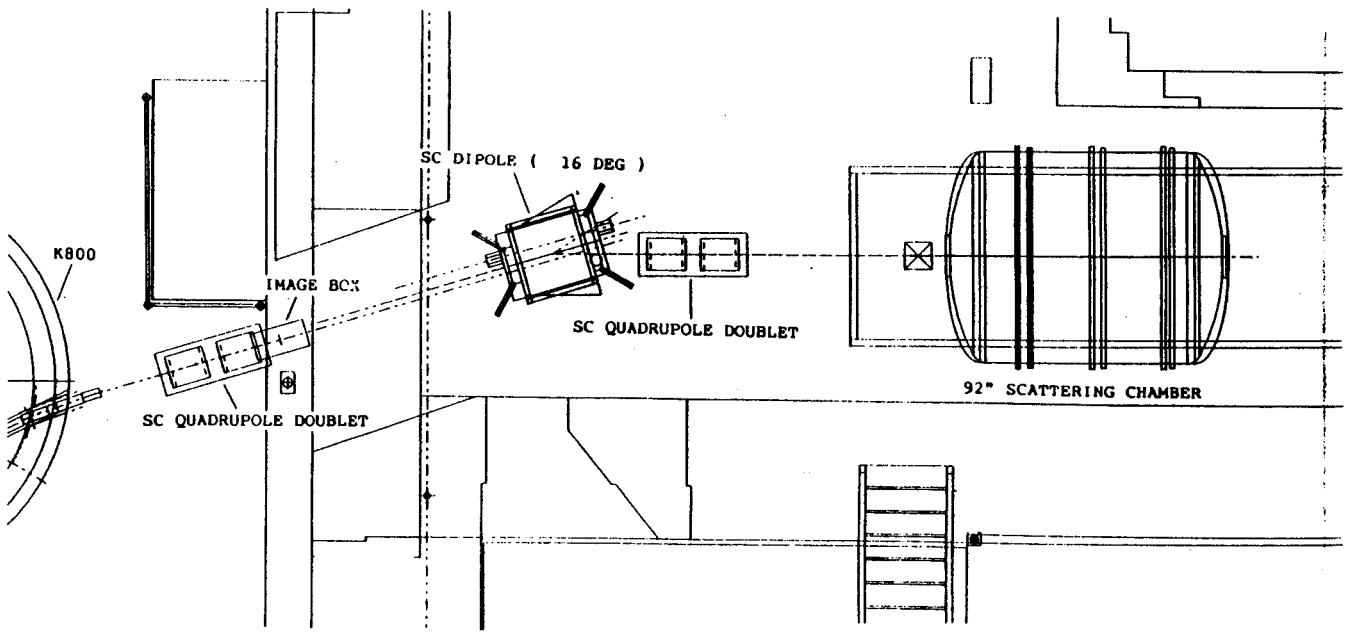

Fig. 1 Layout of the transitions phase when the K800 will be providing beam to the 92" chamber.

PANDIRA calculations for the dipole and quadrupole ring segments are shown in Figs. 3 and 4, respectively. The inner diameter is 1.56" and the outer 4". Each ring segment is 1" thick and is composed of 12 individual trapezoid pieces whose magnetization directions are arranged to produce the desired field shape. The design is for field uniformity to be better than 1.5% at 80% of full radius. After extensive testing of different materials (see other contribution), a high magnetization, high coercivity type of SmCo was chosen over Nd Fe B. With a specified residual magnetization of 10 kG, the peak quadrupole gradient is over 13 kG/in (52 T/m) and the dipole field is 8.6 kG.

Detailing of the mechanical drive system which will rotate the segments with respect to each other is underway and the PM material is out for bid.

---

a. Private Consultant

References

1. R.I. Gluckstern and R.F. Holsinger, NIM 187, 119 (1981).
2. K. Halbach, NIM 169, 1 (1979).
3. K. Halbach, IEEE Trans. Nucl. Sci, NS-26, 3882 (1979).
4. R.D. Hay and C.G. Masi, Proc. 1981 Linear Acc. Conf., 84.

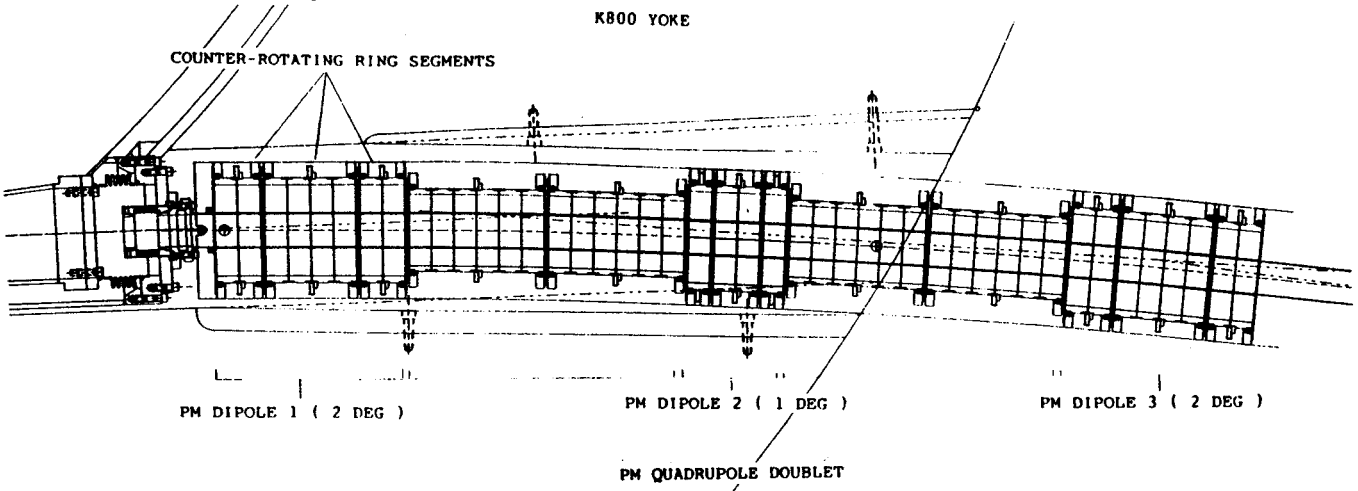

Fig. 2. PM dipoles and quads in the K800 exit channel. The counter-rotating segments of one of the dipoles are shown. Note that the 4 segment inner section rotate with respect to the two coupled outer sections.

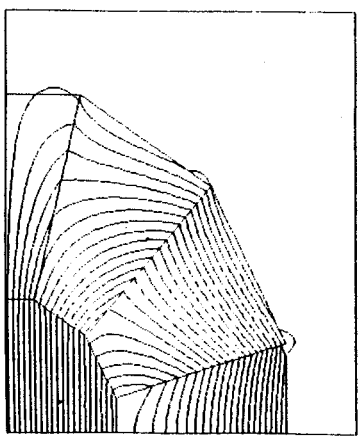

Fig. 3. PANDIRA calculation of one quarter of a 12 segment dipole.

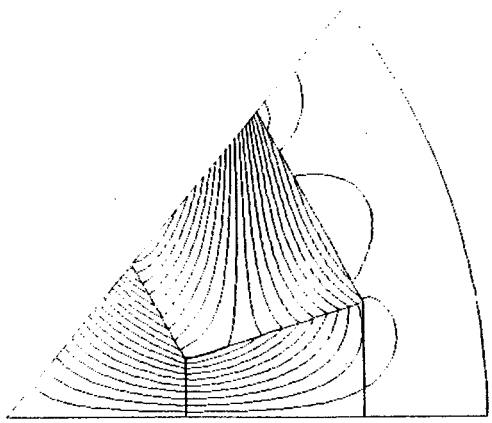

Fig. 4. PANDIRA calculation of one eighth of a 12 segment quadrupole.

PHASE PROBE TESTS

R.M. Ronningen, B.F. Milton, J. Yurkon, M. Maier, and F. Marti

Last years annual report described a prototype gamma ray detector based on a pin diode. Its function is to detect gamma rays from the internal beam striking the viewer port probe tip. Also in that annual report a phase slit system was described. The gamma ray probe was used this past year to measure the phase width of the internal beam using the phase slits.

The phase width of the beam is determined by measuring the time distribution of gamma rays relative to the cyclotron rf. Therefore the detector's time response must be known and unfolded from the measured time distribution. We operated a bare diode, as opposed to one coupled with a scintillator, because the detector is placed in the cyclotron, in close proximity to the probe tip where low detection efficiency should be a small problem. By not using a scintillator one can take advantage of the fast response of the diode without the problems of coupling the scintillator to the diode and the time response of the scintillator. Unfortunately an important drawback of the diode we chose is that its efficiency to gamma detection is so small that its time response cannot be easily measured with gamma sources in the usual way on the bench.

We measured the time response of the detector using a fast (10 psec) pulsed laser and the risetime was less than 500 psec. This upper bound was set by the accuracy of the measurement, not the diode. In addition, the detector was compared to a small BaF detector. To do this, both detectors were used to measure the external beam's phase width and the results compared. The BaF detector was known to provide less than 300 psec FWHM time response. Figure 1 shows the two time spectra, which look quite similar.

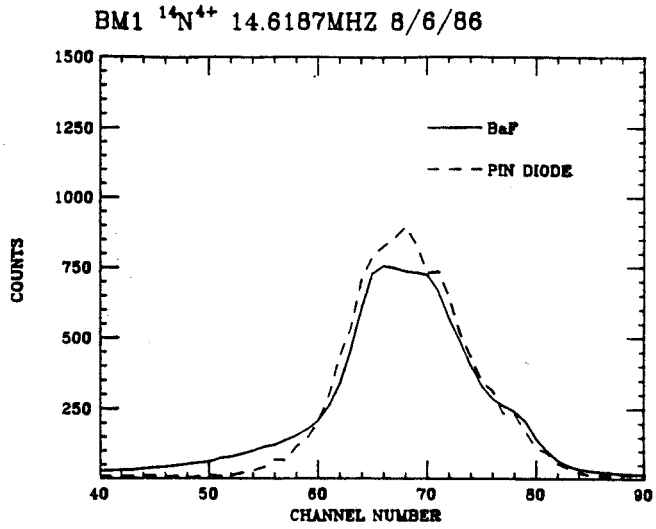

Figure 1. A comparison of the pin diode detector with a BaF scintillator detector. The figure shows the time spectrum of gamma rays relative to cyclotron rf.

The detector was then tested in the cyclotron with the phase slits described last year. The temperature in the probe tip was too high for the diode to survive, so air cooling was added. The detector's sensitivity appeared to be a function of radius, with the highest detection efficiency in the extraction channel. It also showed a strong response to the location of the phase slits, thus verifying its usefulness. Figure 2 shows some representative data.

The sensitivity of the detector to position leads us to believe that it is responding with greater efficiency to particles produced by the beam or a portion of the beam hitting the detector directly. We will be using an avalanche photodiode in future tests to increase the efficiency to gamma detection. We are also working on a wavelength shifter so that if a small crystal of BaF is necessary its fast timing component can be detected by the diode.

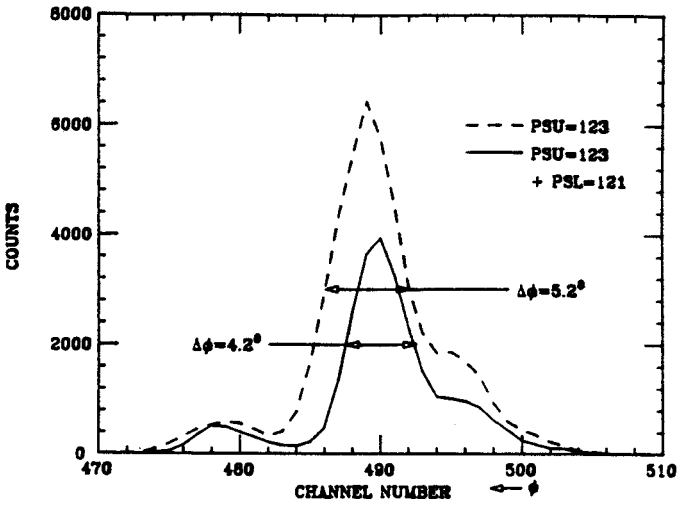

Fig. 2. A comparison of the phase width at extraction radius when one and when two phase slits are introduced. "PSU, PSL" denote upper and lower slit position readout values.

RADIATION EFFECTS ON PERMANENT MAGNET MATERIALS

A.F. Zeller and J.A. Nolen

The exit channel design, presented in a separate contribution to this Annual Report, uses the unique features of Permanent Magnet (PM) materials. However, the hostile environment, including a magnet field of 6.6 kG in the exit channel and large radiation doses from a combination of high energy neutrons and charged particles makes the choice of material particularly critical. The transport of high rigidity beams requires high fields and gradients, resulting in places within the magnets having very low permeance coefficients, P_c, and the superimposed external field drives many parts of the magnets into the third quadrant. The permeance coefficient is a measure of the demagnetization strength and is defined by $P_c = B/H$, where B is the magnetic induction in kG at a given point within the material and H is the demagnetization field in kOe at that point.

In the second quadrant of the B-H curve, P_c is a negative number, and can vary from 0 to $-\infty$. Samples pushed far into the second quadrant have small negative values of P_c and are more "loaded". A P_c of -0.1 is calculated to be present in some parts of our exit beamline PM rings. Therefore tests were carried out on four candidate materials in low P_c configurations, i.e. thin samples magnetized perpendicular to the thin dimension. The materials, kindly supplied by IG technologies, are listed in Table 1. Additionally, two other materials, not available at the start, were also tested in parts of this study. They were supplied as cylindrical disks with a P_c=-.7. The minimum P_c for the NeIGT-27 sample is -0.12 while the other three thin samples had P_c=- 0.2. The maximum P_c=-0.24 for these three is obtained near the outer edges of the rectangular segments.

Table 1

Material		Residual Induction (kG)
NeIGT-27	NdFeB	10.8
NeIGT-27H	NdFeB + Dy	10.2
INCOR-18	Sm_1Co_5	8.8
INCOR-22HE	Sm_2Co_{17}	9.6
*NeIGT-27KM	NdFeB + Dy	10.4
*NeIGT-24K	NdFeB + Dy	10.0

* Supplied in 10mm thick cylinders.

Temperature Tests

The operating PM's will be kept at room temperature since they are thermally anchored to the 260 ton cyclotron, so only beam heating need be considered. Interlocks will assure than any temperature rises will be small, therefore testing for irreversible losses was only conducted to 55°C. Magnets were mapped with either of two search coils, using the MSU magnet mapping system. The large coil measured the total flux changes, while the small coil mapped the microscopic features with a linear step size of 0.15 mm. Overall irreversible losses at 55°C were 17% for the NdFeB while the higher coercive 27H and Sm_2Co_{17} suffered only 1% loss. The 1:5 material showed no loss. Detailed maps of the NdFeB magnets showed that the middle of the magnets (P_c=-.12) suffered five times the magnetization loss as the higher P_c edges. This means that a PM constructed with NdFeB would show an overall loss in strength of only a few percent, since the average P_c=-1, but that areas of low P_c would suffer significant losses, leading to the addition of undesirable higher order multipoles.

Gamma Irradiations

Other samples were also irradiated with gamma rays in a ^{60}Co source at a rate of 100 kilo-rad per hour, with a maximum accumulated dose of 50 mega-rad. The maximum temperature rose to 28°C. The results are shown in figs. 1 and 2. It is not surprising that the SmCo samples were unaffected, since a study[1] at TRIUMF with 500 MeV protons showed SmCo to be sensitive only in the giga-rad range. The small increase in strength seen for SmCo is observed in all phases of this work. Temperature studies showed a small initial rise, before a final decrease at about 45°C. All radiation studies showed the same trend. This has been attributed to a process called thermal remagnetization.[2] However, the effect of P_c is even more pronounced in the NdFeB with gamma irradiation. The high P_c regions were virtually unchanged, while the center (P_c =-.12) region decreased in strength by over a factor of two.

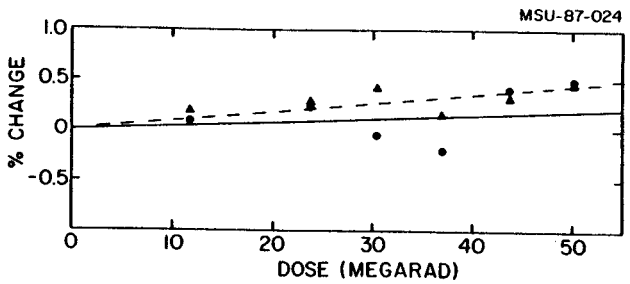

Fig. 1. Change in magnetization after irradiation with ^{60}Co gamma rays for $Sm_1 Co_5$(O) and Sm_2Co_{17} (Δ). The lines are best fits thru the data.

Deuteron Irradiations

Previous studies[1] of flux losses for samples of unspecified P_c during high energy proton irradiation shows that Sm-Co magnets withstand giga-rad, but that NdFeB suffered 50% demagnetization after only 40 mega-rad. This more than 1000x greater sensitivity of NdFeB was surprising. We decided to carry out similar studies of samples with low P_c. We irradiated samples of all six materials with 106 MeV deuterons from the K500. The samples were

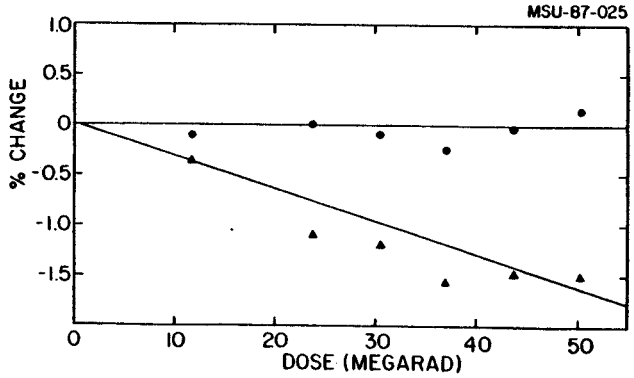

Fig. 2. The same as figure 1, but for NeIGHT-27 (Δ) and 27H (O).

mounted on a thin sheet of soft iron which had been coated with a phosphor to allow monitoring of the irradiation uniformity. (The iron backing increased P_c by 10% for the thin samples.) At a beam current of 1nA per square inch the dose rate was ~0.5 mega-rad per hour. Since this is only about 40 milliwatts of power in each magnet, no heating was expected. This was verified with a thermocouple attached to the iron sheet. Initial doses of up to 3 mega-rad were obtained. The results are shown in fig. 3. Autoradiograms were taken to determine the dose uniformity. Only in the case of the NeIGT-27 at 2.6 mega-rad was a nonuniformity observed. The point in fig. 3 has been corrected for this effect by scaling the detailed map to the total flux map. Detailed maps of NeIGT-27 are summarized in fig. 4. The extrapolated linear decrease for 2 to 3 mega-rad for NdFeB, shows as the solid lines are not followed. The cause of this is probably some remagnetization caused by the presence of the other magnets and the iron sheet.

The very large losses for NdFeB materials when struck by charged particles, in confirmation of the earlier studies, causes us to choose SmCo as the material needed for the exit beamline magnets, since it is impossible to guarantee that the magnets will never be hit with direct beam.

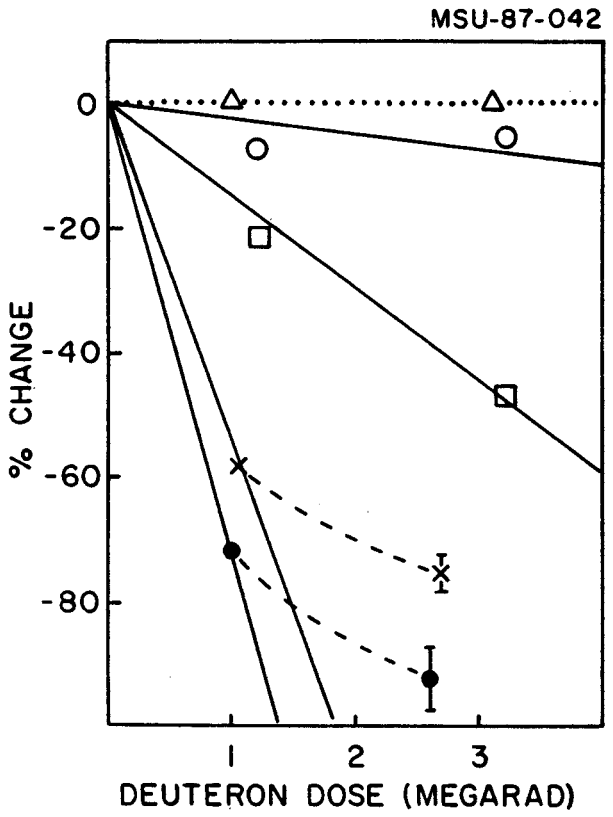

Fig. 3. Change in magnetization following 106 MeV deuteron bombardment. Symbols represent: NeIGT-27 (filled O), 27H (X), 27KM (□), 24K (o), and SmCo(Δ). Sm_1Co_5 and Sm_2Co_{17} showed the same losses.

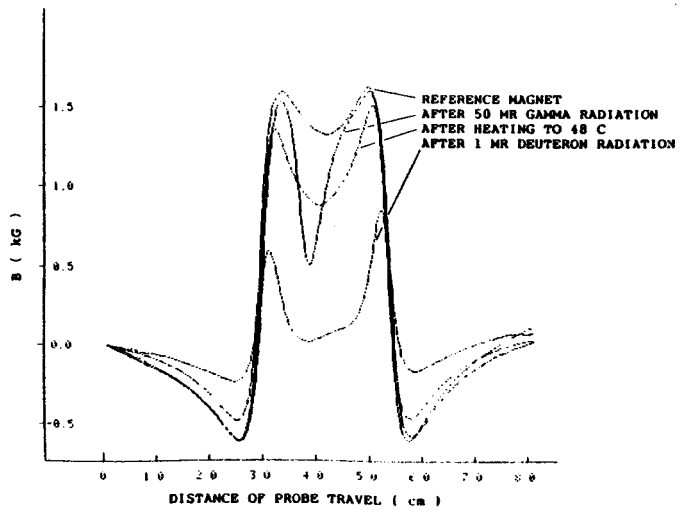

Fig. 4. Detailed maps of NeIGT-27 after heating and irradiations.

We wish to thank M. Bohlmann of I.G. Technologies for supplying the magnets and for many useful conversations.

References

1. E.W. Blackmore, IEEE Trans. Nucl. Sci., NS-32, 3669 (1985)
2. M.A. Bohlmann, private communication.

EFFECTS ON A BEAM OF PROLONGED WEAVING AROUND THE $\nu_r = 2\nu_z$ COUPLING RESONANCE

M.M. Gordon, F. Marti, and X.Y. Wu

The importance of the $\nu_r = 2\nu_z$ coupling resonance has been recognized for a long time since it occurs in the extraction region of most cyclotrons where it severly limits the achievable turn separation. If the radial displacements become too large, the resultant coupling action will cause the vertical height of the beam to grow beyond the allowed aperture with a resultant loss in current.

In superconducting cyclotrons, the values of ν_z generally rise when the extraction energy for a given ion is lowered. One can therefore find operating conditions where the beam repeatedly crosses the $\nu_r = 2\nu_z$ resonance well below its final energy. A good example occurs in the K800 cyclotron for a charge q/A = 0.5 and final energy E_f/A = 142 MeV. Here we find that between 55 and 115 MeV, the average value of ($\nu_r - 2\nu_z$) is 0.012 while the rms value is 0.026. This energy range corresponds to 300 out of the total 700 turns executed by the beam.

The effects on the beam of this coupling resonance were investigated using the Z[4] Orbit Code which is ideally suited to this purpose. This code uses exact equations of motion and magnetic field components which are correct to fourth order in z.

The orbit computations start well below the resonance at 30MeV and go 500 turns to 131 MeV, about 50 turns before extraction. The starting conditions for (x,p_x) and (z,p_z) were chosen to lie on eigenellipses having maximum areas that correspond to an extracted beam with final emittances of 10 mm-mrad radially and 20 mm-mrad vertically. These values are about twice those that would be expected from the K800 cyclotron if one simply extrapolates the measured emittances from the K500 cyclotron.

Some of the results obtained from these studies are summarized in the accompanying figure which shows phase plots for the radial and vertical motion at the end of turns 100(50

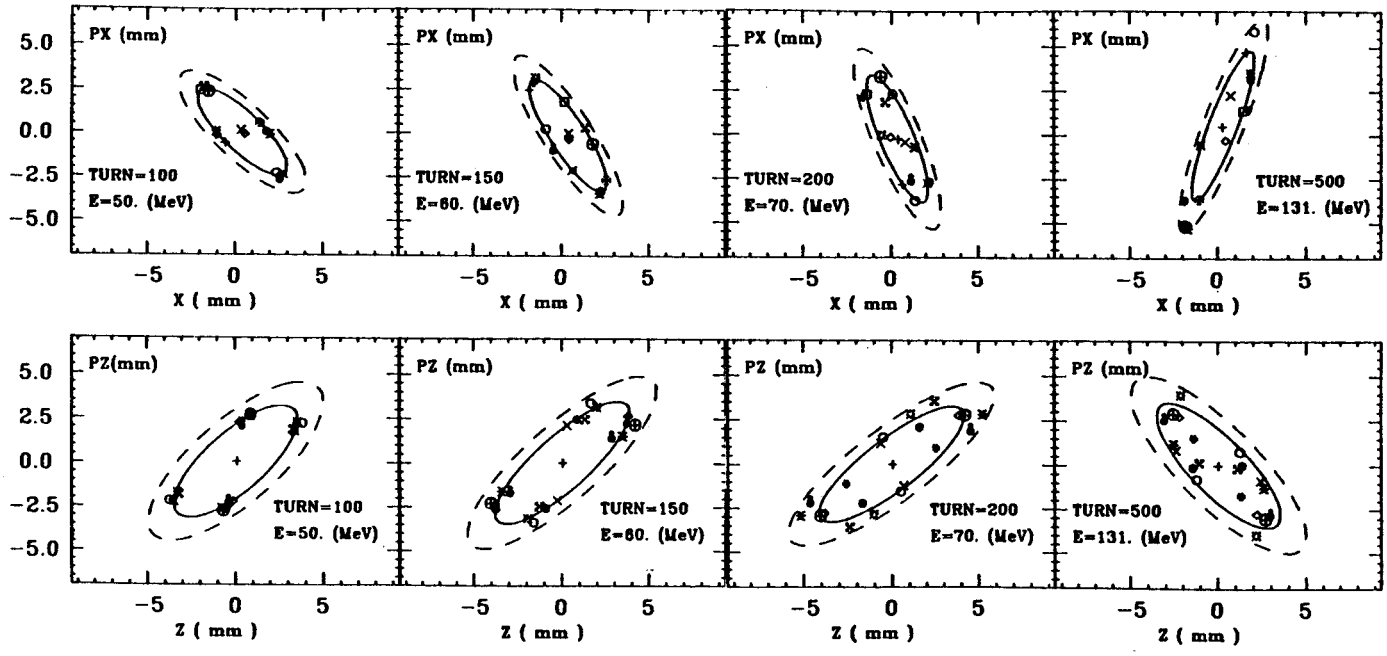

Fig. 1. Plots of p_x versus x (top) and p_z vs z (bottom) for 15 orbits on turns 100, 150, 200, and 500. These plots show evolution of points from an initially ordered state to a chaotic one. Solid eigenellipses have the same areas as the initial ones in Fig. 2, while broken eigenellipses represent theoretical upper limits for the growth in these areas.

MeV), 150(60 MeV), 200(70 MeV), and 500(131 MeV). Solid curves are used to show eigenellipses at each energy having the same areas as those used for the initial conditions at 30 MeV. The eigenellipses shown as broken curves indicate the upper limit for the growth in areas resulting from this coupling resonance according to the theory. These areas correspond to final emittances of 20 mm-mrad radially and 40 mm-mrad vertically which are just twice the initial values given above.

The results shown for turn 100 demonstrate that the motion is fairly linear from 30 to 50 MeV since the plotted points remain bunched together near the original eigenellipses. However, the situation changes rapidly from 100 to 200 turns (50-70 MeV) where the distribution of points becomes progressively more disorganized and continues to be quite chaotic from then on. Nevertheless, the points all remain within the theoretical limits noted above in all the plots shown here, and exceed these limits only intermittently during all the intervening turns.

The program also records the maximum height Δz of the corresponding beam on each turn, and the resultant values show that Δz = 10mm initially, reaches a peak value of 14 mm at turn 425 (115 MeV), and ends up at 12 mm on turn 500(131 MeV). This growth in height is quite consistent with the theoretical limits for the growth in vertical emittance noted above.

These results look very encouraging since they indicate that no beam loss will occur and that there will be at most a factor of two growth in emittance values. This coupling resonance is, however, nonlinear so that its effect depends quite strongly on the conditions of the beam prior to the resonance. We have assumed here that all of the orbits start out well-centered and with the same initial phase at 30 MeV, and although these assumptions might seem quite restrictive, they are fairly well compensated by our use of initial emittance values which are at least twice those expected for the K800 cyclotron. A more detailed report on these studies will appear in the Proceedings of the International Cyclotron Conference held in Tokyo during October, 1986.

ANALYTICAL PERMANENT MAGNET DESIGN CODE PERMMAG

Z.Q. Xie and T. Antaya

An ECR Ion Source requires a large multipole magnet for the radial component of the magnetic bottle, which normally is built of rare earth cobalt permanent magnets. The production of permanent magnet pieces as large as ECR magnet poles is technologically very difficult even without considering the cost. So the large multipole magnet generally is an assembly of many small permanent magnets (see Fig. 1). The small permanent magnets are not magnetically identical because of manufacturing defects which result in a variation in magnetization. Mechanical assembly errors can also not be avoided. How do these defects affect the multipole field? To examine these issues, an analytical field calculation has been developed to computer the net fields due to individual magnet pieces or complete multipoles. This calculation is based on 2 assumptions: (1), that there is a high anisotropy in the magnetization direction (which holds generally for high field rare earth magnets), and (2), that this magnetization is uniformly confined to a plane. The code gives all 3 components of the magnetic field for multipoles using rectangular or trapezoidal pole shapes.

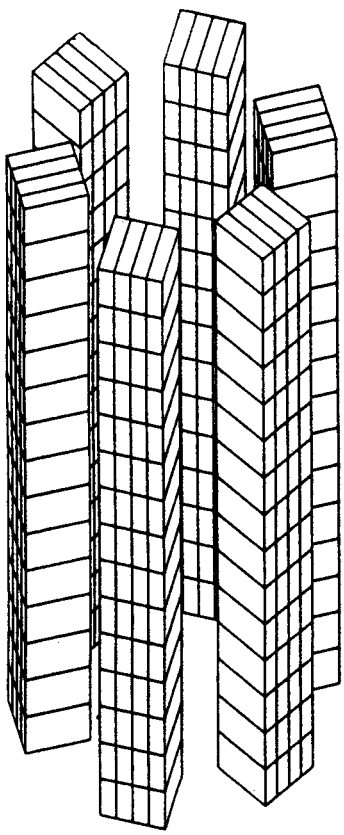

Fig. 1 Representation of the hexapole in the NSCL RT-ECR, which consists of 360 pieces of 2"x2"x.5" $SmCo_5$ magnets.

For a finite trapezoidal magnet as shown in Fig. 2, we make the assumption that the magnetization inside the permanent magnet is uniform and lies in the x-y plane. We do a charge sheet calculation,[1] and find that the total demagnetization field for this magnet has the form;

$$\vec{H} = \vec{H}_1 + \vec{H}_2 + \vec{H}_3 + \vec{H}_4$$

where $\vec{H}_i$ is the field produced by the charge on the i-th side surface indicated in Fig. 2. The assumption that the magnetization was confined to the x-y plane was used to eliminate the top and bottom surfaces. The magnetic charge density in the surface is given by

$$\sigma_m = \vec{n}.\vec{J} = J\cos\Phi = \mu_0 M\cos\Phi = B_{rm}\cos\Phi$$

where Φ is the angle between the outer normal and the magnetization direction. B_{rm} is the residual induction.

We desire to calculate the net magnetic field at point (X,Y,Z) by integrating over surface coordinates (x,y,z) as shown in Fig. 3. The field at point (X,Y,Z) produced by charge $\sigma_m da$ on the i-th surface at (x,y,z) is of the form:

$$d\vec{H}_i(X,Y,Z) = \frac{\sigma_m \vec{r}_i da_i}{4\pi\mu_0 |\vec{r}_i|^3}$$

where $\vec{r}_i = \vec{R} - \vec{r}$

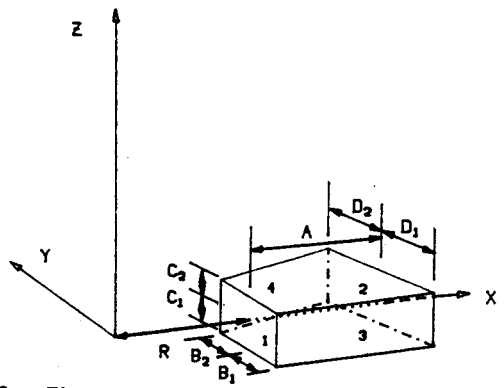

Fig. 2 The representation of a trapezoidal shaped permanent magnet for the PERMMAG calculation is shown.

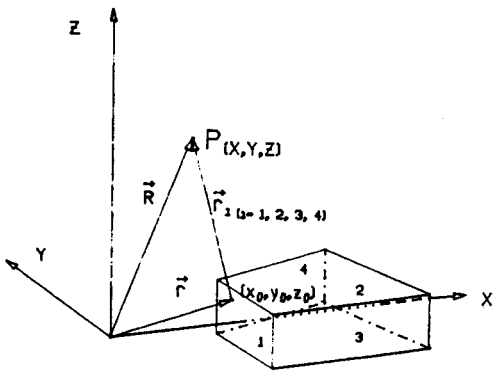

Fig. 3 The components of $\vec{B}$ at P (X,Y,Z) are computed from charge sheet integrals over the magnet surface.

thus $$\vec{H}_i(X,Y,Z) = \frac{\sigma_m}{4\pi\ \mu_0} \iint \frac{\vec{r}_i\, da_i}{|\vec{r}_i|^3}$$

The total field for trapezoidal pieces is obtained by adding the contributions from all surfaces. The complete formulation of the solution is found in report "An Analytical Calculation of Multipole Field Produced by Oriented Permanent Magnets".[2] When $B_1=B_2=D_1=D_2$, the calculation reduces to that for a rectangular block, and additionally if the magnetization is coincident with the X-axis, the formulae reduce to those given by Thome and Tarrh's formula for the magnetized block of finite length.[3]

What we have obtained so far is the field due to a single permanent magnet block. Multipole fields will be obtained by superposition from this basic result. We would first like to demonstrate the validity of the basic calculation, the field along a line normal to the surface of a rectangular REC magnet (A=1.98, B=D=2.06, C=.525 in, B_{rm}=8.7 kG) at the center of a pole, is compared to the measured field using a calibrated hall probe. The results of this comparison are found in Table I.

Table I

Y (in)	By (kG)	
	measured	calculated
.02	3.96	3.968
.44	1.20	1.243
.94	.46	.468
1.44	.223	.225
1.94	.127	.125
2.44	.077	.077
2.94	.051	.050
3.44	.036	.036
3.94	.026	.027
4.44	.019	.019

Note: Y is the distance away from the pole surface at the pole face center.

As can be seen, the calculation for a single magnet agrees well with the measured field.

In the RT-ECR, a pole consists of 4 such rectangular blocks that are glued together (see Fig. 1). We also did a calculation of 4-group with slightly different residual inductions. Again there was a good agreement between the calculated and the measured fields, as shown in Fig. 4. Note that for small displacements from the pole surface the measured field shows sharp peaks. This assembly defect is the result of misalignment of the edges of the 4 pieces in the group. The effect washes out rapidly in a distance that corresponds to the plasma chamber wall thickness (0.3 in) so that the source does not see the sharp peaks.

One can use this calculation to explore multipole assembly issues - such as how to mix

pieces with varying strength to achieve an overall uniform field. As Fig. 5 shows, the effect of mixing $\bar{B}_{rm}$ + 2% and $\bar{B}_{rm}$ -3% pieces is washed out at 0.4 in from the surface. Variations of ± 1-3% are typical in REC magnets.

The success with calculations of individual elements led to construction of a generalized code "PERMMAG" to calculate permanent magnet multipole fields in 3-dimensions via the superposition principal. In this code there is the additional simplification that poles made smaller pieces shall be treated as a single piece. One can easily verify that this is correct if all pieces in the pole have the same magnetization. It works also if the variations in magnetizations are small. In ECR magnet design calculations one always assumes entirely uniform magnetization, later, after the construction pieces have arrived and strength variations determined, the effects of possible large fluctuations can be studied with a variation of PERMMAG. In order to specify the multipole geometry in a generalized way, we

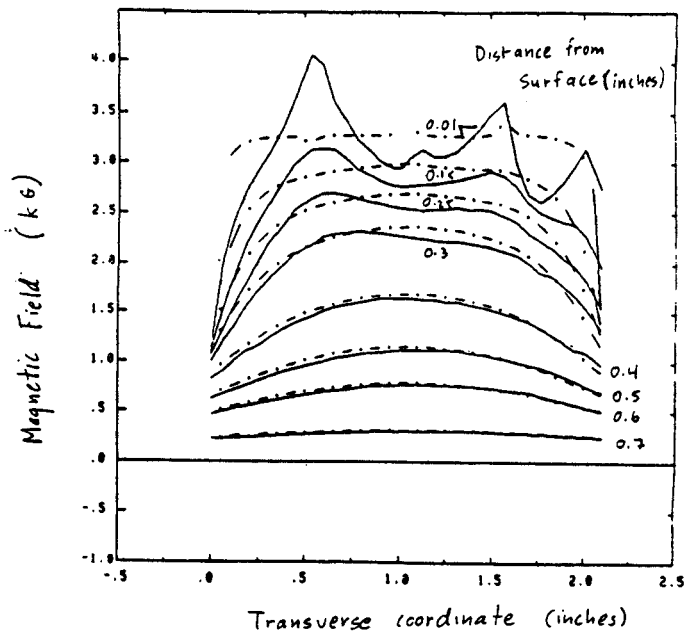

Fig. 4 The accuracy of the 4-group assembly is important - here the measured normal component of a 4-group with 4 same strength pieces is compared to the ideal field. Near the surface, the sharp peaks in the field are the result of mis-alignment of the pieces edges.

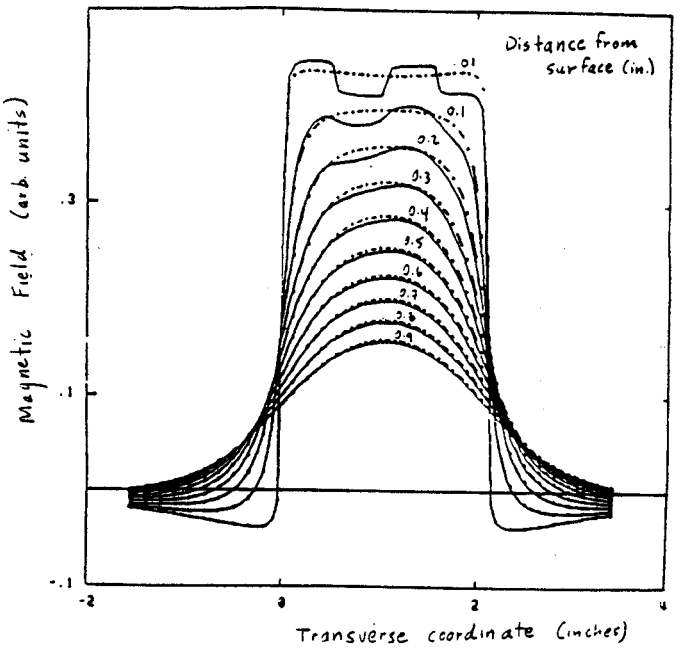

Fig. 5 A comparison of the calculated magnetic field at distances normal to the surface, of two pole 4-groups : in the first (broken lines) each piece has the same strength, and in the second (solid lines), 2 pieces have +2% strength and two have -3% strength, ordered high-low-high-low.

follow Halbach's criteria for the easy axis rotation,[4] where the easy axis is taken to be magnetization axis. For a multipole comprised of M pieces that are geometrically identical, consisting of a permanent magnet material uniformly magnetized in the transverse plane, the easy axis advances an angle of $\frac{2N\pi}{M}$ on the coordinate fixed on the piece relative to the previous piece if 2N is the number of poles and M the number of segments in the transverse plane. This is illustrated for the case of a quadrupole of 8 trapezoidal pieces (N=2, M=8) in Fig. 6.

As illustrated in Fig. 6, we choose the m=1 piece to be bisected by the X axis. PERMMAG calculates the field at point (X,Y,Z) by summing up the contribution from each piece. For detail see " An Analytical Calculation of Multipole Field Produced by Oriented Permanent Magnets " by Z.Q. Xie and T. Antaya.[2]

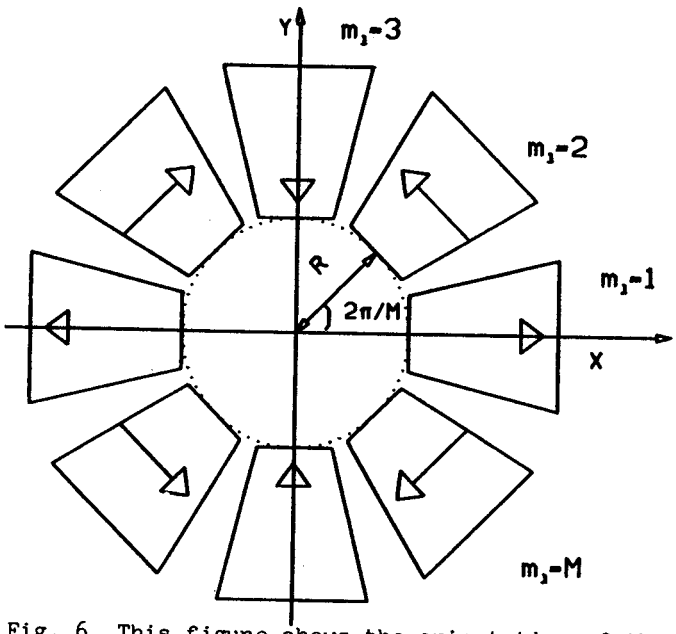

Fig. 6 This figure shows the orientation of the magnetization direction for an eight piece quadrupole (N=2, M=8). See text for details.

We would like to illustrate possible calculations with PERMMAG and make comparisons with existing 2D magnet codes. In Fig. 7, the 2D calculation codes HALBACH and PANDIRA are compared with the 3D code PERMMAG for a long hexapole magnet (length C=30".) made of rectangular pieces. All three codes give the same value at the hexapole midplane (Z=0".) and near the end of the hexapole magnet (Z=14.5") PERMMAG shows the finite multipole length effect. In Fig. 8, HALBACH, PANDIRA and PERMMAG are compared at the midplane (Z=0".) of a hexapole magnet composed of trapezoidal pieces, for different multipole lengths, again the PERMMAG shows the length effect. Fig. 9 shows in detail all the components of a hexapole magnet with rectangular pieces: B_r(vs r and Φ at Z=0".), B_Φ(vs r and Φ at Z=0".), B_z(vs r and Z at Φ=0.), B_t(vs r and Φ at Z=0".) and B_t(vs r and Z at Φ=0.). This is the standard output of PERMMAG and is very useful for the study of the field shape in fine detail at any point.

The PERMMAG has been generalized to do the calculations of all 2N multipoles that are made of geometrically symmetric trapezoidal or

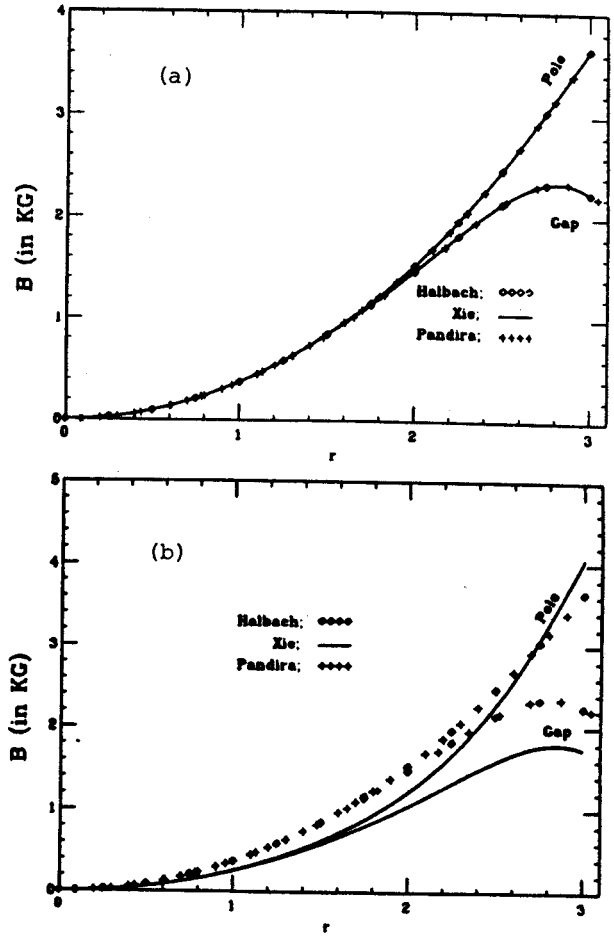

Fig. 7 Comparison of HALBACH, PANDIRA and PERMMAG for a 6 rectangular piece hexapole having pole dimensions 2"x2"x30" and B_{rm}=8.7 kG. The hexapole aperture is R=3". (a) pole and gap strength at midplane (Z=0."). (b) pole and gap strength near the hexapole end (Z=14.5").

rectangular pieces. As mentioned previously, the code also accurately does the case of a single permanent magnet. In addition, several straightforward modifications of the code are possible, such as rectangular and irregular shape multipole aperture rather than round aperture assumed for ECR magnets, calculations of combinations of trapezoidal and rectangular pieces would also be possible with a more generalized superposition formula. In addition one could take the derivatives of the field equations with respect to the field coordinates and input them to the code, then PERMMAG could also calculate the field gradient. These generalizations would allow PERMMAG applications for a wider range of permanent magnet geometries.

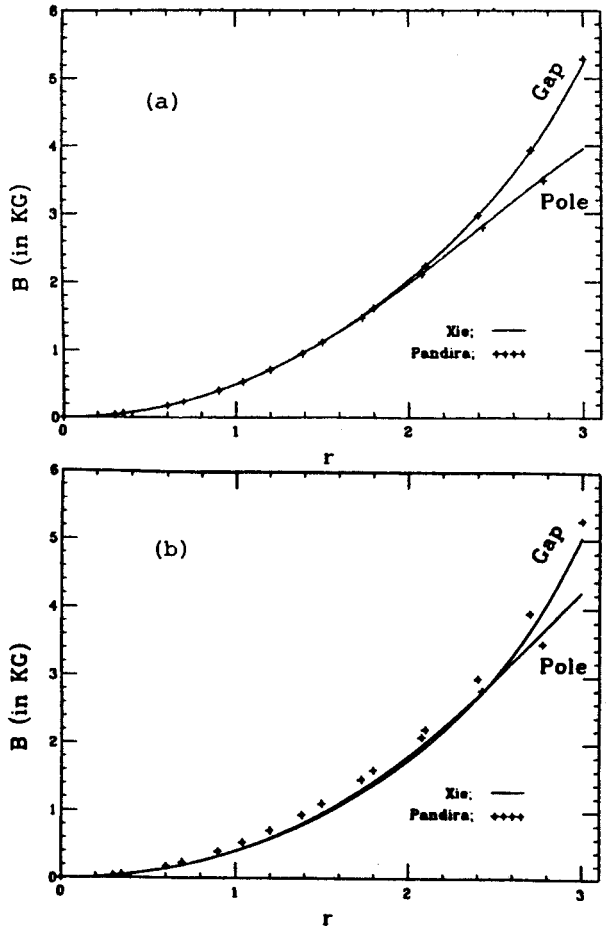

Fig. 8 Comparison of HALBACH, PANDIRA and PERMMAG for 6 piece trapezoidal hexapoles with piece dimensions A=3", B=3", D=5", and varying pole lengths, with B_{rm}=8.7 kG. The hexapole aperture is R=3". (a) pole and gap strength at midplane (Z=0."), multipole length C=50". (b) pole and gap strength at midplane (Z=0."), multipole length C=3".

References

1. Kai-hua Zhao and Xi-mou Chen, Electrostatics and Magnetostatics. (People's Education Publisher, P.R.C, 1978) Vol 2, p 99
2. Z.Q. Xie and T. Antaya, An Analytic Calculation of Multipole Field Produced by Oriented Permanent Magnets. To be published.
3. Richard J. Thome and John M. Tarrh, MHD and Fusion Magnet. (J. Wiley & Sons Inc, London, 1982) p 139.
4. K. Halbach, Nucl Instr and Meth. 169(1980) 5.

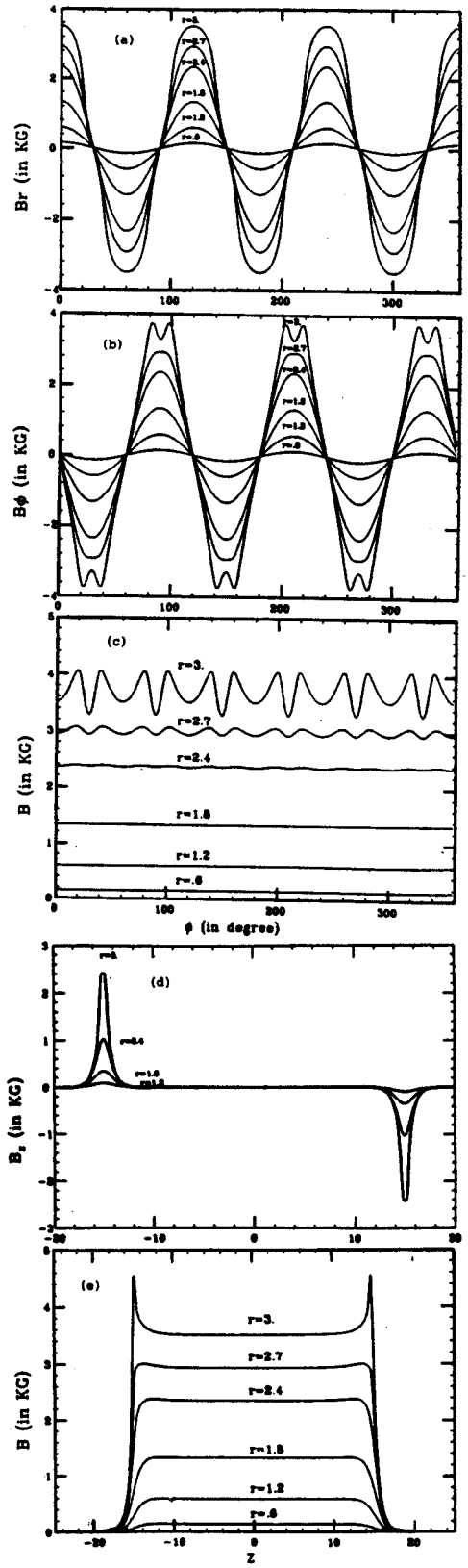

Fig. 9 Field components of a 6 piece rectangular hexapole magnet with dimensions 2"x2.5"x30" and B_{rm}=8.7 kG. The hexapole aperture is R=3". (a) radial component at midplane. (b) azimuthal component at midplane. (c) total strength at midplane. (d) B_z component vs Z at Φ=0. (e) total strength vs Z at Φ=0.

PRESENT OPERATION OF THE RT-ECR ION SOURCE

T.A. Antaya, D.P. Sanderson, W.D. Nurnberger and Z.Q. Xie

Positive ions from $^{2}H^{+}$ to Kr^{19+} have been injected into the K500 cyclotron during the first year of coupling to the RT-ECR. Nearly continuous operation of the ion source occurred during this period. The source configuration for most of this period has included a large first stage chamber and radial microwave injection into the main stage at the midplain. This development was the subject of the initial operation of the source during this period and will be discussed in this report. The shift to a larger first stage chamber resulted in large gains in highest charge states of light ions up to neon. Next development centered on the production of metallic ions by feeding solid materials into the main stage plasma. Metal ion development is considered separately in a report by D.P. Sanderson. Late in 1986 new power supplies were installed (to replace those borrowed from the K800 Cyclotron project) to power the source coils and the K500 injection beam line. At the same time the control system was re-configured to include the CP-ECR, SC-ECR and K800 injection beam line control elements. These developments are noted in a separate contribution by W.D. Nurnberger.

Present Source Configuration

Fig. 1 shows the present operating Configuration. A 10 cm diameter X 15 cm long first stage chamber with off axis axial microwave feed replaces the initial smaller (5 cm dia. X 10 cm) chamber and the main stage microwave feed has been moved to a radial port at the main stage midplane (there not being adequate clearance for the off-axis axial mainstage microwave feed as was the case in the earlier configuration). Two considerations motivated this change. First, the ECR resonance surface was close to the walls in the small first stage, making magnetic field adjustment during tuning a critical operation. Second, the diameter of the small chamber was close to the cavity low frequency cutoff for 6.4 GHz microwaves, making the microwave coupling critical. The change to the larger chamber simplified the first stage tuning, which has since gone in the direction of very strong coupling between the two stages, and has resulted in large increases in high charge state light ion intensities. A summary of ion production for gaseous feed to the RT-ECR is summarized in Table I.

The characteristics of the strongly coupled two stage mode are illustrated in Fig. 2. A large increase in the output of the first stage results in a significant jump in the high charge states during two stage operation. (The first stage output can determined by turning the main stage off, since each stage has an independent microwave feed.) In this mode the first stage is the "coarse" knob for high charge state ion production - all other knob are "fine".

Future Developments

The production of beams for acceleration in the K500 cyclotron dominated the use of this ion source - only source studies that could be fit into 2-3 day periods could be attempted. Even these were of reduced value due to differences in source conditions after extended operating periods. This situation is expected to improve with the operation of the CP-ECR - it will be possible in 1987 to focus again on the development of the RT-ECR while the CP-ECR is sending beams to the K500 cyclotron. This development period will nevertheless be somewhat short lived, as the initial operation of the

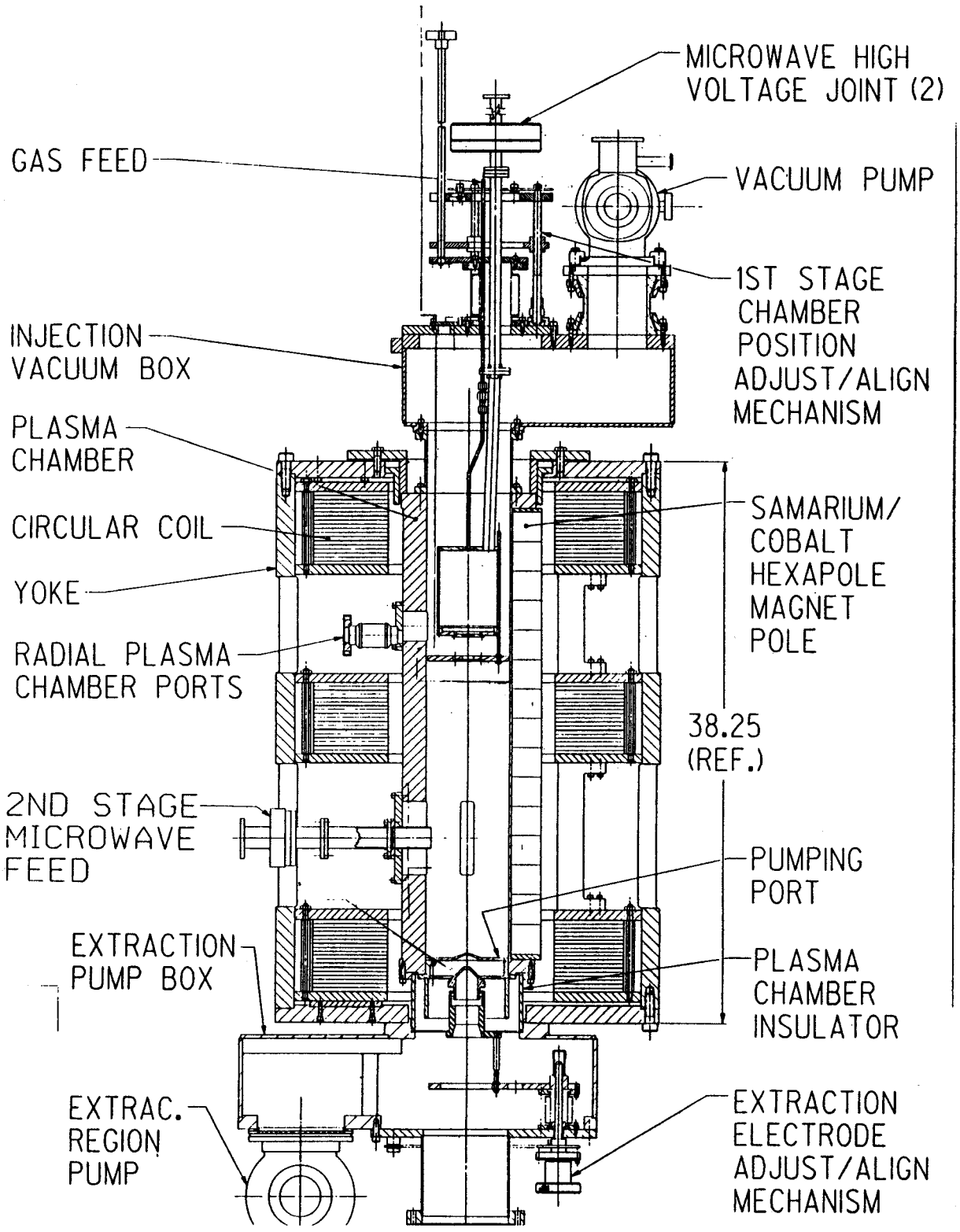

Fig. 1. The present operating configuration of the RT-ECR is shown.

Table I. DC ECR Performance for gaseous feed materials.

	^{12}C	^{14}N	^{16}O	^{20}Ne	^{40}Ar	^{86}Kr	^{127}I†
4	25.5	>100	87.	67.	19.		
5	5.6	68.	61.	50.5	*		
6	*	25.5	52.	41.1	42.		
7		*	12.2	16.5	55.		
8			*	5.0	94.		
9				1.0	44.		
10				*	*	23.	
11					7.0	*	
12					1.6	23.3	
13					0.10†	29.0	1.7
14					0.10†	29.0	2.3
15						23.2	3.0
16						*	*
17						6.8	2.7
18						3.2	*
19						1.4†	2.5
20						0.4†	2.3
21							2.1
22							1.8
23							1.0
24							*
25							.035††

Conditions: 10 kV ext. voltage; 8 mm ext. aperature,
† Vertical emittance decreased by 2.0 to increase resolution.
†† Vertical emittance decreased by 6.0 to increase resolution.
* Mixed M/Q

K800 cyclotron with beam injection from the CP-ECR source is likely.

One initial study will be to make the source operate with only one transmitter- since the combined power requirements of both stages are typically less than one third of the output power of a single transmitter (3.3 kW). A power divider circuit with computer control is now being readied for this purpose. The main gain from this operation will occur from releasing one of the two transmitters involved in the RT-ECR operation, for the development of other ion sources. We will in addition make a longer study to develop very high charge state calcium beams for use by the accelerators. Finally, a detailed study of the extracted beam formation process will be made.

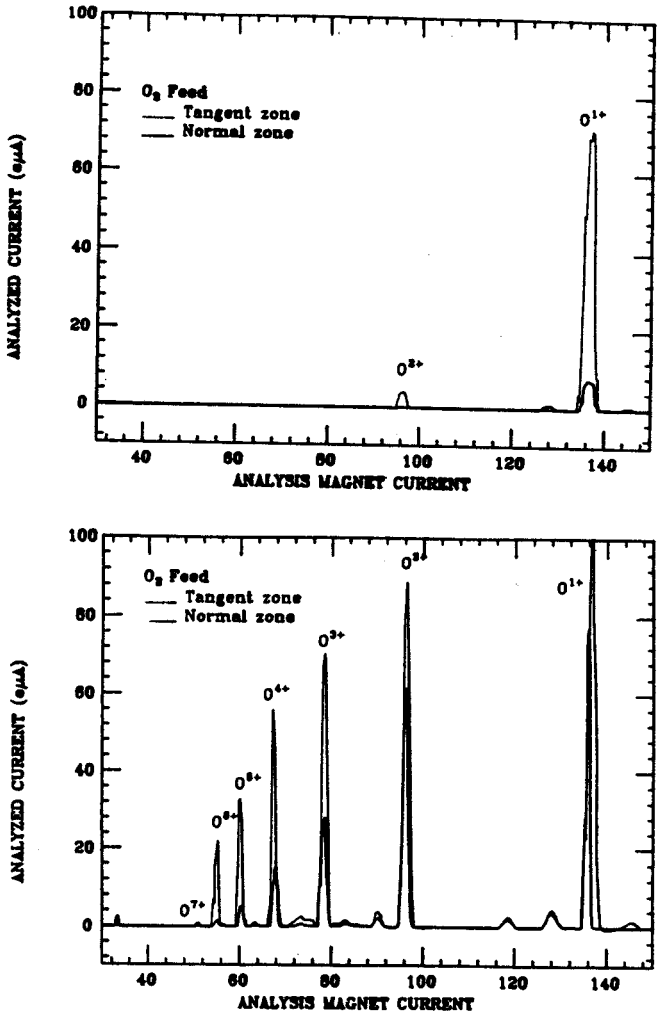

Fig. 2. For a 7 times increase in the first stage output of the RT-ECR, a progressively higher percentage increase in the output of high charge state oxygen ions is observed. In part (a), the source is adjusted for two different 1^+ output levels from the first stage. The effect of changing the first stage output is seen in a comparison of the two traces in part (b).

THE COMPACT ECR ION SOURCE CP-ECR FOR LIGHT IONS AND LITHIUM

T.A. Antaya, Z.Q. Xie and D.P. Sanderson

We are now about to start the operation of a second, compact room temperature ECR ion source. The final assembly of the CP-ECR ion source is now just finishing. The period of time from start of design to first operation will be approximately 4.5 months. This source has 35% of the confined plasma volume of the RT-ECR main stage and has an aspect ratio (length/diameter) of 2.35. The mode of operation will be based on a single stage mode of operation of the RT-ECR, identified during the early operation of that source (but later supplanted by the strongly coupled 2 stage mode)[1]. In this single stage mode good axial confinement and a single microwave feed combined to produce useable (≈ 1 eμA) intensities of intermediate charge state heavy ions and high charge state light ions in the RT-ECR source. The performance of the compact source will be similar. In addition, in the simpler "single stage" design of the CP-ECR, it has been easier to design a high temperature metal vapor oven into the source-- in the place where the first stage would normally reside. Such an oven will be used to produce lithium vapor as well as other metals for direct injection into the main stage of this source. (The oven details will be discussed in a report by D.P. Sanderson.) Here some characteristics of the compact source will be presented.

The source is shown in Fig. 1 for gaseous operation. The plasma axis orientation is vertical, as in the RT-ECR. The iron yoke is the major mechanical structure, providing support and alignment for all hardware. The coil pancakes are individually stacked inside the yoke with no additional alignment structures. The main chamber is pumped through slots in the extraction electrode (the pump is not shown). A limited first stage is possible using the resonance occurring in the rising field of the top mirror - microwave coupling to this zone initially will be thru leakage from the main stage proper, but later we may add a direct first stage feed.

It is expected that the charge state distribution for gaseous feed operation will be equivalent to the single stage mode of operation of the RT-ECR. In that mode, the magnetic field in the first stage was raised above the 6.4 GHz resonance level, so that ECRH was only possible in the main stage. In that mode the source produced 5 eμA of O^{7+}. We do not expect that the CP-ECR source will provide highly ionized species since we know that a strong first stage is necessary to decouple the main stage plasma from the neutral gas feed, as in the present operation of the RT-ECR, and that this is very important for the highest charge states. Instead, intermediate charge states will be present in sufficient intensities to produce useable beams for injection into the K500 cyclotron, and the use of the CP-ECR to generate these ions will free the large RT-ECR for further development of heavy ion beams. In addition, frequently used deuterium and helium calibration beams should also be easily produced by the CP-ECR. These uses constitute approximately half the motivation for this simple ion source. The other half is the possibility of developing metallic ion beams, with the initial emphasis on Lithium, and the design goals for Lithium are 10 eμA of Li^{2+} and 1 eμA of Li^{3+} The source should be operating before this report goes to the printer.

References

1. T.A. Antaya and Z.Q. Xie, 7th Int. Workshop on ECR Ion Sources, Julich, FRG, 72 (1986).

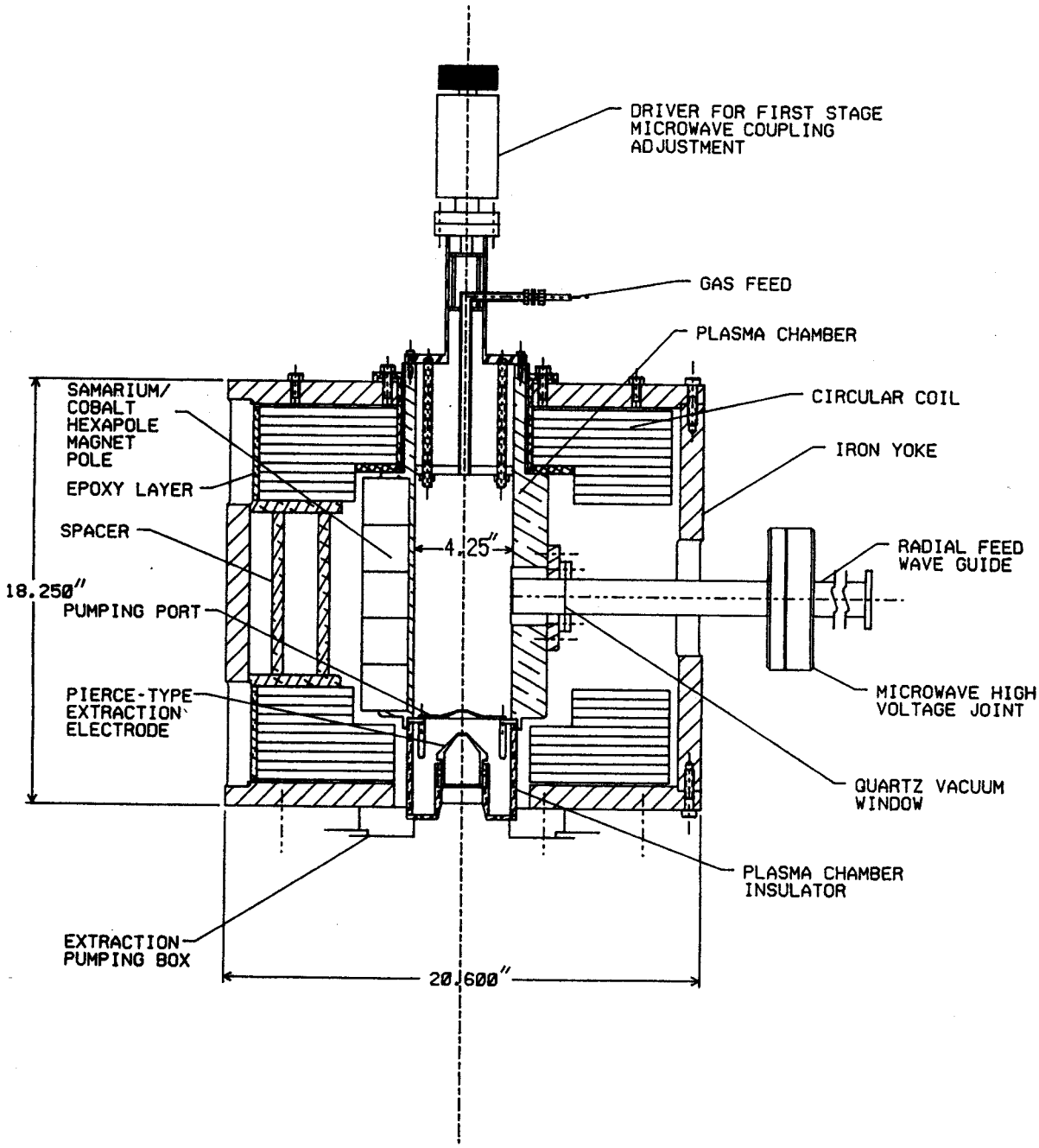

Fig. 1. The compact ECR ion source (CP-ECR) configured for gaseous feed operation.

THE HIGH FREQUENCY SUPERCONDUCTING ECR ION SOURCE PROJECT

T.A. Antaya, H.G. Blosser, J.A Nolen and A.F. Zeller

This report describes an ECR ion source with a superconducting magnet of wide dynamic range, to explore new ranges of significant operating parameters, leading to the development of beams of very highly charged ions, up to Q=40-50 for heavy masses. Present ECR technology can reach useable intensities at Q=20-25.[1,2,3] This work is the result of optimization of existing source designs. However, development has been slowed because the present sources have limited flexibility and are in full use providing beams for accelerators with demanding nuclear physics experimental programs. To make significant new gains requires a powerful new magnet that can span the existing operating space and then extend it to new regimes of ion confinement and ECR heating without making large changes in hardware.

Recent work in Grenoble with 16.6 and 18 GHz ECR sources has resulted in significant gains in intensity for high charge states.[4,5] This is primarily due to an increase in the maximum allowed plasma density. The sources were pulsed to avoid difficulties with microwave transmission and plasma coupling. There is a need to corroborate these results, to extend them to the continuous output regime, and to push them to higher frequencies.

The investigation of these effects requires an ECR magnet producing large magnetic fields and a tunable hexapole coil. At lower frequencies, such a high field magnet would also permit operation of the ion source on harmonics of the fundamental electron frequency, which may raise the intensities of highly charged ions through better microwave coupling.[6] Study of this possibility requires an ECR magnet that can produce a field at least twice as high as that required for excitation of the fundamental coupling mode. To match the requirements of these studies, a single ion source with a wide dynamic range of magnet excitation would be the best solution. We find that only a superconducting system can reasonably meet these requirements.

Fig. 1 shows the SC-ECR ion source design. This design follows the general features of the RT-ECR source. The plasma axis is vertical to simplify the mechanical design. The magnet includes a complete iron return yoke. This improves the magnetic efficiency of the coils, reduces the effects of stray magnetic fields on the plasma, and suppresses the plasma generated X-ray flux. As in the RT-ECR, both stages have minimum B magnetic fields. With 6.4 GHz in both stages, this source would be nearly identical to the RT-ECR. The main difference is that the radial magnetic field in this case is provided by an independently tunable superconducting hexapole coil instead of the permanent magnet hexapole in the RT-ECR. The design is also consistent with the experience gained in the Laboratory in the development of superconducting magnetic systems of similar design.[7,8] The coils will be composed of random-wound, epoxy-impregnated, NbTi wires. Quench characteristics and coil forces have been studied and indicate that this is a sufficiently rugged coil design.

This source design goes beyond the RT-ECR because the magnetic field can be raised smoothly to the field levels required for source operation at a resonance frequency as high as 35 GHz. The magnetic field profile of the main stage and extraction region, shaded in Fig. 1, is shown in Fig. 2. At 35 GHz, the ECR resonance occurs at 12.5 kG. The position of this resonance in the main stage can be seen in Fig. 2. One sees also that the minimum wall strength at the main stage midplane is 16.5 kG. High power microwave generators in the range of

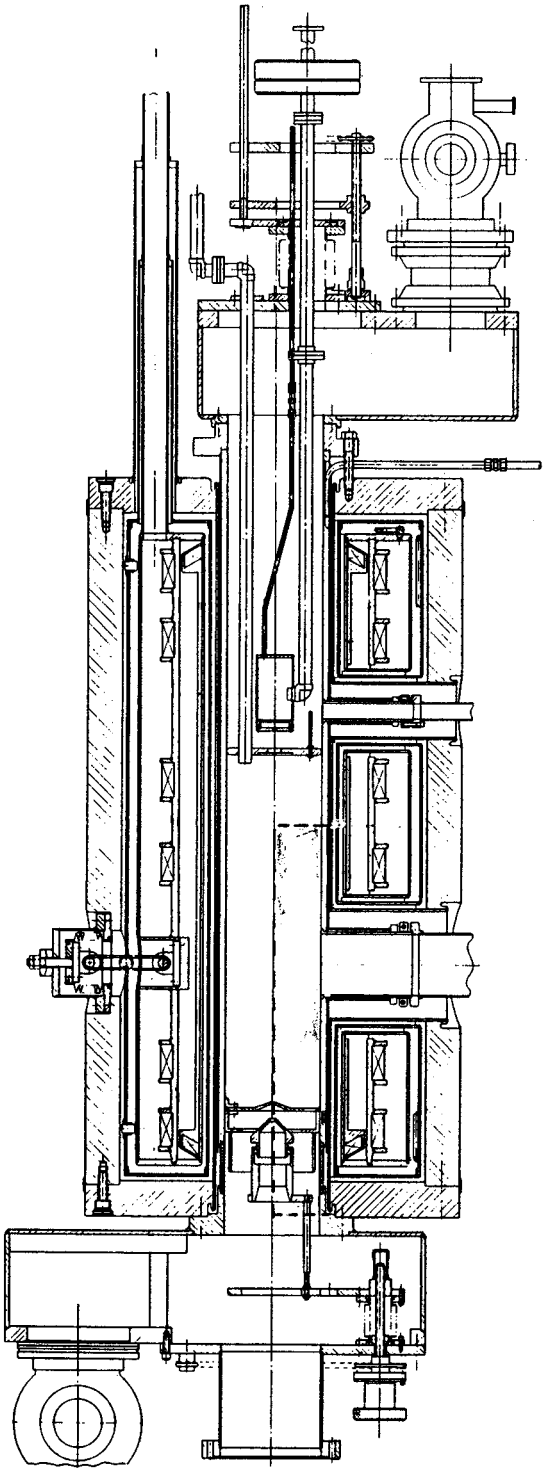

Fig.1. The SC-ECR ion source is shown.

5 to 18 gigahertz are klystron based; beyond 18 GHz, high power generator frequencies are few, with the next available frequency being a 28-35 GHz gyrotron amplifier. To span this range with conventional magnet technology would require a set of coil and permanent magnet

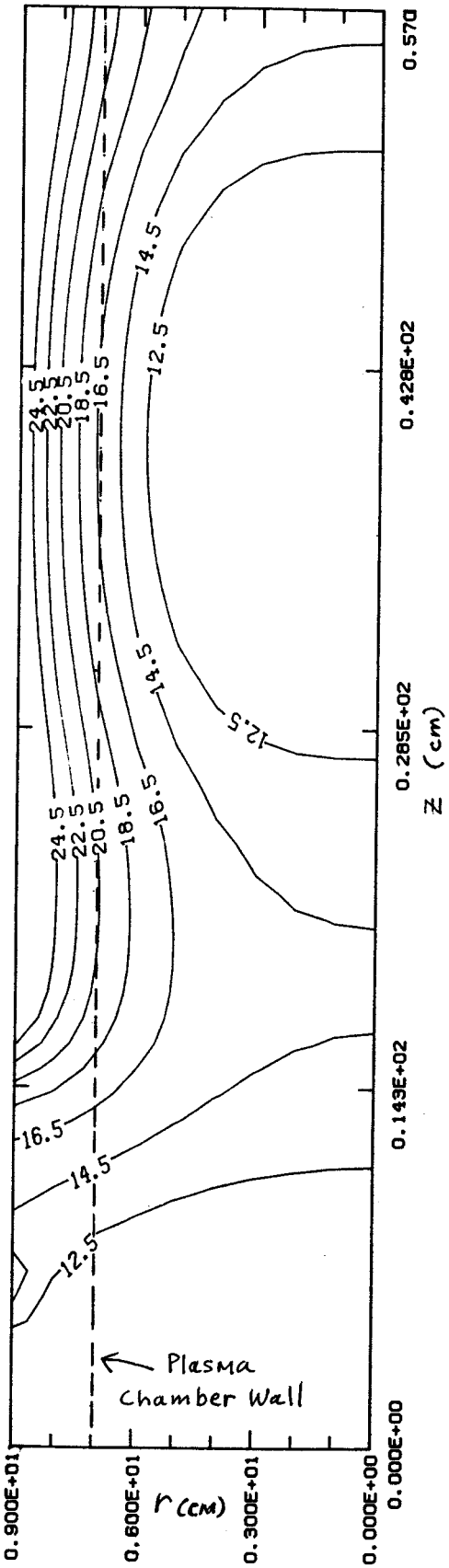

Fig. 2. The magnetic field isocontours for the region shaded in Fig. 1 are shown for the case of hexapole and solenoid coil excitations for 35 GHz operation of the SC-ECR.

hexapoles with prohibitive power consumption and permanent magnet material costs. The use of a single superconducting magnet system capable of covering the whole range then becomes an essential tool for frequency scaling studies. Further, independent adjustment of the mirror and hexapole strengths over a wide range at a given frequency will allow a more complete study of axial and radial confinement issues than has been possible previously.

We have just received funding to build the superconducting magnet for this source and assemble a configuration that will operate at 6.4 GHz (there exists spare microwave power since we have three 6.4 GHz transmitters). Since at 6.4 GHz it would be nearly identical to the RT-ECR, we would avoid the initial start-up R&D effort. Most of the hardware required to make the magnet an ion source is identical to the RT-ECR-- this greatly reduces the cost. The important studies of higher harmonic heating and radial confinement scaling would then be immediately possible with this ion source. At the same time the magnet will be tested at field levels required for operation at higher frequencies, up to 35 GHz. Should higher frequency transmitters become available, it will be possible to push the operating frequency higher.

References

1. T.A. Antaya, and Z.Q. Xie, 7th Int. Workshop on ECR Ion Sources, Julich, FRG, 72 (1986).
2. C.M. Lyneis, 7th Int. Workshop on ECR Ion Sources, Julich, FRG, 1 (1986).
3. A. Chevalier and Y. Jongen, 7th Int. Workshop on ECR Ion Sources, Julich, FRG, 266 (1986).
4. F. Bourg, et. al., 6th Int. Workshop on ECR Ion Sources, Berkeley, CA, 1 (1985).
5. R. Geller, et. al., 7th Int. Workshop on ECR Ion Sources, Julich, FRG, 187 (1986).
6. R. Geller and B. Jacquot, 7th Int. Workshop on ECR Ion Sources, Julich, FRG, 31 (1986).
7. J.C. DeKamp, et. al., IEEE Trans. Mag. 21, 990 (1986).
8. A.F. Zeller, et. al., Proc. 9th Int. Conf. Magnet Tech., Zurich, Switzerland, 167 (1985).

METAL ION PRODUCTION IN THE ECR ION SOURCES AT NSCL

D.P. Sanderson, T.A. Antaya, and Z.Q. Xie

As part of the continuing development of ion beams in the ECR ion sources for injection into the cyclotrons at NSCL, metallic ion production poses interesting challenges. An ECR ion source plasma is generated by the ionization of gases--the material feed is easily controlled and any unused material is pumped away by the vacuum system. Metals, however must be carefully introduced into a plasma produced by a gas. Unused feed material is deposited on water cooled surfaces in the plasma chamber and can have a large effect on subsequent beams. In addition, the plasma heats and vaporizes any uncooled material in direct contact with the plasma at an unpredictable rate.

Four other laboratories have invested much effort in metal ion production in ECR sources. A major effort to produce beams of solid materials has occurred at CEN in Grenoble. In one development there, a small moveable piston is used to insert solid materials including calcium into the main stage of Minimafios.[1] The ECR source at ORNL has produced several metalic beams using a foil positioning system that allows tangential contact between the material and the plasma.[2] After only limited success of direct solid feed of lithium into an ECR, workers at Karlsruhe constructed a source specifically for lithium ion production (LISKA) using a metal vapor oven.[3] Another major effort in this field has taken place at the Lawrence Berkeley Laboratory. Principally, metal ions are generated using a heated oven which injects vapor radially into the plasma of the LBL source, although direct solid feed has also been attempted there.[4] By these techniques, ions of approximately 27 gaseous and solid elements have been successfully produced in ECR sources to date.

Inspired by these successes and the demand by experimenters for beams from solid materials, a program of solid material beams was started during 1986 by the ECR group at NSCL. The initial program can be divided into beams produced by the feeding of solid materials into the room temperature source (RT-ECR) and beams to be produced using a metal vapor oven in the compact source (CP-ECR).

RT-ECR

High charge state beams of solids are produced in the RT-ECR by inserting a sample of the material directly into the second stage ECR zone through a radial port at the second stage midplane. (See figure 1) The feed mechanism consists of a linear motion feedthru with 15.25 cm of travel attached to an airlock. A gate valve seals off the source from the feedthru when changing samples. The source remains under vacuum during the transfer. The small ball valve is used to pump out the sample volume prior to opening the gate valve. By pumping out this volume, the source vacuum is not affected by the transfer. Since the whole drive mechanism is at the source bias voltage, the operator uses an insulated handle to turn the feedthru shaft.

Many different beams have been produced using this system. They are summarized in the charge state distribution table below. (Table 1)

The criteria for an appropriate sample for this system were found to be a high melting point (>700°C.) and a lack of dissolved gases in the sample. The first criterion comes from the empirical observation that it was difficult to control the rate of heating in the plasma, since it appears that the transition region from no heating to excessive heating is very sharp (a few mm). Low melting point materials tend to vaporize too quickly under these conditions. An

Fig. 1 The RT-ECR solid feed mechanism.

Table 1. Charge state distributions in eμa for beams from the RT-ECR using the solid feed.

	$^{6,7}Li$	^{19}F	^{28}Si	^{51}V	^{90}Zr	^{184}Ta
1+	8.5	37	*			
2+	1.3	15	*	6.5		
3+		14	.33	7.4	7.5	
4+		10	*	8.7	6.5	
5+		5	1.2	11	2.5	.09
6+		2.5	*	12	1.5	*
7+		0.5	*	13	0.5	.10
8+			*	12		.10
9+			0.2	8.0		.20
10+				3.6		*
11+				1.6		.26
12+				0.63		1.0
13+						*
14+						.85
15+						*
16+						1.4
17+						1.6
18+						1.7
19+						1.5
20+						1.4
21+						1.0
22+						.68
23+						*
24+						.24
25+						*
26+						*
27+						.11

* more than one beam present.

feed:	LiF crystal	silicon crystal	foils	wire
support gas:	He	He	He	N_2

example of this effect was the case of lithium ion production, where a direct solid feed of the LiF material was only marginally controllable. The vaporization rate was high and the flourine contamination of the chamber excessive. It was later found that the flourine in the source significantly affected the subsequent high charge state nitrogen production. The source had to be disassembled and the chamber scrubbed to remove the deposits. The second criterion comes from the observation that the effect of having dissolved gases in a feed sample during operation is to cause the local pressure in the source to rise, inhibiting high charge state production through negative gas mixing and charge exchange. Tuning during the expulsion of the dissolved gases from the sample is very complex.

The procedure for tuning a solid feed beam is to first produce a stable beam with the support gas. Then the solid is inserted until it reaches the outer edge of the plasma. This is usually seen as either a rise or fall in the x-ray production. Electrons with over 100 keV energies striking a heavy metal will produce a large amount of radiation. If however, gas is produced by the heating, the rise in the local pressure will lower the energy of the electrons and reduce the x-ray output. Once the sample is being heated, the drive is adjusted to maintain a good output with the minimum necessary feed rate.

Tantalum was the first metallic beam produced in this source. It met both criteria with both a high melting point and high purity. Later vanadium and zirconium were tried. These were found to require helium as the plasma support gas since the vaporized metals which struck the inner walls of the plasma chamber formed a gettering surface, and thus pumped the more reactive gases such as nitrogen or oxygen. These heavier mass gases would have been expected to improve the high charge states, on the basis of the experience of gas mixing in

this source, but because of the gettering effect could not be used. If, while tuning beams of vanadium or zirconium with a nitrogen feed the plasma was lost, it took large amounts of gas to overcome this pumping and restart the plasma. Good results were also obtained using a pure silicon crystal removed from an old radiation detector to produce ions. This method has advantages over the gaseous alternative to silicon crystals, silane gas, a highly corrosive and explosive compound. For several K500 experimental runs, lithium 1+ and 2+ beams were produced using a purified lithium flouride crystal as the feed. Both ^{6}Li and ^{7}Li beams with acceptable long term 2^{+} beam currents (1eμa) were produced. By using large amounts of material, 1^{+} beams of order 10 eμa or greater, were generated though the performance declined with extended use. This method has the previously mentioned drawback in that the flourine contaminated the source and appeared in the spectra during later runs. Since flourine is heavier than oxygen or nitrogen, it had a detrimental effect on the high charge state production of these elements as well as the lithium beams. Only when the source was opened and the deposit removed was the contamination problem solved. There will be more lithium beam requests at NSCL, therefore a cleaner method for lithium production was needed. Some trials were made with the insertion of pure lithium metal directly into the plasma. Acceptable quantities of all of the charge states were obtained, but only for a short time intervals, due to high vaporization rates. In contrast to the LiF runs, metallic lithium did not contaminate the source and no peaks appeared in subsequent runs.

The LiF crystals were the lowest melting point materials tried with direct solid feed. The tuning was very complex when compared with tantalum, the highest melting point material attempted. It appears that as the solid melting point decreases, so does the tuning range. At 800°C it is already easier to vaporize lithium flouride at low microwave power without getting sufficient high temperature electrons for good lithium 2+ and 3+ production. The key for ion production from low melting point materials would be to have an independent knob controlling vapor pressure without affecting the ionization rate determining electron temperature. A fundamental difficulty with the insertion of solids directly into the plasma is that the hot electrons in the plasma drive both the material vaporization process and the high charge state ionization rates. Raising the electron temperature to make high charge states in turn will actually suppress them if a large rise in the vaporization rate also occurs. For refractory metals it is found that sufficient tuning range exists, since the high electron temperatures needed to melt the sample also aid high charge state production. These observations suggested that a metal vapor oven would be the best way to introduce lithium metal and other low melting point solids into the plasma. The CP-ECR ion source is well equiped for this task.

CP-ECR

The compact ECR ion source (CP-ECR), described elsewhere in this annual report, is designed to use a large metal vapor oven for injection of low melting point, high vapor pressure materials into the ECR plasma. The metal vapors are injected axially into the single minimum B stage from a stainless steel oven. A heated liner should recirculate into the plasma any material which deposits on the walls. The source is easily disassembled and cleaned.

The oven is based on a design used in polarized lithium ion sources at the tandem accelerator laboratories in Heidelberg[5] and at Florida State Univ.[6] (See Figure 2) A sealed stainless steel container with an output laval nozzle is loaded with the source material and

inserted into a heater assembly. The nozzle is used to restrict the output and confine the vapor beam close to the source axis. The heating is done by coaxial wire heater cable. The temperature is monitored and regulated using commercial proportional temperature controllers and thermocouples. The heating current is provided by a set of variacs and the whole control assembly is mounted at the source high voltage in an isolated instrument rack.(See Figure 3) The oven is thermally insulated with graphite felt and an outer layer of stainless steel foil. The system has been tested to 730° C without heating the plasma chamber and should easily attain temperatures greater than 800° C.

The heated liner consists of a long stainless steel tube heated with the same cable from the inside. The tube has an outer diameter slightly smaller than the bore of the plasma chamber. A rectangular hole at the waveguide entrance permits the microwaves to reach the ECR zone. A boron nitride baffle with a small hole in its center separates the oven from the main stage. This causes a much higher pressure in the small gradient ECR zone at the top of the source. It is expected that the initial ionization of the vapor here will raise the high charge state output of the source.

The liner will be heated to approximately 400° C to reevaporate any material not used in the plasma. It may be possible to turn off the oven and generate the plasma off this liner recirculation.

A basic feature of this ion source is its ease of cleaning. If too much material accumulates in the extraction region or in the oven vessel, cleaning is accomplished by removing the source from its 90° magnet and flushing it out with water, a highly effective remover of alkali metals. A large percentage of the operation of the CP-ECR will be for lithium production, just as in LISKA at Karlsrhule.

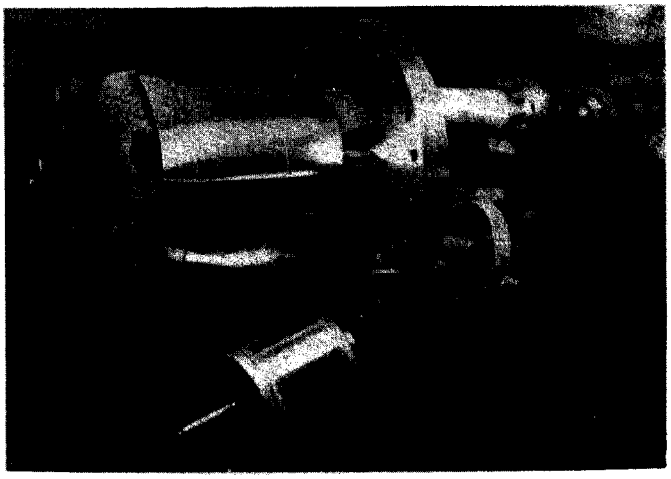

Fig. 2 The CP-ECR oven system. The heater assembly is inserted in the top of the upper vacuum chamber of the CP-ECR source.

Fig. 3 The controls for the CP-ECR oven system. The control box is at the same high voltage as the source.

Future Beams

A large number of beams can be produced from high melting point solids in the RT-ECR solid feed system. Beams produced in ECR sources at other laboratories which we have yet to try successfully include aluminum, niobium, and calcium. The success with solid silicon suggests germanium as a source material due to their similar chemical properties. This method would be improved through the use of an automatic feed drive. A remotely controlled motor drive system identical to that used on the gas valves will be installed in the next year. The temperature range of the CP-ECR oven allows it to be used for many elements in addition to lithium: Ca, Mg, Bi, K, Na, or Zn. All of these metals have a vapor pressure greater than 10 mtorr within the temperature range of the oven. For those elements with more than one isotope, the analysis system can easily resolve the individual beams. For the production of the highest charge states for these materials, a larger two stage source is necessary. Therefore a small oven similar to the LBL model has been constructed to inject radially into the RT-ECR. Its use will be restricted to limited runs where very high charge state beams are necessary.

Conclusions

Two systems for introducing solids into the ECR ion sources at NSCL have been described. The simplest system--insertion of a high melting point material into the plasma--has been shown to work very well with beam intensities and lifetimes suitable for cyclotron injection and multi-day experiments. The upcoming use of a metal vapor oven on the new CP-ECR ion source will allow the use of low melting point materials in an easily controlled manner with simple maintenance and cleanup.

With two operating sources at NSCL, there will be a greater possibility for the development of solid beams. Both systems add a much larger section of the periodic table to the list of beams available to NSCL cyclotron users.

References

1. R. Geller, B. Jacquot, and M. Pontonnier, Rev. Sci. Instr. 56,1505(1985).
2. F. W. Meyer and J. W. Hale, contribution to 1987 Particle Accelerator Conference (Washington, D. C.).
3. V. Bechtold, L. Friedrich, and F. Schulz, Tenth Intl. Conf. on Cyclotrons and their Appl. (East Lansing)1984.
4. C. Lyneis, contribution to 1987 Particle Accelerator Conference (Washington, D. C.).
5. E. Steffens, W. Dreves, H. Ebinghaus, M. Köhne, F. Fiedler, P. Egelhof, G. Engelhardt, D. Kassen, R. Schäfer, W. Weiss, and D. Fick, Nucl. Instrum. and Methods 143,409(1977).
6. D. P. Sanderson, dissertation, Florida State University, 1986.

BEAMLINE QUADRUPOLE PROGRESS REPORT

J.C. DeKamp, C.T. Magsig, J.A. Nolen, A.F. Zeller

During the last year, work on beamline quadrupole magnets has concentrated on procurement of long lead time items, developing coil winding techniques, and construction of two quadrupole doublets needed for the first K800 experimental setup.

Quadrupole doublet design was completed based on the prototype singlet built and tested earlier.[1,2,3] The liquid helium (LHe) and liquid nitrogen (LN2) containers were made longer to accept two magnet assemblies and the necessary extra cryogen volumes. The support system design was adjusted to account for the larger weight and size. The LHe feedline assemblies were redesigned to eliminate thermal accoustic oscillation tendencies found to exist in the prototype, while still maintaining reasonable heat leak values. The doublet has a 27% lower calculated heat load and is 30% less expensive to build than two singlets. Calculated doublet heat leak contributions are shown in Table I. The leads are cooled by the cold gas from the cryostat and hence do not contribute significantly to the numbers in Table I.

Table I

Calculated cryogen boiloff rates.

Item	LN2 (l/hr)	LHe (l/hr @ 1atm)
Feedlines	.037	.042
Vent pipe	.007	.038
Support links	.005	.020
Radiation	.180	.079
Totals	.229	.179

Work on coil production centered on modifications to the existing winding table. A new clutch and form motion take-up system was installed which reacts faster to changes in spool velocity, resulting in more constant wire tension. Fewer and larger idler pulleys are now used, giving less chance for wire breakage. A new epoxy bath system allows for cleaner operation and more uniform wire coating. A new end-form mold was constructed to make the end-forms more uniform. Also duplicate winding forms were made for quicker turnaround between winds.

Manufacturing of magnet steel assemblies was released to Japan Steel Works. All 60 steel assemblies have been received.

Superconducting wire specifications were changed slightly from that of the prototype magnet to have guaranteed critical currents of 22 A, instead of 19 A, at 2 Tesla. Manufacturing of the wire was released to Outokumpu Copper Products. A request was made by the vendor to supply the wire with polyesterimid insulation instead of formvar as was used in the prototype magnet. Coils were wound from sample spools and then tested at FNAL to be sure of proper bonding of the epoxy to the insulation. Test results for two quadrupole coils in their own self fields are shown in Fig. 1. As is shown, significant training did occur. The first quench initiated at about the same current as in the prototype coils, although less training was observed in the prototype coils. The new conductor did, however, reach higher critical currents. It is thought that the lower current capacity of the wire in the prototype coils limited the forces to levels below those needed to break epoxy-wire bonds or that epoxy-insulation bonding is significantly different, although no solution can yet be reached. This is to be investigated in the coming year. The testing did show the polyesterimid insulation to be acceptable. About 10% of the total order is now in house, with the remaining four million feet in shipment.

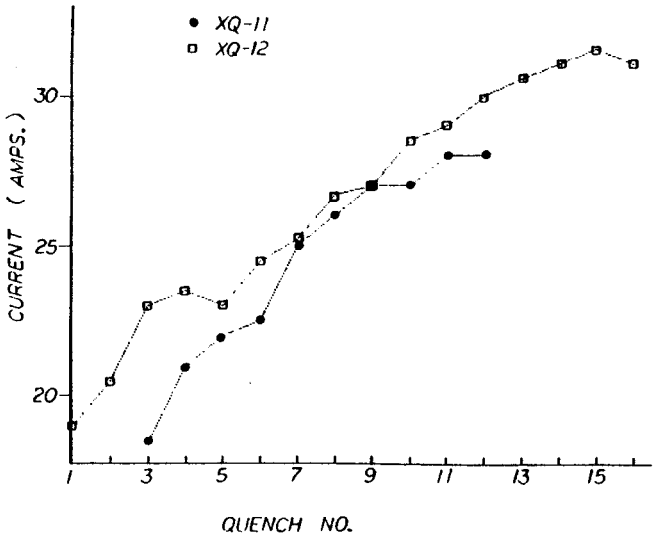

Fig. 1. Quench no's. 1 and 2 for coil XQ-11 are not shown as they were caused by eddy current heating of filaments within conductor from ramping too quickly.

Additional total order items received are the cryogenic valves, LHe level sensors, and current lead wire. A new leak detector system was purchased to support construction.

Cryostat parts for two doublets have been received and are awaiting assembly. Doublet coil winding has also begun. Both doublets will be finished in time to support initial K800 experimental operation.

We wish to acknowledge the assistance of A.D. McInturff of FNAL for conducting the wire testing.

References

1. A.F. Zeller et al, Proc. of the Tenth Int. Conf. on Cyclotrons and Their Applications, 1984, 79.
2. A.F. Zeller et al, Proc. Ninth Int. Conf. Magnet Technology, 160 (1985).
3. A.F. Zeller et al, MSU Annual Report, 1985, 176.

16 DEGREE DIPOLE CONSTRUCTION AND TESTING

J.C. DeKamp, C.T. Magsig, J.A. Nolen, A.F. Zeller

The prototype beamline dipole has been completed and successfully tested. It's design, construction, and preliminary test results have been published elsewhere.[1-7]

The maximum operating field of 1.75 T, as measured with a NMR probe, was reached at a current of 91 A. The magnet was ramped past this point to 1.8 T at 96 A without quenching. The effective length of 87 cm gives a maximum bend angle of 16.3° at 1.8 T. The pole tip gap had a transverse nonuniformity of 0.2% caused by the welding of the pole tips to the bobbin cryostat wall. The gap nonuniformity can be reduced in future dipoles by use of more spacers welded on each side of the gap. Magnetic mapping was done with the electronics used for the K800 cyclotron, and a special table constructed for beamline magnet measurements. Figure 1 shows field uniformities from mapping results vs. "POISSON" calculations adjusted by taking into account the measured gap nonuniformity between it's middle and outer radius at fields of 5.5 and 17.5 kG. The required uniformity of 0.1% within the beam volume is satisfied. Measurements showed that the field was not sensitive to small changes in coil bobbin positioning.

Persistent mode operation gave a field decay of .02% per hour. This corresponds to a resistance of 10^{-7} Ohms in the persistent circuit. This decay value is too large to make persistent mode operation of value for K800 beamline operation. The persistent switch was quenched twice without harm, showing the protection diodes worked well.

The horizontal support links at the large end, carrying the unbalanced magnetic forces, reached a maximum load of 300 lb. at full field, increasing from the 175 lb. initial pretension.

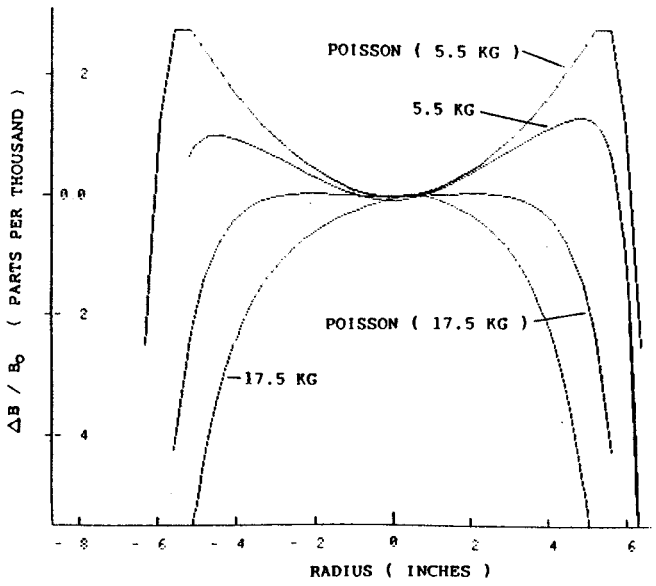

Fig. 1. Calculated field uniformities for 5.5 and 17.5 kG compared with measured maps for a position 9" inside the large end. "POISSON" calculation have been adjusted to take into account the measured nonuniformity of the gap between the middle and the outer radius. the required uniformity of 0.1% within the beam volume is satisfied, but the left-right asymmetry at high field is not presently known.

This was well within the 900 lb. design limit. No load change was noticed on the vertical support links as the field increased.

The best cryogenic boiloff rates measured were a factor of 2-3 greater than those calculated, giving a 2.5-3 day refill cycle instead of the 7 day goal. This is unwanted since it will control the liquid helium (LHe) refill cycle of a number of other magnets on the same cryogenic manifold which are capable of longer holding periods. Reasons for the high LN2 heat loads are thought to be in the bobbin cryostat as the insulation space is very tight. The high LHe heat load is thought to be due to inefficient shielding, especially in penetration areas, or a high resistance thermal short. Another possible heat load contribution may be due to the LHe container not being vented

directly to the lead port. The container therefore had to be vented through the cold gas return line to prevent over-pressure. It also had to operate at an equal or higher pressure to insure liquid was not pushed out below the level of the persistent switch. A pressure difference of only 120 Pa makes a relative difference of 10 cm in liquid level between the container and the lead port. As the pressure could not be controlled to even 1000 Pa, as setup, liquid was being pushed up the leads making them less efficient through increasing their area/length ratio. Magnet cooldown time was 3 days. This is slow for the amount of thermal mass because of no separate cold return line for the bobbin. The cooldown gas from the bobbin is limited to return through the leads and two way flow through the large feedline from the LHe container. This gave a bobbin cooling rate of 10 W, even though the upper container filled quickly. The new feedline design seemed to eliminate thermal acoustic occillations present in an earlier design in the prototype quadrupole.[8,9] Filling cryogen containers while the magnet was energized presented no problems. A LHe refill cycle duration of 1.25 hours was experienced for filling two quadrupole singlets and the dipole. This time period includes the 20 min. manifold cooldown time. The LN2 refill time was 20 min. for all three devices.

During 1987 the dipole will be partially disassembled for modifications to improve cryogen holding time, decrease cooldown time, and equalize LHe container and lead port pressures. In addition the persistent switch will be removed and a new set of current leads installed. The dipole will then be installed in the first K800 experimental set-up.

References

1. A.F. Zeller et al, MSU Annual Report 1981-1982, 101.
2. M.J. Dubois, A.F. Zeller, and J.A. Nolen, MSU Annual Report 1982-1983, 155.
3. A.F. Zeller et al, ibed, 151.
4. J.C. DeKamp et al, IEEE Trans. on Mag. Mag-21, 990 (1985).
5. J.C. DeKamp et al, MSU Annual Report 1983-1984, 266.
6. J.C. DeKamp et al, MSU Annual Report 1985, 179.
7. J.C. DeKamp et al, IEEE Trans. on Mag. Mag-23, (to be published, 1987).
8. A.F. Zeller et al, Proc. Ninth Int. Conf. Magnet Technology, 160 (1985)
9. J.C. DeKamp et al, MSU Annual Report 1985, 176.

BEAM OPTICS OF ADJUSTABLE PERMANENT-MAGNET QUADRUPOLE AND DIPOLE MAGNETS

S. Tanaka, J.A. Nolen, and A.F. Zeller

The permanent magnet exit channel design, presented elsewhere in this Annual Report, describes the use of high field dipoles and large gradient quadrupoles. In addition to having the desired quality of very small external fields[1], they are also adjustable over a large dynamic range[2].

Adjustable quadrupoles and dipoles can be constructed from rings of permanent magnet material. To adjust the strength, the rings are rotated about the beam axis in opposite directions. Normally, in addition to changing the effective dipole or quadrupole strength, this would also mix x and y phase spaces. However, special geometries can be used to avoid the mixing of the phase spaces while still permitting variable strengths.[2,3] Below we present results for geometries appropriate for dipoles and quadrupoles to be used in the K800 cyclotron exit channel. The treatments in ref 2 and 3 are in terms of first order matrix optics. Below we compare first order calculations with the program TRANSPORT with raytracing calculations from the program RAYTRACE in order to determine more accurately the degree to which the x and y phase spaces are decoupled by the methods of ref 2 and 3.

I. Permanent magnet quadrupoles

In designing a permanent magnet quadrupole, two factors are considered separately. One is lens configuration, and the other is the above mentioned capability of covering various beam momenta while maintaining non-mixture of horizontal and vertical motion. As the lens configuration, we have taken two quadrupole doublets which gives us simple optics where the beam transport matrix becomes a unit matrix. The capability of covering various beam momenta is achieved by four layers of quadrupole sections for each doublet, as shown in Fig. 1. Each layer or ring consists of twelve trapezoidal sections as reported elsewhere in this annual report and installed with the entire body rotatable around the z-axis. The gradient

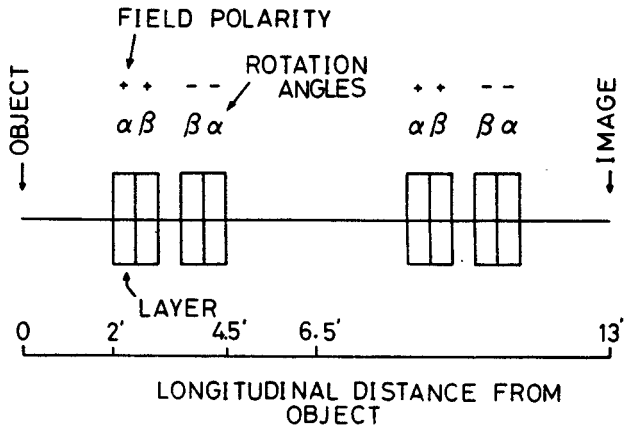

Fig. 1. Lens configuration for the permanent magnet quadrupole focusing system.

of the magnetic field of the quadrupole magnet was determined to be large enough for focusing a beam of 1.6 GeV/c with all the quadrupole rings oriented upright. The magnetic field at pole tip and half-aperture are 6.710 kG and 1.905 cm, respectively. For lower beam momenta we must rotate all the rings. Thus there exists a certain relation between the rotation angles and the beam momentum which was calculated by the programs TRANSPORT and RAYTRACE with the constraint that the vertical and horizontal motion are independent of each other. Table 1 lists the rotation angles, α and β versus beam momentum. The difference between TRANSPORT and RAYTRACE calculation is quite small and is concerning only the focus of the beam. As seen in Fig. 2, if a momentum is given, β is determined uniquely. However, for the two doublets there are two solutions for α, the normal solution α_1, and a spurious solution α_2. The difference between them can be explained in

Table 1. Relation between beam momentum and rotation angles, α and β. For the chosen values of β, α_1 and α_2 result from TRANSPORT calculations. (α_1 is the "normal" solution while α_2 is the "spurious" solution.)

p (MeV/c)	α_1 (deg.)	α_2 (deg.)	β (deg.)
1600.0	0.00	0.00	0.00
1554.00	4.97	155.03	-10.00
1426.28	9.48	130.52	-20.00
1244.90	13.01	106.99	-30.00
1049.40	15.02	84.98	-40.00
877.31	15.11	64.89	-50.00
749.66	13.22	46.78	-60.00
668.12	9.71	30.29	-70.00
624.52	5.12	14.88	-80.00

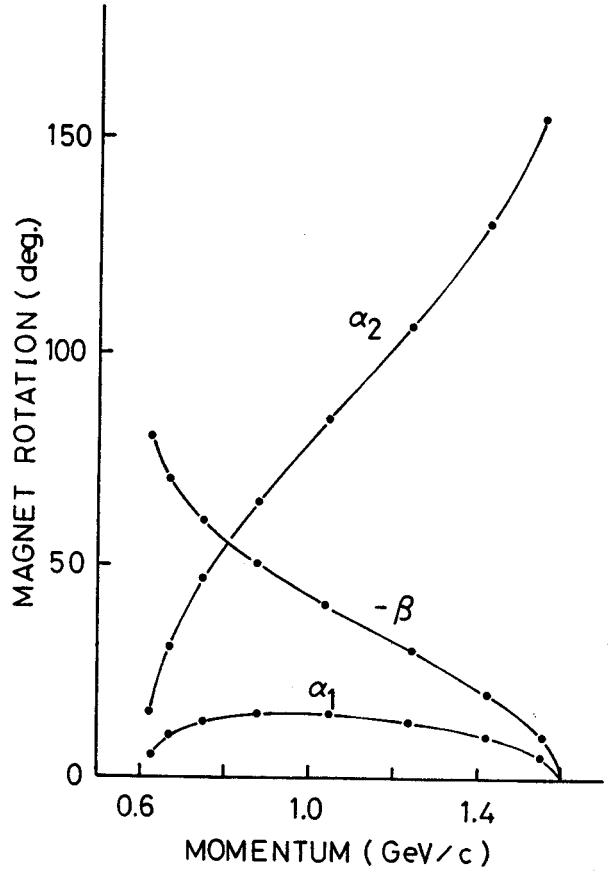

Fig. 2. Relation between beam momentum and rotation angles, α and β for the quadrupole. α, and α_2 denote two solutions for α. β takes negative values.

terms of the demixing mechanism of the horizontal and vertical motion through the sequential quadrupole magnets. Figure 3 shows "RAYTRACE" calculations of the beam trajectory with the initial condition for horizontal motion, namely x_0=0, θ_0=1 mrad, y_0=0 and Φ_0=0. The gain in vertical divergence starts to grow at the entrance of the first quadrupole magnet. This becomes zero at the exit of the fourth magnet, if α_1 is chosen for α. On the other hand, if α_2 is chosen, the vertical divergence becomes zero at the exit of the eighth magnet, i.e. the x and y phase spaces are not decoupled in the region between the two doublets. This result also shows the reason why we have required four layers of permanent quadrupole magnets for each doublet. It is worth emphasizing that the first four layers of the permanent quadrupole magnet behave nearly perfectly, as a quadrupole doublet if the set of solution α_1 and β is taken. This permanent quadrupole quadruplet can be tuned to focus beams with momenta from 0.6 to 1.6 GeV/c.

With the program RAYTRACE we have determined the degree to which the x and y phase species are decoupled between the two doublets. The TRANSPORT program predicts the values of α_1 and β to use for a specified momentum p to have decoupling in the first order transfer matrix. Starting from these solutions and an optical layout as shown in Fig. 3. we used the program RAYTRACE to follow the ray x_0=0, θ_0=0 mrad, y_0=0, Φ_0=15 mrad through the system. Halfway through the system, between the two doublets this ray is predicted to have x=0.000 cm, θ=0.000 mrad, and y=1.866 cm, Φ=-12.718 mrad, i.e. perfect decoupling of x and y phase spaces for rays with these divergences.

II. Permanent magnet dipole

Because of the nonlinear saturation of the return yoke, the deflection of the beam in the K800 exit channel varies with the coil settings. To constrain the beam to the proper direction of 6°, permanent magnet dipoles are planned. The dipole magnet has been designed so that the beam of 1.6 GeV/c can be bent by 4 degrees. The central field strength and the length of the magnet are 9.168 kG and 16 inches, respectively.

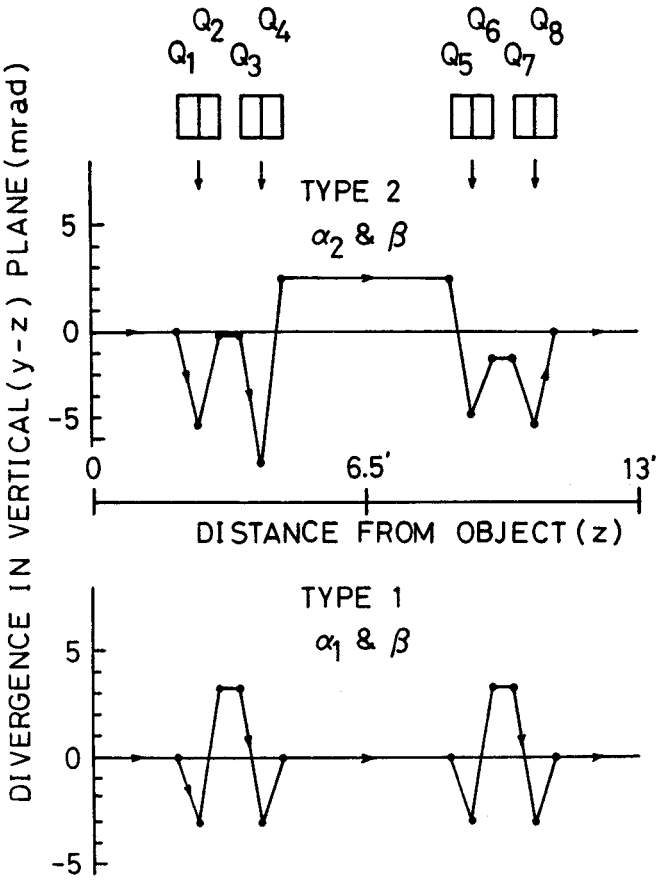

Fig. 3. Vertical divergence which develops in the quadrupole magnets due to the rotation. Type 1 and 2 correspond to the solutions α_1 and α_2, respectively,

It is also required that the deflection angle should cover the range of 4 degrees to -4 degrees to meet various acceleration conditions. Similar to the permanent magnet quadrupole, the permanent magnet dipole can be designed to handle beams with less momentum than 1.6 GeV/c by rotating its magnetic field around the z axis which is defined to be the central beam trajectory at the entrance of the magnet. One possible configuration of the dipole magnet is shown in Fig. 4. The 4 degree dipole magnet consists of four 1 degree dipole magnets, each of which consists of three layers of permanent magnets slags. Each layer is rotatable around the z axis. A relation between beam momentum and rotation angles, α and β was obtained by the TRANSPORT and RAYTRACE calculation with the constraint that each 1 degree dipole magnet is free of mixing horizontal and vertical motion. The relation obtained[3] is simply expressed by $\alpha=-\beta$ and $p(\mathrm{GeV/c})=1.6\cos(\alpha)$. Calculations are in exact agreement with the simple expression from ref. 3.

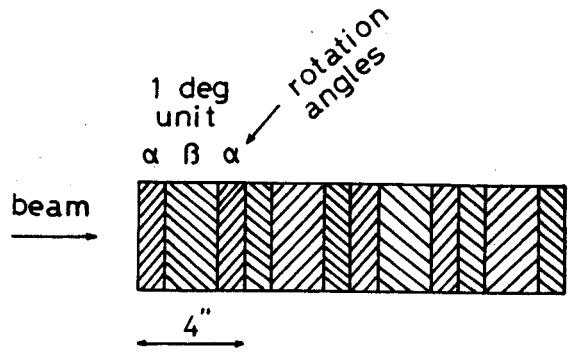

Fig. 4. 4-degree dipole consisting of four 1-degree units. α and β denote magnet rotation angles.

References

1. K. Halbach, NIM 169, 1(1980).
2. R.L. Gluckstern and R.F. Holsinger, NIM 187, 119(1981).
3. R.D. Hay and C.G. Masi, Proc. 1981 Linear Acc. Conf., 84.

IMPROVED ECR BEAMLINE X-Y STEERING MAGNETS

M.F. Williams, A.F. Zeller and J.A. Nolen

As part of the ECR beamline to the K800 cyclotron more of the X-Y steering magnets described in last year's annual report (p 172) will be needed. In order to improve the field quality two-dimensional calculations were done to simulate the finite length of the magnet. Because the gap is comparable to the length, the 2-D calculations overestimate the field in the middle, relative to the sides. To correct for this effect, the gaps between the coils above and below the median plane were increased to cause a faster decrease in the field strength with increasing radius. The gap was adjusted in the calculations until the slope of the field error matched the measured Mark I field profile. This is shown in fig. 1, together with the Mark I and Mark II maps. The POISSON calculation has been labeled with a times -1 to show that during fitting, the calculation were normalized to the Mark I data by this factor. It is seen that the Mark II has considerably better field quality than the Mark I. The fewer turns resulting from the increased gap gives a field of 90 G at 5A, but the addition of water cooling fixtures allows operation at up to 10A. Additionally, wooden protective covers have been added. Figure 2 shows one of the new magnets. The magnets have been completed and are ready for installation.

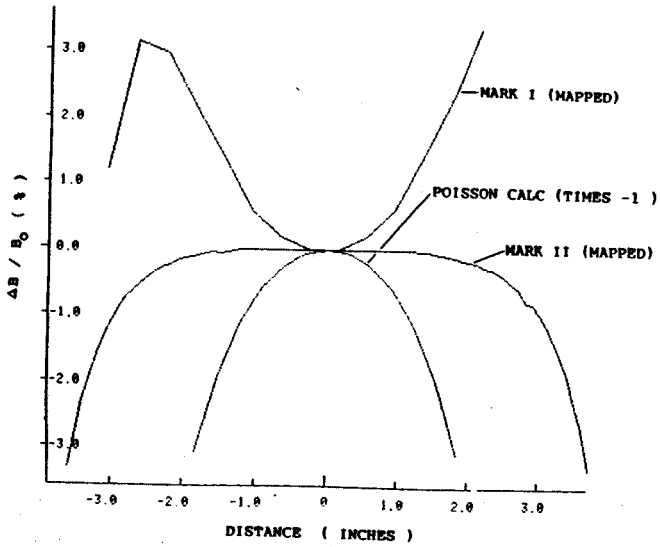

Fig. 1. Field uniformity for the Mark I and II magnets, together with the 2-D calculation which reproduces the Mark I field error slope.

Fig. 2. Photograph of one of the new steering magnets with the water cooling blocks attached.

BEAM CURRENT METER: EVERYTHING UP FRONT

A. McGilvra

The Beam Current Meter (BCM) is designed to measure a wide range of currents from one pico-Amp to 300 micro-Amps. The purpose of the BCM is to accurately measure beam currents in the beamlines of the K-500 and K-800 Cyclotrons.

The design was implemented as two stages; the first stage is a very high precision, low noise current-to-voltage transducer circuit, the second stage further amplifies the output of the first stage and contains the logic that controls the BCM. Together, these two stages allow a total of 16 ranges from 10 pico-Amps full scale to 300 micro-Amps full scale. The first stage, or front end, is the critical component and is the focus of this contribution.

The main problem with designing a front end capable of measuring currents as low as one pico-Amp is electrical noise. This noise is amplified by the extremely high gain of the first stage and appears at it's output. It is further amplified by the second stage and finally displayed.

There are two main classifications of noise: internal and external. The internal noise is generated by the circuit itself, by the operational amplifier that is the heart of the first stage and the resistors used in the feedback path of the op-amp. The external noise is generated external to the circuit by several sources: 1) electromagnetic interference (this is the most prevalent, especially the 60 Hz variety), 2) piezo- and tribo-electric effects produced in the cable connecting the BCM to the beam probe (these can also be very noticeable if the cable isn't secured properly and is allowed to sway or vibrate), 3) thermo-electric noise produced by the effective leakage resistance between the beam probe and the circuit ground (same as earth ground) (this can be a serious problem if the probe isn't kept clean and designed to maximize this resistance), 4) Van de Graaff effects produced by the cooling water flowing through the probe (these contribute a small, if any, part to the noise).

The electrical noise comes in two forms: current noise and voltage noise. Both the internal and external noise are made up of a current noise component and a voltage noise component. The total current noise is multiplied by the feedback resistance in the first stage (one giga-ohm on the 10 pico-Amp range) and then appears as a voltage at the output. The total voltage noise is multiplied by the ratio of the feedback resistance to the leakage resistance and then appears at the output. Since voltage noise makes up the majority of the total noise it is critical to maximize the leakage resistance by good probe design and frequent cleaning and thus minimize the gain factor of the voltage noise.

The thermo-electric noise mentioned above is proportional to the square root of the leakage resistance. Since it's gain factor has the leakage resistance in the denominator the component of output noise due to thermo-electric effects is actually proportional to one-over the square root of the leakage resistance.

To minimize the effect that all this noise has on the output of the BCM three things must be done: 1) maximize leakage resistance using materials with high resistivity and low moisture absorption, 2) shield the signal path of the beam current from external electromagnetic interference, 3) select first stage components with low noise properties. The first item was accomplished by using polyethylene insulated cable from the beam probe to the BCM and a teflon printed circuit board for the first stage

(PC Dynamics Co., Texas). The second item was accomplished by using twin-axial shielded cable (Belden # 9207, polyethylene insulated) and housing the entire first stage in a 5/16 inch thick iron box. The third item was accomplished by selecting a low noise op-amp (Analog Devices AD-515) to serve as the current-to-voltage transducer. It should be noted that although polyethylene has very high resistivity and low moisture absorption it has relatively poor piezo- and tribo-electric properties. Therefore the cabling should be well secured and not allowed to vibrate.

In situations where, despite best efforts, the noise is unacceptably high, an internal low-pass filter can be turned on that reduces the bandwidth of the BCM from 100 Hz to 1 Hz.

Another problem with designing a front end that can measure currents at the pico-Amp level is leakage currents. This problem was overcome in part by using a teflon printed circuit board which has a volume resistivity and surface resistivity several orders of magnitude higher than conventional fiberglass boards and also has a lower moisture absorption. A guard ring was used on the pc board around the two points where the beam current and ground are attached to the board. This guard ring significantly reduces leakage currents into the signal by draining to ground any current that tries to get from outside the ring to the beam current connections inside the ring. Finally reed relays were used instead of leaky analog switches to switch between the ranges of the first stage. Using reed relays presented a problem since they were activated by the external magnetic field encountered near the cyclotron. The 5/16 inch thick iron box that houses the entire first stage solved this problem.

Initial tests of the BCM indicate that the steps taken to reduce noise and leakage currents were successful. The accuracy and readability of the signal were greatly enhanced compared to previous beam current measuring devices.

The present status of the BCM design is as follows:

All circuit design is complete except details of communication to the outside world.

First Stage is built and tested.

Second Stage is built.

Overall Enclosure (to house first and second stages) design is nearly complete.

MEDICAL CYCLOTRON STUDIES

E.Blosser, G.Blosser, H.Blosser, J.DeKamp, J.Griffin, D.Johnson, F.Marti, R.Maughan, B.Milton, W.Powers, J.Purcell, J.Vincent & W.Young

Two medical cyclotron projects are underway at the NSCL, one involving construction of a K100 super-conducting cyclotron for neutron therapy, the other, a study of a K250 superconducting synchrocyclotron for proton therapy. After beams are obtained from the K100 cyclotron, it will be moved to Detroit and installed in the radiation oncology center of Harper Hospital, one of the city's largest medical facilities. In contrast the proton project is in an early design stage with possibilities for funding construction of a first such machine in a state of initial exploration.

The K100 cyclotron for Harper Hospital

System Concept. Many project details have changed significantly in the two years that the project has been in process, but major features remain the same as previously described[1,2] namely:

1) the cyclotron will mount on a ring type gantry and will be able to move in a full 360° arc about a supine patient.

2) the cyclotron will use a third harmonic, three dee rf system operating at 105 Mhz to accelerate deuterons to 50 MeV in a magnetic field of 4.58 tesla at the center and 5.4 tesla max. on the hills.

3) the deuteron beam will produce neutrons in an internal, thick beryllium target located 185 cm from the rotation axis of the isocentric mounting system and giving an estimated dose rate of 0.6 gray/min for a 10 μamp beam.

4) the cyclotron will be extremely simple with no frequency adjustment, no trimming coils, and no extraction system so that the overall system should be exceptionally reliable.

A central element of the cyclotron design which has changed significantly since the previous conference is the design of the superconducting coil. The coil is now a high current density, fully impregnated design, with a batch-fill helium system which includes thermal conduction elements designed to allow the coil to continue to operate until the liquid supply in the vessel is fully exhausted. The helium vessel includes a special array of vent pipes[2] which allow the vessel to operate as an atmospheric pressure, pool boiling system, which can still be fully rotated without spilling liquid helium.

Construction Status. Fig. 1 shows a model of the cyclotron and gantry system. Specifications require that the gantry be stiff enough to support the 50 ton combined load of cyclotron and counterweight with maximum deflections such that the axis of the beam always intersects a sphere of 3 mm diameter at the system isocenter, irrespective of the position of the cyclotron in the 360° rotation range of the system. The two large rings of 166" O.D. and 126" I.D. are the major element responding to this specification. Stress calculations predict that the shift in aiming point due to deflection of these rings will be less than ±0.050". The rings are supported by a system of 8 rollers one of which is driven by a 1 hp gearmotor, and the complete system is mounted on a precision base plate that measures 180" x 120". A floor allowing access around the treatment couch has been designed. This floor will be pushed out of the way by the gantry when the cyclotron is positioned at angles below the horizontal. (Many features of the combined floor and support system can be seen in Fig. 1.)

Fig. 1--Model of Harper Cyclotron showing cyclotron, and patient table and the isocentric gantry.

The main superconducting coils are constructed as a close packed, carefully ordered, epoxy impregnated winding. The conductor is wound in a true helix around a double wall bobbin, the bobbin outer wall fabricated from special, high nickel, 316 stainless steel, the inner wall being of copper. The stainless steel provides strength and vacuum integrity for the He vessel, the copper is a conduction element to cool the potted coil even when the helium level is low. The 0.031" by 0.055" superconducting wire is wound under tension onto the copper bobbin, with the winding tensioner set for 9,000 psi. Individual layers of wire are wound dry, but each layer of wire is preceeded by a layer of epoxy saturated paper, the paper serving as both a convenient method of applying the epoxy and as an additional back up insulator against the estimated 40 volt layer-to-layer quench potential. (In the winding process the formvar insulation on the superconductor was found to have substantial bare spots so that the additional layer to layer insulation is especially valuable.)

The initial cool down of the coil will be accomplished by filling the helium vessel first with liquid nitrogen and then with liquid helium. Thereafter, if the heat leak is in reasonable accord with design expectations, the vessel will be maintained at 4.2 K by weekly 100 liter refills. The batch-fill, potted-coil design is thought to be particularly adapted to the environment of an average hospital, where the skills required to procure and batch transfer helium are likely to be.

Medical Cyclotron rf System

The rf system for the medical cyclotron consists of three mechanically coupled dees operating in the 3rd harmonic mode ($\omega_{rf}=3\omega_o$) with dees in the valleys of the magnet. The operating frequency of the system is 105 Mhz, which will be supplied by a commercial 25 kw FM broadcast amplifier. Each dee has two quarter-wave stems going up and down through the magnet in the fashion of the K500 and K800. The dee stems each have an adjustable short which will be permanently clamped in place once the system is tuned. The rf return currents flow through copper plating on the pole tips and through a water-cooled copper plate in the bottom of the valley. At 105 MHz, the dee stems are quite short (≈5") and do not reach out of the magnet; the dee stem holes through the yoke will therefore be blocked with plugs behind the shorts for added neutron shielding. Coupling of the rf drive will be through a special coupling loop on one of the six dee stems. The dees themselves will be made from 1/2" aluminum plate to reduce residual radioactivity.

A low power model has been built and tested to confirm the system design. This model is now being modified to test the coupler design. The central region geometry has been tested in the K500 where it operated successfully with 40 kV across a 4 mm gap between the ion source and the dee (with the source in operation).

K250 Medical Synchrocyclotron

In the United States, considerable

attention has recently been directed toward the development of accelerator systems optimized for radiation therapy with protons. An informal group, PTCOG[3], has been organized and has had a number of meetings. A number of different accelerator systems have been described at these meetings, including a variety of proton synchrotron designs and a high field synchrocyclotron, the latter a system which is under study at NSCL.

System Concept. The design energy goal for a proton therapy accelerator is generally taken to be 250 MeV (the magnet K value required to produce 250 MeV protons is 285 MeV; in the fashion of other MSU cyclotrons, we name the cyclotron based on the Q/A formula for energy). Beam currents of a few nanoamps are marginally adequate and tens of nanoamps are comfortable for even the largest tumors. Synchrocyclotrons are used in present proton therapy programs, but the machines are older, massive room temperature machines which are located in physics laboratories and are overall poorly matched to a hospital environment. Such a cyclotron would also be inordinately costly to reproduce in present conditions. If the synchrocyclotron is redesigned as a superconducting high field device, the mass and cost are greatly reduced and an overall system with many appealing features results. One likely arrangement for such a system has the 70 ton cyclotron mounted on a gantry in a fashion similar to the neutron system. Systems in which the cyclotron is fixed and the beam feeds to one or more beam swinger systems are also quite attractive.

The features of the high field synchrocyclotron which are most questionable are 1) can a proton beam be extracted from a 5 tesla magnetic field (none of the present superconducting cyclotrons attempt to do this), and 2) can a reasonable system for varying the energy of the output beam can be achieved in a synchrocyclotron system (synchrotrons of course meet this requirement with ease). A strength of the synchrocyclotron is that it easily exceeds the intensity requirements (by orders of magnitude if desired).

Extraction Studies. As in room temperature synchrocyclotrons, beam extraction from the superconducting synchrocyclotron is based on the regenerative process invented by Tuck and Teng, and perfected by Lecouteur. The main difference in the two situations is simply a change of scale.

To obtain an approximate quantitative picture of the behavior of an actual regenerative extraction system, the fully saturated iron approximation has been used to obtain the magnetic field of a rather simple set of regenerator bars. The regenerator used has a constant angular width of 30° and starts just inside the $\nu_r=2\nu_z$ coupling resonance (n=0.2) in the unperturbed field. The regenerator constitutes in effect a powerful field bump that drives ν_r into the $\nu_r = 2/2$ stopband while simultaneously depressing the values of ν_z. The main difficulty with regenerative extraction is the potential loss of vertical stability as a result of the coupling resonance. Although the regenerator gradient depresses the value of ν_z well below the resonant value for particles close to the equilibrium orbit, the rapidly increasing radial amplitude produced in the extraction process drives ν_z into the resonance thereby making the vertical motion unstable. This phenomenon therefore limits the maximum radius-gain per turn that can safely be achieved. Figure 2 is an r vs θ plot of the last five axially stable turns of the central ray of the extraction trajectory; the figure shows the characteristic "node" at θ=65°, and also that a radius gain per turn of about 0.5" can be achieved near θ=110°. This radius gain is comfortably adequate for inserting an iron bar magnetic channel of the form used in the K800's extraction system as indicated schematically by the dashed outline in the figure. We therefore

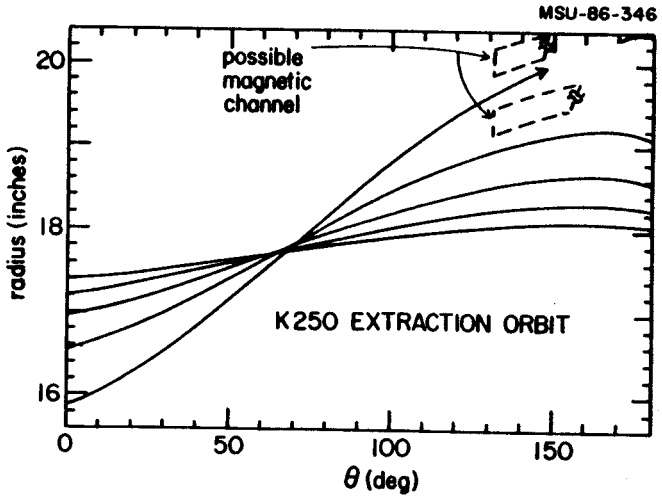

Fig. 2--r vs. θ successive extraction orbits (just prior to the onset of the axial instability).

conclude that extraction from a high field 250 MeV synchrocyclotron is a reasonably straight forward design problem. Detailed studies of specific magnetic channel geometries are in progress.

Beam Transport and Analysis. The primary beam transport problem is the need to spread the dose over large tumor volumes (large in both transverse dimensions and in depth) with a dose uniformity of no worse than 5% and with minimum dose outside the tumor volume. Two main methods are available for the transverse spreading, namely, passive spreading by multiple scattering and active spreading using a deflecting element to scan a small beam spot over a large area. The longitudinal spreading requires changing the beam energy - this can be done by a variable absorber or by changing the energy of the accelerator. A possible third type of system involves focusing the beam to a line and moving the patient relative to this line as at the meson facility at SIN. In general, passive systems have the advantage of reducing the risk of local over exposure of the patient should the deflecting element fail to function, but the beam is utilized less effectively in the sense that much of the beam will be stopped in slits and collimators as the axially symmetric distribution produced by the scattering is shaped to match the tumor. The synchrocyclotron tends to match best with a scattering type system in that it easily produces more intensity than is needed (treatment times of about two minutes are considered ideal - times less than one minute are considered to be too fast).

A major cost issue in either a scattering or a scanning system is the distance from the last beam element to the patient - if this distance is large, the equipment required to rotate the beam transport system in an isocentric pattern becomes large and costly and the cost of the treatment room is also greatly increased. Scattering systems which place the scattering foil in front of the last 90° bending magnet are therefore very attractive. A likely beam spreading method for such a system has been developed[4] which gives excellent uniformity at the tumor, convenient energy variation, and primary beam defining elements are relatively far from the patient so that effective shielding of secondary neutrons can be accomplished.

References

1. H.G. Blosser, W.E. Powers, R.L. Maughan, C.G. Orton, D.P. Ragan, G.F. Blosser, R.J. Burleigh, and E.B. Jemison, Proceedings Tenth International Conference on Cyclotrons (1984) 431.
2. H. Blosser, J. DeKamp, J. Griffin, D. Johnson, F. Marti, B. Milton, J. Vincent, G. Blosser, E. Jemison, R. Maughan, W. Powers, J. Purcell, and W. Young, Transactions of Nuclear Science 5 (1985) 3287.
3. Proton Therapy Cooperative Group, M. Goitein, Sec., Depart. of Radiation Medicine, Mass. Gen. Hospital, Boston, MA 02114.
4. E. Kashy and B. Sherrill, Nucl. Inst. and Meth. (in press).

BEAM EXTRACTION STUDIES FOR A 250 MeV SUPERCONDUCTING SYNCHROCYCLOTRON

M.M. Gordon and X.Y. Wu

A 250 MeV superconducting synchrocyclotron for use in cancer therapy is being designed with a central field of 57 kG and a pole radius of 21 in. Use of a superconducting magnet increases the field and decreases the size by about a factor of three, and this size compression greatly affects all systems, including extraction.

Beam extraction from synchrocyclotrons is based on the regenerative process invented by Tuck and Teng and then developed by LeCouteur in the 1950's. Our choice of regenerator parameters is derived from an extrapolation of those used in the extraction system of the Harvard cyclotron.[1]

Before the regenerator is added, the magnet is axially symmetric, and the values of ν_z rise with increasing energy while the ν_r values fall. In the present design, these values cross the $\nu_r = 2\nu_z$ (n=0.2) resonance at 19.1 in., and this radius determines the approximate starting point for the regenerator.

The iron configuration of the proposed regenerator is shown schematically in Fig. 1 along with the field change and field gradient that it produces. This device has an average angular width of 30° and has terraced edges that are designed to reduce the nonlinear effects associated with the rapid azimuthal field variations.

The regenerator provides a powerful field bump whose strong gradient drives ν_r into the $\nu_r = 2/2$ stopband while simultaneously depressing the values of ν_z. This is shown in Fig. 2 where values of ν_r and $2\nu_z$ are plotted as a function of energy. The pair of curves for the unperturbed field come together and cross at 258.9 MeV where n=0.2, as noted above. With the regenerator present, the two curves diverge with

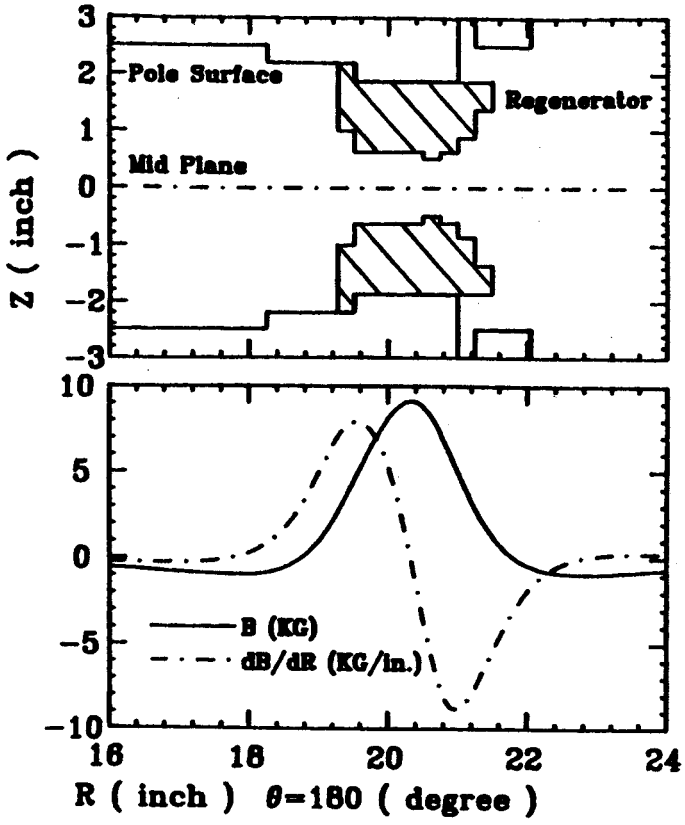

Fig. 1. At top, radial profile of regenerator situated on the edge of the magnet poles. At bottom field B (solid curve) produced by regenerator, and its gradient dB/dr (broken curve) vs. radius. Plots are for θ = 180°, the center of the regenerator.

ν_r rising sharply to $\nu_r = 1$ at 253.7 MeV, which becomes the ultimate extraction energy. At this point, $\nu_z = 0.29$.

The nature of the extraction process can best be understood by examining radial phase plots like the ones shown in Fig. 3 for E = 252.5 MeV. Here values of p_x vs. x are plotted once per turn at θ = 180° (the center of the regenerator) for three different orbits, one stable and two unstable, which clearly show the boundary of the stability region. This region shrinks to zero at E = 253.7 MeV where $\nu_r = 1$,

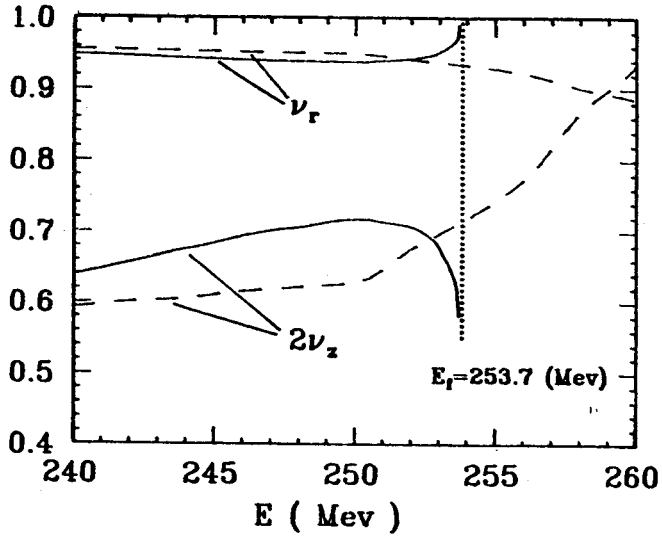

Fig. 2. Plots of ν_r and $2\nu_z$ vs. energy both without regenerator (broken curve) and with regenerator added (solid curve). ν_r=1 at 253.7 MeV, the peak extraction energy.

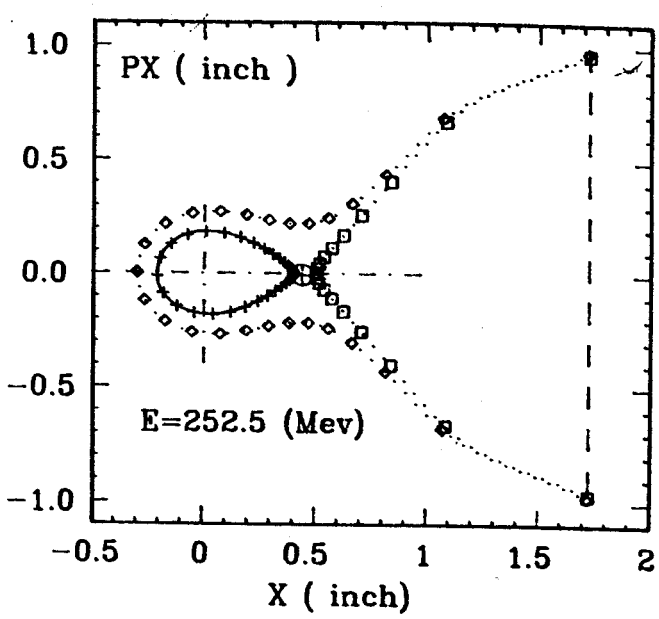

Fig. 3. Radial phase plots for three orbits at 252.5 MeV showing stability region and asymptotes produced by regenerator. The stability region shrinks to zero at 253.7 MeV.

and is sufficiently large at 252.0 MeV to encompass most of the internal beam that can survive the extraction process. One can therefore see that as the protons accelerate outward, they encounter a rapidly shrinking stability region that eventually causes their orbits to spill over the boundary into the radially unstable region. As shown in Fig. 3, the phase points then move onto the outflowing asymptote along which their radius-gain per turn increases exponentially thereby enabling the protons to clear the septum and enter the extraction channel. Because the stability region shrinks so rapidly, the energy spread in the extracted beam will be less than about 1%.

Vertical stability ultimately limits the radius-gain per turn that can be achieved in the regenerative process. That is, as the orbits move progressively farther off-center, strong coupling effects eventually cause the vertical height of the beam to expand beyond the allowed limits.

Figure 4 shows plots of r vs. θ between θ = 0 and 180° corresponding to the last four turns of the two radially unstable orbits depicted in Fig. 3. These plots (and those in Fig. 3) have been terminated before the vertical motion becomes seriously unstable. In addition to showing the characteristic "node" near θ = 50°, these r vs. θ plots indicate that a radius gain per turn of about 0.5 in. can be achieved near θ = 110° where the channel septum would be inserted.

The design of the magnetic channel system is still being studied. This system will consist of a sequence of passive magnetic elements that bend and focus the beam along its path out of the cyclotron. The structure and design of these elements is based on the analogous channel systems used in the K500 and K800 cyclotrons.

References

1. G. Calame, et.al., Nucl. Instr. and Meth. 1(1957)169.
2. M.M. Gordon and V. Taivassalo, Nucl. Instr. and Meth. A247(1986)423.

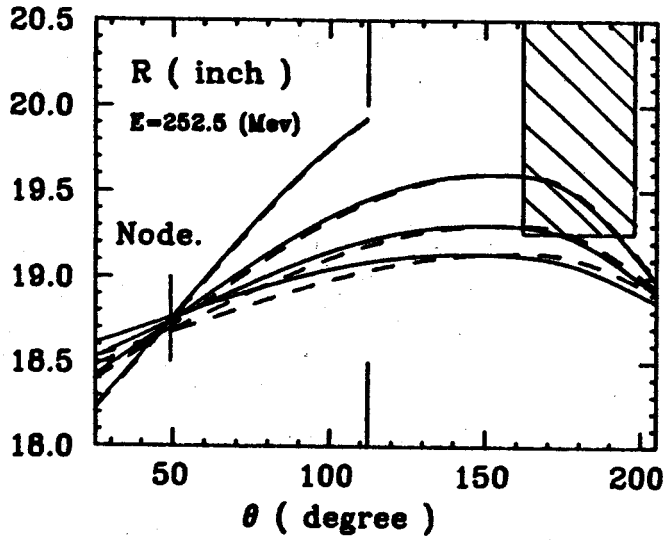

Fig. 4. Plots of r vs. θ for the last four turns of the two unstable orbits (depicted in Fig. 3) showing growth in turn separation at θ = 112°, the channel entrance. The regenerator shims lie within an area from θ = 162° to 198° and from r = 19.25 to 21.5

Beams of charged particles of large spatial dimensions with uniform areal densities at a given location are essential in radiation treatments of tumors, as well as for many applications of charged particle beams. A simple method for the preparation of such beams is to send the beam from some accelerator through a thin scattering target. The multiple scattering of the beam which arises mainly from the interaction of the projectile with the nuclear charge of the target nuclei results in an approximately gaussian angular distribution of the particles emerging from the target[1].

By moving the position where irradiation is to take place far from the beam spreading target, the radiation field is enlarged and uniformity of dose is obtained at the cost of intensity. Two methods have been discussed by Koehler, Sneider and Sisterson[2] to improve the homogeneity of radiation fields, with minimum reduction in intensity. In the first, one sweeps a narrow beam over a target. In the second, a double scattering scheme,one adds an additional beam spreading target downstream from the first target, with the second target appropriately obstructed. The net result is an improvement of the flatness of the distribution over a certain irradiation area. A recent calculation by Gottschalk using the double scattering system with a variable circular obstruction before the second scattering[3] indicates a uniformity in the measuring plane of 10% with an efficiency of about 32%, which is considered satisfactory for medical treatment. However, when the scatterings occur within a beam transport or analysis system, a potential weakness of the double multiple-scattering method is the enlargement of the effective object size of the system by the second scattering and the increased loss of intensity due to nuclear interactions.

scattering and the increased loss of intensity due to nuclear interactions.

We have found a way to use non-linear optics to transform a large fraction of particles which have a gaussian-like areal distribution into a uniform one. Calculations using the magnetic-optics computer code TURTLE[4] show that the proposed method achieves excellent homogeneity in the measuring plane with high beam efficiency as discussed below.

The method makes use of magnetic lenses of high order, with octupoles being the lowest order required for symmetric distribution. The particles which travel near the axis of the octupole are unaffected since the octupole field varies as the cube of the radius, while the particles away from the axis are deflected in a non-linear manner causing a flattening of the final particle intensity distribution. The octupoles are placed at the positions where waists in the beam envelope are located in order to decouple the effects in the x and y planes. Figure 1 shows a sample layout which clarifies the requirements of the method. A charged particle beam from an accelerator is focussed at position 1, where depending on the requirements, either 1) a scatterer of appropriate atomic number Z and thickness is located, or 2) the beam from the accelerator is focussed. A beam defining slit follows immediately and acts as the object of the quadrupole triplet. The tails of the beam divergence entering the quadrupole triplet can be limited by the next aperture, placed ahead of the first quadrupole.

The strengths of the magnetic fields of the quadrupoles in the doublet are adjusted so that the foci in the two planes are displaced from each other along the beam trajectory. These foci are close to the final location of the octupoles, with the actual positions chosen at the waist of the beam in each dimension after taking into account the effect of the octupoles.

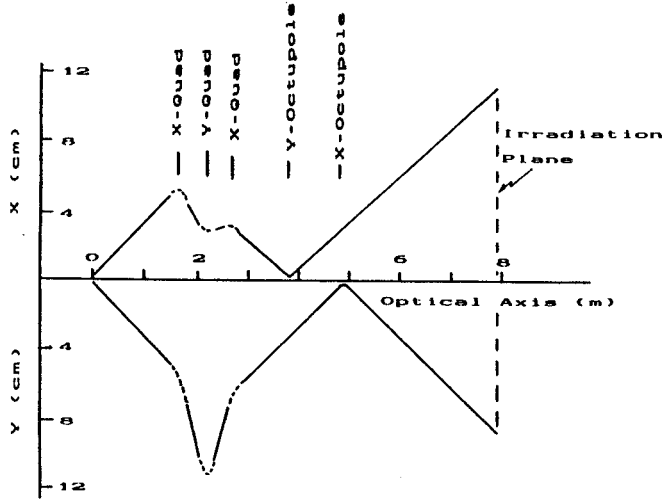

Fig. 1. An example arrangement of part of a beam transport system. Fig. 1a shows the x-envelope of a beam and figure 1b the y-envelope. The positions of the octupoles, used to homogenize the particle areal density, are shown at the waists of the system.

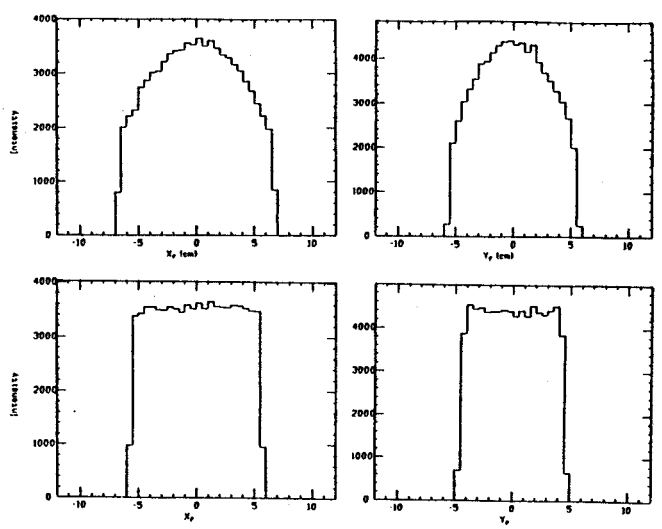

Fig. 2. Projections of the particle distributions on the x and y axes for an initial distribution of a uniformly populated ellipse in x-θ and y-φ phase spaces. In the upper part, the octupoles are not used. In the lower part, the octupoles have been turned on and adjusted to homogenize the distribution. The fluctuation in the curves reflect the statistical nature of the sampling of particles traversing the system. A set of slits before the first quadrupole limit the acceptance of the system to 80% of the initial distribution.

the waist of the beam in each dimension after taking into account the effect of the octupoles.

Also shown in fig. 1 are the envelopes of the beam in both x and y as function of longitudinal displacement. The upper part of fig. 2 shows the projection of the particle intensity on the x axis and on the y axis at the irradiation position with the octupoles turned off. These were obtained from a randomly selected set of rays within the initial phase space distribution of a uniformly populated ellipsoid, as calculated in the code TURTLE[4]. It is clearly seen that the peaked nature of the distributions is unaffected as it travels through the system.

In the lower part of fig. 2, the two octupoles have been turned on to the appropriate values for flattening the two dimensional particle intensity distribution. Since the fields required in the octupoles can be quite large, the working apertures can be chosen to reduce the required field strength at the poles and the cost of the lenses. The envelopes following the octupoles have been slightly reduced is size. The role of the octupoles in flattening the particle distributions is clearly demonstrated by the calculation of the distribution on the measuring plane shown in fig. 2. The homogeneity is better than 10% for a beam which includes more than 70% of the initial beam. Figure 3 shows the x-y projections of the particle distribution at the measuring plane, since projections on the x and y axes are not sufficient to ascertain the uniformity of the particle distribution. Fig. 3a shows the results without the use of the octupoles while in fig. 3b, the octupoles are used.

The octupoles physical orientations are the same at both positions, but their magnetic fields have opposite signs, since, depending on the plane of action, they are placed ahead and following the respective beam waists. The octupoles act essentially independently of each other, because of their placements at these waists. Because of the strong effect of these elements on the phase space, it appears best to place them close to the end of the transport system. We note that the octupole settings depend on the absolute value of the width of the

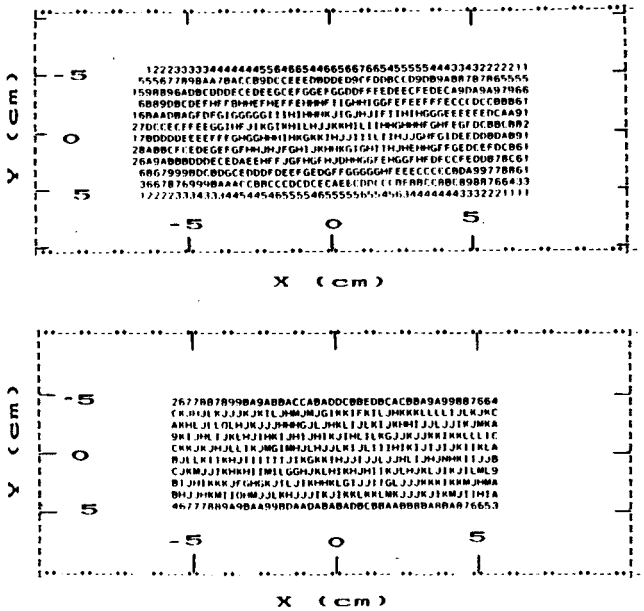

Fig. 3. Areal density plot in the x-y plane of the particle distribution shown in fig. 2. In fig. 3a the octupoles are unused. In fig. 3b the octupoles have been turned on and adjusted to homogenize the distribution. The number of particles is given by the numerals or letters, with 1 = 1-9, 2 = 10-19,... 9 = 80-89, A = 90-99, B = 100-109, etc.

distribution, and need to be adjusted accordingly.

The size of the irradiation field can be controlled by adjusting the distances and the size of the aperture ahead of the first quadrupole. Proper limits of the field can be assured by a mask at the irradiation location. For very small size irradiations areas, other procedures which include a smaller object slit as well as the use of an initial scatterer of lower atomic number Z may be used.

References

1. E. Segre, Nuclei and Particles, (W.A.Benjamin, N.Y.) p.39 (1965).
2. A. M. Koehler, R.J. Schneider, and J. M. Sisterson, Medical Physics 4, 297,(1977).
3. B. Gottschalk, Double-Scattering System with Optimum Dose Uniformity in Proton Therapy, (private communication)to be published.
4. D. Carey, 'TURTLE', Fermi National Accelerator Laboratory, report 64-2041.000.

TRIAL OF BEAM RECONSTRUCTION USING A FILTERED BACK PROJECTION

Y.D. Ahn, S.M. Austin

One cannot get sufficient information about particle beam distribution in two dimensions by using only two projections (on the x and y axes), because these don't give a unique solution. Consider the two beam distributions (Fig.1) represented by lines (1) and (2) where

$$y = \frac{d - c}{a - b} x + e_1 \qquad (1)$$

$$y = -\frac{d - c}{a - b} x + e_2 \qquad (2).$$

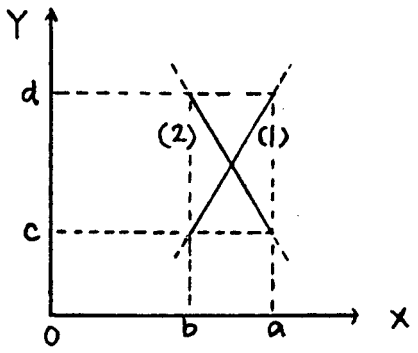

Fig. 1 Example of ambiguity in reconstruction from 2 projections.

The two distributions have the same projections. In order to get two dimensional information, we are trying tomographic beam reconstruction and as a first trial we used a filtered-back projection method[1] (based on the results from a paper[2] in radio astronomy) to get information about the beam's density distribution and size in a plane perpendicular to beam's direction (See Fig. 2.).

In this method, choosing large number (n) of projections (in an n x n array) is desirable for good precision. But we chose n small for convenience and because the current measuring wires are not much more than a factor of 10 smaller than the beam diameter. Since this decreases the precision, we tried to determine whether filtered-back projection is useful for our purpose or not. We chose 9 parallel wires (projections) per angle and moved the apparatus through 5 angles (spaced by $2\pi/10$ from $\phi=5\pi/10$ to $-3\pi/10$). ϕ is the angle between plane perpendicular to projection direction and x-axis (Fig.2). Trial projections we calculated from the (current density) shown in Fig.3 (a) and Fig.4 (a). The results of the reconstruction are shown in Fig.3 (b) and Fig.4 (b).

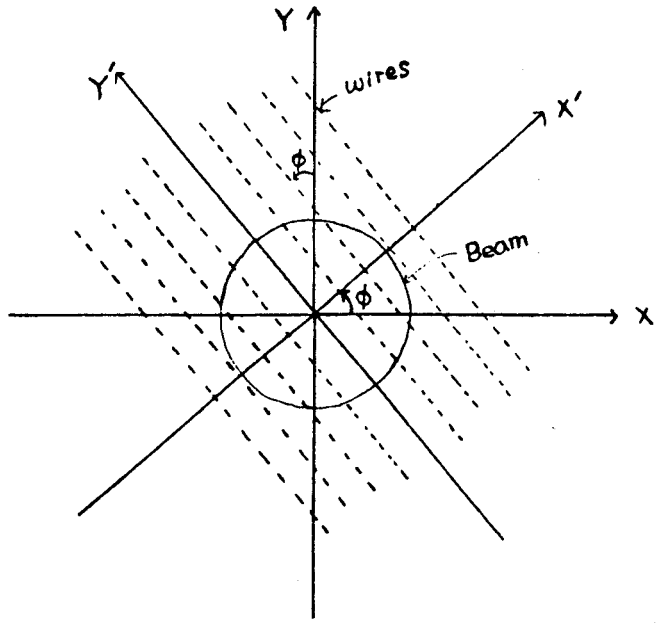

Fig. 2 Geometry used from computer trial of reconstruction technique.

We found that the test of the beam's size was reasonable and we could find the peak of the current density but the value had an error of 17%. The results are promising in that reasonably accurate values of the current density ρ are obtained especially in situations where ρ is slowly varying. It appears that a simple device based on these principles could provide information on beam shapes not otherwise available. A possible application is to the ECR injection line.

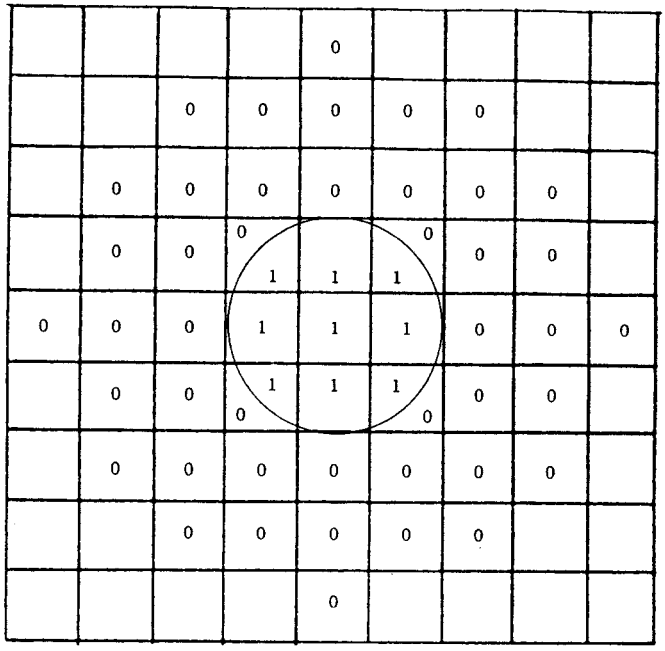

Fig.3(a) Trial current density.

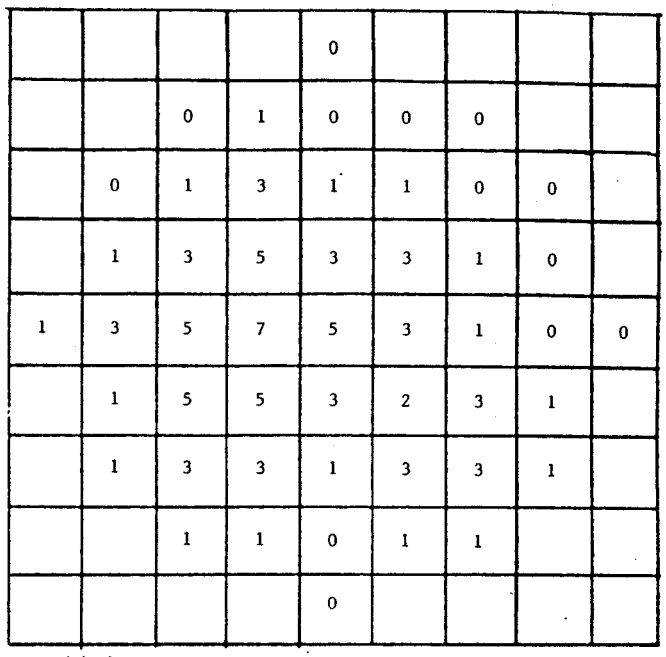

Fig.4(a) Trial current density.

				0.06				
		0.1	-0.04	0.06	-0.04	0.1		
	-0.1	-0.04	0.01	0.09	0.01	-0.04	-0.1	
	0.09	0.01	0.55	0.78	0.55	0.01	0.09	
-0.03	-0.02	0.13	0.79	1.03	0.79	0.13	-0.02	-0.03
	0.09	0.01	0.55	0.78	0.55	0.01	0.09	
	-0.01	-0.04	0.01	0.09	0.01	-0.04	-0.01	
		0.1	0.04	0.06	0.04	0.1		
				0.06				

Fig.3(b) Results of the reconstruction.

				0.509				
		-0.11	0.548	0.953	0.06	-0.52		
	0.725	1.31	2.07	1.76	0.64	0.129	0.34	
	1.24	3.44	4.10	3.27	2.18	0.94	-0.3	
1.12	2.42	5.11	5.80	5.34	3.1	2.0	1.0	0.7
	1.35	3.97	4.21	2.75	2.21	1.96	0.65	
	1.87	2.77	2.54	2.23	2.49	2.32	1.41	
		0.32	0.57	0.33	1.02	0.60		
				-0.1				

Fig.4(b) Results of the reconstruction.

References

1. Brooks, R.N., and DiChiro, G.: Theory of image reconstruction in computed tomography. Radiology, 117:561, 1975.

2. Bracewell RN, Riddle AC: Inversion of fan-beam scans in radio astronomy. Astrophys. J. 150:427-434, Nov. 1967

STATUS OF THE MSU 4π ARRAY

G.D. Westfall, M. Maier, L. Morris, D. Swan, S. Tanaka, A. Vander Molen, J. van der Plicht, J. Winfield, M. Williams and J. Yurkon

The MSU 4π Array is designed to measure all the charged particles emitted from nucleus-nucleus collisions.[1] To accomplish the detection of particles ranging from fission fragments to high energy protons, the array is designed such that the stopping power of the detectors increases with the range of the particles to be detected. For fission fragments a low pressure multi-wire proportional counter (MWPC) is used. Target-like fragments will pass through the MWPC and will be detected in a Bragg curve counter (BCC). Energetic light particles will pass through both the MWPC and the BCC and will be detected in a fast/slow plastic scintillator phoswich telescope (FST).

The geometry of the array is a truncated icosahedron (soccer ball) with twenty regular hexagonal faces and twelve regular pentagonal faces. Two of the pentagonal faces are used for beam entry and exit leaving twenty hexagonal and ten pentagonal faces to be instrumented. Each hexagonal (pentagonal) face will support a subarray consisting of one MWPC, one BCC and six (five) FSTs. The entire array will consist of thirty MWPCs, thirty BCCs, and one hundred seventy FSTs.

The parts for the MWPCs are all in house. The prototype hexagonal and pentagonal detectors have been assembled and tested with fission fragments. Currently the gas bypass holes are being drilled. The foils and wire planes are still to be fabricated.

The FSTs are being fabricated by Bicron, Inc. Bicron has contracted to perform the scintillator fabrication, machining, and assembly for the FSTs. Each subarray is delivered as a unit with the fast plastic ΔE counters, slow plastic E counters, and the holes and grooves necessary for the mounting of the BCC/MWPC assembly as well as the mechanical mounting of the entire subarray. Currently Bicron has delivered fourteen of the thirty two subarrays that will be constructed. One of these production modules has been tested with beam from the K500 Cyclotron and performs very well.

The BCC construction has been dependent on the delivery of the FST arrays because the BCC must mount directly to the scintillators. The FSTs form the pressure window for the BCC. In addition the fronts of the fast plastic ΔE counters are aluminized to form the anode of the BCC. An evaporator is now operational that can aluminize the front faces of the scintillator arrays. The current design of the BCC calls for a stainless steel front window support attached to tapered G10 walls that in turn attach to the Frisch grid mount that is attached to the scintillators. Assembly fixtures have been constructed for the BCCs.

The construction of parts for the vacuum vessel is now complete. The parts have been carefully cleaned and are being assembled in anticipation of sealing and pumping down.

The computer controlled gas handling system is nearly complete. It consists of a VME based 68010 computer system interfaced to the controller valves, pressure transducers, and solenoid valves. There are twelve independent systems each supporting five gas counters in series. This control system will also control the programmable high voltage supplies for the FSTs and gas counters.

The data acquisition system consists of five CAMAC crates containing programmable logic, programmable discriminators, Fast Encoding and Readout ADCs (FERAs), and time to FERA converters (TFCs). The data will be read out

from the FERAs over an ECL bus. The entire system of data aquisition will reside in the vault. The system is controlled by a VME based 68020 processor with 68881 numeric coprocessor. This computer allows software triggering involving complicated computations such as particle identification or topology selection.

The preamplifiers for the MWPC anode and position signals and the BCC anode signals will consist of single chip amplifiers mounted directly on the counters. The photomultiplier bases are designed and feature one cable that carries both the high voltage and the signal.

The entire system should be ready by the end of 1987.

References

1. G.D. Westfall, J.E. Yurkon, J. van der Plicht, Z.M. Koenig, B.V. Jacak, R.Fox, G.M. Crawley, M.R. Maier, B.E. Hasselquist, R.S. Tickle, and D. Horn, Nuclear Instruments and Methods, A238, 347 (1985).

HIGH RESOLUTION HEAVY FRAGMENT HODOSCOPE

T.K. Nayak, T. Murakami, W.G. Lynch, K. Swartz, D.J. Fields,
C.K. Gelbke, Y. Kim, K. Kwiatkowski[a], J. Pochodzalla, M.B. Tsang, F. Zhu

Recent studies of two-particle correlations of emitted fragments in heavy ion collisions have revealed many interesting phenomena (Ref. 1 and the references therein). However, because of the lack of position information, it was not possible to obtain the correlations at small relative momenta with good energy resolution. Also, so far the coincidences have been made only between light particles ($z_f<3$). To study the importance of particle unstable states in a fragmentation process, it is necessary to measure the two-fold coincidences between isotopically resolved heavy fragments with $2<z_f<9$ and isotopically resolved H and He isotopes. A high resolution heavy fragment hodoscope using position sensitive gas detectors was built for the purpose of studying the emission and sequential decay of particle unstable complex fragments.

The hodoscope consists of 13 telescopes in total in a close-packed array. Nine telescopes are used to measure light particles (called LP telescopes), i.e., isotopes of H and He, and 4 telescopes are used to measure heavy fragments (called HF telescopes). The LP telescopes are set at a distance of 25cm from the target and the HF telescopes are set at 18cm. The angular acceptance of the hodoscope was between -19° and +19°. The optimised relative angle between neighboring LP and HF telescopes is 8°.

The LP telescope consists of a position sensitive gas detector (of 6 msr solid angle) followed by one silicon ΔE detector of 200 micron, one lithium drifted transmission type silicon ΔE detector of 5mm thickness and one NaI E detector. The HF telescope consists of a position sensitive gas detector (of 6 msr solid angle) followed by two silicon ΔE detectors of 75 and 100 micron thicknesses and one lithium drifted silicon, E detector of 5mm thickness.

Each of the gas detectors is a two-dimensional position sensitive detector having two cylindrical compartments and each of the compartments having one wire orthogonal to the one in the other compartment. The wire material is nichrome (80% Nickel and 20% chromium) of 7.62 micron thickness. For the entrance and exit windows of the HF gas counters, 1.5 micron aluminised polyester was used and for the LP gas detectors we used the same material of 6.4 micron thickness. The foil in the middle of the detector was aluminised on both sides and of 1.5 micron thickness. The spacer holding this middle foil had a hole for continuous gas flow from one compartment to the other. The diameter of LP gas detector is about 3cm and the length of each compartment 1.2cm. The corresponding numbers for the HF gas detector are 2.3 cm and 1.2cm. The chamber gas was isobutane bubbled through methylal. The percentage of methylal was 20% to 80% of isobutane. Methylal was used to prevent polymerisation of the counters. The LP detectors were operated at a gas pressure of 100 torr and the bias applied to the wires was about 1250 V. The HF detectors were operated at 40 torr gas pressure and 900 V bias. The position from each of the counters was obtained by the method of charge division.

For the purpose of calibrating the detectors, a mask was built and was put in front of the hodoscope at a distance of 16.5 cm from the target center. The holes in the mask were made taking care of the different slanting angles of the individual counters. The holes in each mask pattern are 1mm diameter and the center to center distance of holes is 1.5mm. Using an alpha source (^{244}Cm), we obtained the image of the mask pattern from the gas detector. A typical density plot pattern is shown in fig. 1. It is evident from this that we could measure

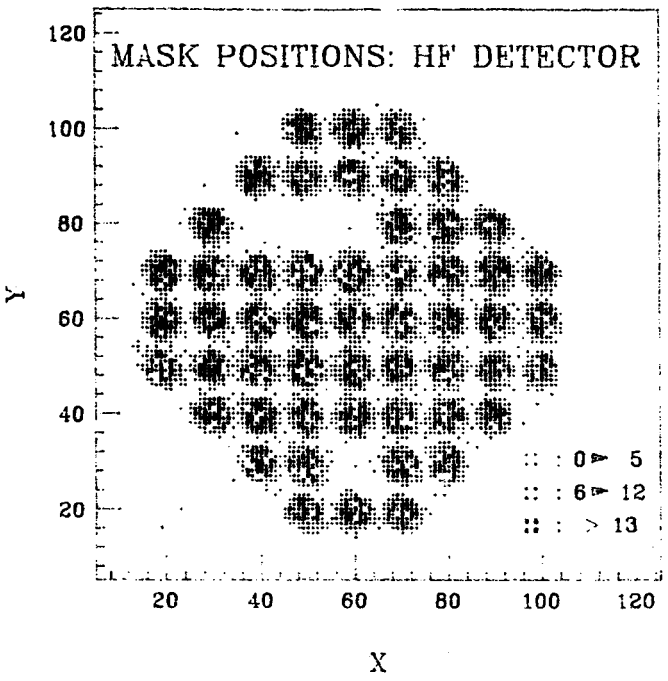

Fig. 1. Two dimensional mask pattern obtained by position sensitive gas detector.

the position to 100 micron accuracy in this case.

This hodoscope was used in an actual experiment with ^{14}N beam at a bombarding energy of 35 MeV/nucleon and Ag target. The analysis of the experiment is in progress.

---

a. Indiana University, Bloomington,In.

References

1. J. Pochodzalla et al. MSUCL-569

PARTICLE IDENTIFICATION BY PULSE SHAPE DISCRIMINATION WITH INORGANIC SCINTILLATORS

D.A. Cebra, D. Fox, M.R. Maier, D. Swan, P.B. Ugorowski, G.D. Westfall,
D.K Wilson and J.E. Yurkon

The light output of inorganic scintillators depends on particle type: magnitude and decay time of the light pulse is different for lightly and heavily ionizing particles, e.g. electrons and protons at the same incident energy. The difference in decay time-related to the pulse shape-can be used to distinguish between the particles incident on this type of scintillator. In CsI and NaI highly ionizing particles produce faster decaying pulses. In BaF_2 the fast component in the scintillator decreases for highly ionizing particles.

We have investigated the response of NaI, CsI and BaF_2 scintillators together with a phoswich detector[1] to particles ranging from protons to lithium isotopes.

We used 1.5" diameter x 4.0" long cylindrical NaI, CsI and BaF_2 scintillators coupled to appropriate photomultiplier tubes-UV sensitive in the case of BaF_2. We built standard ΔE-E telescopes using 200μm thick silicon transmission detectors, and the scintillators and the phoswich detector (1mm fast plastic followed by 5" slow plastic 2cm X 2cm square) as E detectors. Therefore, any particle hitting the E detectors could be identified by the standard "energy loss" method. Therefore, we could clearly identify the particle type (p,d,t, etc.) for every particle hitting the E detector.

These telescopes were used to detect fragments coming from bombarding a thin gold target with 150 MeV lithium ions. At forward angles, the lithium fragments produced p, d, t, ^{3}He, α, ^{6}He, ^{6}Li and ^{7}Li particles. An example of a ΔE vs E plot is given in Fig. 1. The signal coming from the E detectors were fed to two charge integrating ADC's, one with a long gate (total energy) and one with a short early gate ("fast" component).

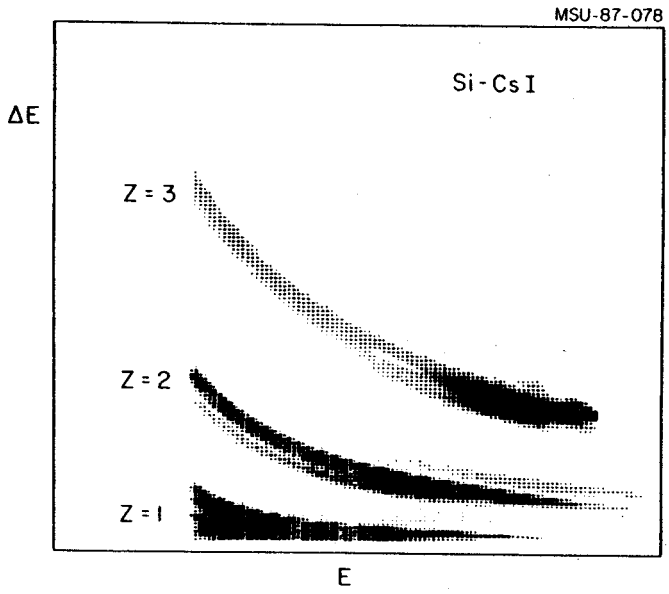

Fig. 1. ΔE vs E plot for Si-CsI telescope.

Figure 2 shows a fast vs total energy plot for CsI. This "pulse shape discrimination" works down to rather low energies (~ 4 MeV in our setup). For particle identification CsI seems to be best suited, however, it suffers from rate limitations due to its long light decay time. NaI does not separate the lithium isotopes as well as CsI, and BaF_2, due to its low light output can only be used to separate p, d, t and α, the lithium isotopes are no longer well separated from the α particles. BaF_2, however, due to its very good timing resolution, is best suited for time of flight applications, giving good mass resolution. The resolution in the phoswich is comparable to the CsI, however, the particles have to punch through the thin fast plastic to permit good identification.

In conclusion, CsI seems to work best if one wants identification down to low energies, followed by the phoswich. BaF_2 excels if timing is important.

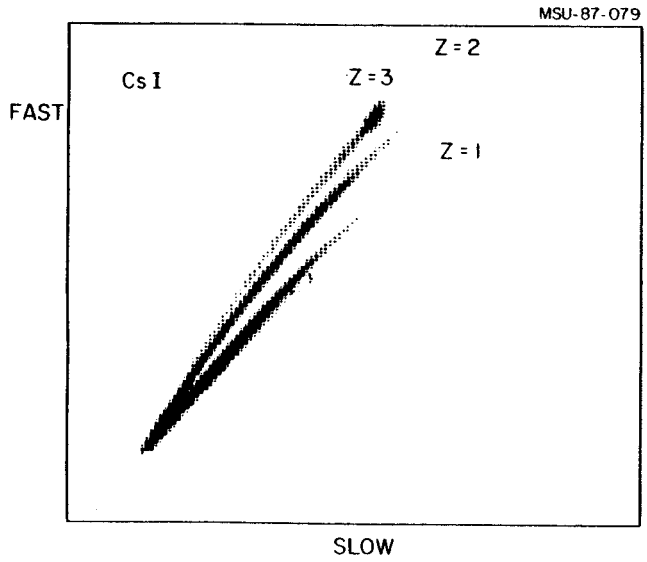

Fig. 2. Example of a particle identification plot using pulse shape discrimination for CsI. Resolution is achieved down to ~4 MeV.

We plan to investigate the relative merits of the "two QDC method" and the classic "zero cross method" as a means to do pulse shape discrimination. The latter method could be applied to a CsI photodiode combination.

References

1. G.D. Westfall, et al NIM A238 (1985) 347.

GAS CHROMATOGRAPHY AS A TECHNIQUE FOR DETECTING TRACES OF H_2 IN CRYOGENIC He

J.C. Batchelder and Wm.C. McHarris

In liquid-He cryogenic systems any impurity can cause problems by solidifying and stopping up the lines. Most substances can be removed through the use of cold traps and micro-porous filters. However, H_2 and He make their way through these and present a lingering problem. Gas chromatography has proven to be a straightforward, effective means for identifying minute quantities of H_2 in He, and here we report our experimental findings during the past year.

Gas chromatography works by taking advantage of the different rates of adsorption by various chemical species.[1] A gas chromatograph consists of an injection port, a long column packed with a suitable adsorbent substrate, and a detector at the end of the column. For H_2 in the presence of other weakly adsorbed gases, a good substrate is the zeolite carrying the trade name, "molecular sieve."[2] The sample(s) to be adsorbed and separated are transported along the long column (necessarily long because of the low adsorptiveness of H_2) by appropriate inert carrier gases.

We used a modified Varian Aerograph Model 90P-3 gas chromatograph.[3] It contained a 16-ft long stainless steel column packed with 60-80 mesh #5A molecular sieve ($2Ca \cdot Al_2O_3 \cdot SiO_2$), having an effective pore diameter of 5 A.

The detector for this gas chromatograph consisted of a wire serving as one arm of a Wheatstone bridge. It was calibrated for the carrier gas, and the changes in resistance of the wire as the sample gases flowed over it were recorded. He is commonly used as the carrier gas for such experiments, but we had to find a different carrier gas. We found Ar to be an optimal carrier because of its relative inertness, yet very different thermal conductivity from H_2 and He. (See Table 1.)

Table 1

Gas	Density	Thermal Conductivity
Ar	1.784 g/l	45.5
He	0.178 g/l	376.1
H_2	0.0899 g/l	471.1

We injected samples into the chromatograph at room temperature, using a gas syringe. Our samples were prepared by successive dilution with He. We discovered, as anticipated, that the best separations were attained with a slow flow rate (≈12-15 ml/min) and with successively lower temperatures. We were able to detect 100 ppm H_2 in He quite readily at -68°C, which is easily reached by immersing the column in a dry ice-isopropanol bath. Spectra produced under these conditions are shown in Fig. 1. At lower temperatures and possibly with longer columns, the detection sensitivity could be lowered considerably. By using tritium dilution techniques, we should be able to detect 1 ppm H_2 or less.

References

1. P.G. Jeffrey and P.J. Kipping, Gas Analysis by Gas Chromatography, Pergamon Press, Oxford, 1972, Chap. 7.
2. C.J. Cowper and A.J. DeRose, The Analysis of Gases by Chromatography, Pergamon Press, Oxford, 1983, Chap. 4.
3. We thank the MSU Chemistry Chemistry for giving us this gas chromatograph and for keeping it in good repair.

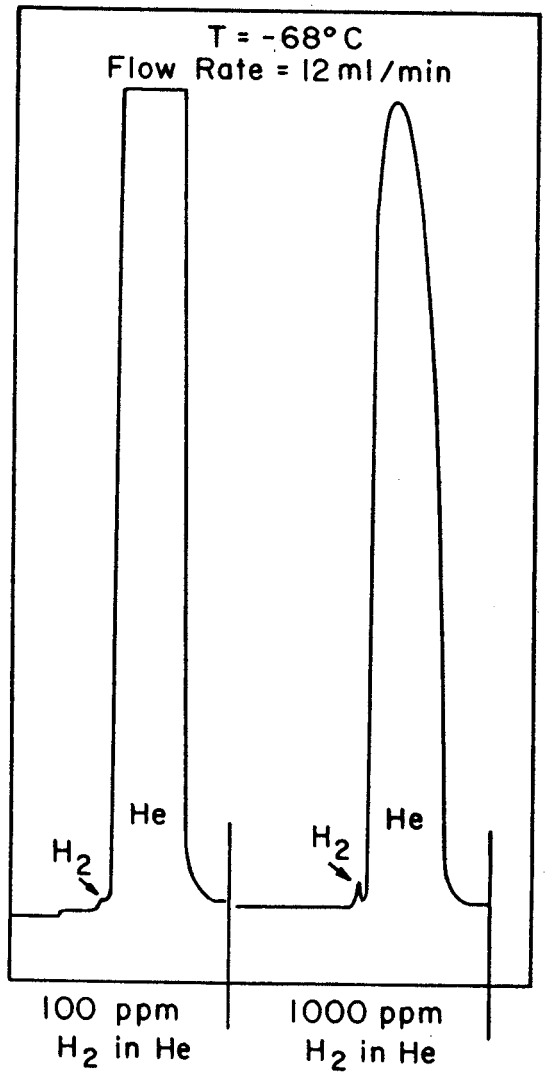

Fig. 1. H_2-He gas-chromatographic separation, using a 16-ft column packed with 60-80 mesh #5A molecular sieve.

ACTIVATION OF ^{Nat}Cu BY 480 MeV ^{12}C

R.M. Ronningen

The K500 cyclotron and ECR source have opened up new regimes of projectile mass, energy and intensity. New radiation hazards are anticipated.

Radioactive beams are now being produced by the K500 cyclotron. The process for making them involves stripping an intense primary beam to a higher charge state. The stripped beam is lost in the accelerator and is assumed to irradiate the copper dees.

The question of activating the cyclotron interior beyond safe levels for maintenance has resulted in an activation study of copper foils. A stack of six copper foils, each 10 mils thick, were irradiated by a 480 MeV $^{12}C^{5+}$ beam. The collected charge was 253 microcoulombs. Dose rates and activities were studied for each foil and the foil stack using an ion chamber (with and without its beta shield) and a Geiger-Mueller counter (with and without a beta filter). Figure 1 shows the radiation decay curve measured by the ion chamber located about 15 cm above the foils.

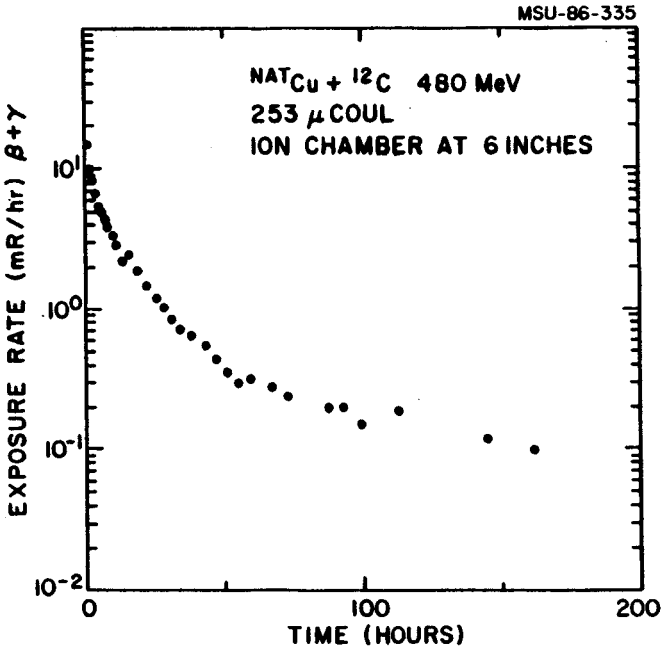

Fig. 1. The decay curve for the irradiation of a copper foil with a 480 MeV ^{12}C beam and a total collected charge of 253 microcoulomb.

The production of radiation was peaked for the foils located between 120 and 240 MeV effective bombarding energy. The foil stack is self-shielding to a significant extent and the radioactivity yields mainly betas. These data were used to estimate personnel exposure for planned maintenance after a radioactive beams experiment.

Gamma rays from the foils were identified at Purdue University[1] to obtain information on long lived activities. Those with significant production cross sections (> 10 mb) were: $^{46}Sc(84d)$, $^{48}V(16d)$, $^{51}Cr(28d)$, $^{52,54}Mn(6d,313d)$, $^{56,57,58,60}Co(79d,272d,71d,5.3y)$, and $^{65}Zn(244d)$.

Future studies will include higher energy beams on copper, and on aluminum. These will help us plan for K800 maintenance.

References

1. S.Y. Cho, private communication.